Swirl stabilized premixed flame analysis using of LES and POD

Iudiciani, Piero

2012

Swirl stabilized premixed flame analysis using LES and POD

LUND
UNIVERSITY

Piero Iudiciani

Department of Energy Science
Division of Fluid Mechanics
Faculty of Engineering, LTH
Lund University, Lund, Sweden

Akademisk avhandling som för avläggande av teknologie doktorsexamen vid tekniska fakulteten vid Lunds Universitet kommer att offentligen försvaras onsdagen den 25 april 2012, kl. 10.15 i hörsal M:B, på M-huset, Ole Römers väg 1, Lund.
Fakultetsopponent: Dr. Sébastien Ducruix, (École Centrale Paris / CNRS, Frankrike)

Academic thesis which, by due permission of the Faculty of Engineering at Lund University, will be publicly defended on Wednesday 25 April, 2012, at 10.15 a.m. in lecture hall M:B, in the M-bulding, Ole Römers väg 1, Lund, for the degree of Doctor of Philosophy in Engineering.
Faculty opponent: Dr. Sébastien Ducruix, (École Centrale Paris / CNRS, France)

Thesis for the degree of Doctor of Philosophy in Engineering.
ISBN 978-91-7473-281-8
ISSN 0282-1990
ISRN LUTMDN/TMHP-12/1086-SE

Department of Energy Sciences, Division of Fluid Mechanics
Lund Institute of Technology
Box 118, 22100 Lund, Sweden

Typeset in LaTeX
Printed by E-husets Tryckeri, Lund, March 2012

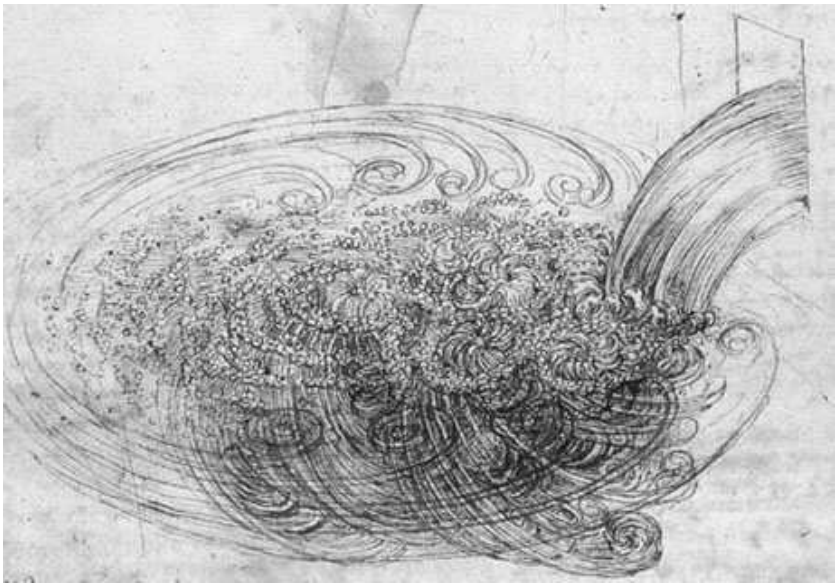

Observe the motion of the surface of the water, which resembles that of hair, which has two motions, of which one is caused by the weight of the hair, the other by the direction of the curls; thus the water has eddying motions, one part of which is due to the principal current, the other to the random and reverse motion.

Leonardo da Vinci (April 15, 1452 – May 2, 1519)

Abstract

For environmental and human health reasons, the regulations on the emissions from combustion devices are getting more and more strict. In particular, it is important to abate the emission of pollutants deriving from combustion in gas turbines. A solution is the use of swirl stabilized, lean premixed combustion. Besides the beneficial effects, there are still some issues related to instabilities and a full, clear understanding of the dynamics of swirling flows and flames has not been reached yet. This is where the contribution of this thesis lie. In this work, advanced techniques, namely Large Eddy Simulation (LES), Proper Orthogonal Decomposition (POD), and optical diagnostics, have been applied to analyze swirl stabilized flames, relevant to gas turbine applications.

A simple geometry combustor, the "Lisbon"burner, useful for fundamental studies, was simulated by LES. The dynamics of a forced swirling flame are successfully captured, allowing to characterize the influence of the Precessing Vortex Core on the flame stabilization and its interactions with axial fluctuations.

However, real applications are typically characterized by more complex geometry. Special attention was then paid to the study of a realistic burner, the "Triple Annular Research Swirler (TARS)". Detailed LES of this aeroengine-like fuel-injector, including the upstream portion of it, shed some light on the experimentally observed asymmetry of the flow. The flow through the fuel-injector, unaccessible to experiments, was clarified and detailed. Differences and similarities with academic simple geometry swirl burners were also highlighted. For reacting conditions, the LES formulation was able to explain the peculiar stabilization mechanism in a case where the CRZ was destroyed by thermal expansion, to capture dual behavior/hysteresis phenomena, to describe the dynamics of a lean flame and its interaction with the PVC.

Throughout the thesis, POD analysis highlighted large scale structures and flame fluctuations of several combustors contributing to the understanding of the dynamics of swirl stabilized flames.

It was shown how POD can relate to conditional averaging and in particular to phase averaging. A POD based phase averaging procedure was used to study thermo-acoustic oscillations. Applied to experimental data obtained with a simple and relatively cheap set-up, but complex geometry and flow, it opens possibilities for application on industrial rigs, enabling phase averaging with a priori unknown period.

The concept of Extended POD was expanded to combustion applications highlighting the correlations between flow and flame dynamics. For both numerical and experimental data, it gave new insights into flames and their correlation with the flow field.

Contents

Chapter 1

Introduction

1.1 Energy situation

In order to sustain the current living standards of modern society, the world's energy demand is constantly increasing. Although, in the future, a larger contribution from renewable and sustainable sources is expected, it is foreseen that a great part of energy will still be produced by means of combustion, as sketched in Fig. 1.1 [1]. Moreover, the recent progresses in green-technologies enable today to partly replace fossil fuels with synthetic renewable hydrocarbons [2]. Therefore combustion is still, and so it will be in years to come, a vital technology for our modern society to convert these fuels into work or electricity. One of the main problems related to combustion are pollutants, harmful for the environment and for the human health, and green-house gases, contributing to global warming. Among all the various combustion applications, the gas turbine is often described as the prime mover of our time [3]. It finds an increasingly wide variety of applications, the main ones being electrical power generation or mechanical drive for land stationary gas turbines, propulsion in the case of aeronautical engines. Further research is needed in order to reduce the undesired emissions of combustion devices: carbon monoxide (CO), unburned hydrocarbons (UHC), soot and especially nytrogen oxides (NO_X) [4]. In particular for stationary gas turbines, ultralow NO_X operation has even become a major marketing issue [3].

1.2 Gas turbines

A typical sketch of a gas turbine is reported in Fig. 1.2. In the schematics of Fig. 1.2, the flow goes from left to the right. It is composed by three main components, a compressor, a combustor and a turbine. The pressure of the incoming flow is first increased through the compressor. The air is then conveyed into the combustion chamber, where fuel is added and burnt. The chemical energy of the fuel is converted into heat, increasing the energy (temperature) of the gas. These burnt gases at high temperature then expand through the turbine. Part of the energy is used to drive the compressor, and the remaining part is the useful energy. In stationary gas turbines it is used to drive a mechanical load or an electricity generator, while in aero-engines the flow further expands for giving propulsion.
This thesis aims at contributing to the part of the process in which the air and fuel are mixed and burnt in the combustion chamber. As it will be clarified in Section 2.3.1.1, there are two main modes of combustion: premixed, in which air

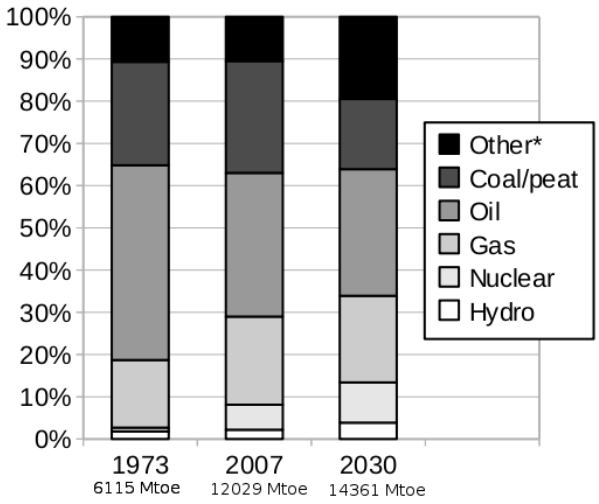

Figure 1.1: World's fuel shares of total primary energy supply (TPES). *Other** includes combustible renewables & waste, geothermal, solar, wind, tide, etc. Data from [1].

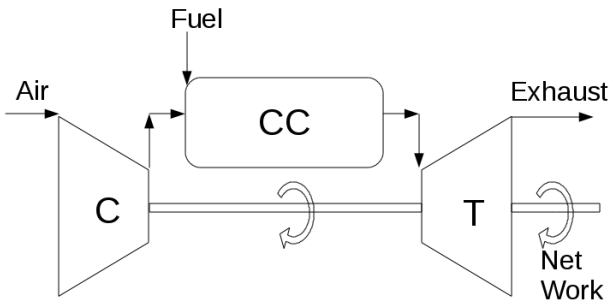

Figure 1.2: Gas turbine schematics. C: compressor; CC: combustion chamber; T: turbine.

and fuel are blended together before the combustion takes place, and non-premixed (diffusion type) in which the fuel and air are injected separately and mix directly into the combustion chamber. To reduce the level of the emissions, it is important to reduce the temperature of the flame, as it will be explained later in Section 2.2.2. Premixed flames are thus desirable, because they allow a better control of the flame temperature, and consequently of emissions. At the present time lean premixed (LP) combustion appears to be the only technology available for achieving ultralow NOx emissions from practical combustors [3,5]. When dealing with liquid fuels, one should rather talk about lean premixed prevaporized (LPP) [6] combustion.

1.3 Swirling flows in gas turbines

In the design of modern lean premixed combustors, swirling flows play an important role. Vortex breakdown [7] is nowadays the preferred flame holding mechanism. Swirl stabilized flames are rather compact and allow the design of smaller and lighter combustion chambers. Moreover there is the advantage that no flame holders are needed in the hot regions of the flame (and therefore no need to cool them). The incoming fresh mixture is given a swirling motion which induces a recirculating bubble in the center of the jet. This Central Recirculation Zone (CRZ), recirculating hot burnt gases, provides the heat necessary to preheat and ignite the incoming air-fuel mixture. Moreover, swirling flows enhance mixing of the fuel with the air flow, both for gaseous and liquid fuels. In particular liquid fuels need to be atomized, vaporized and mixed. Complex swirling flows with azimuthal shear layers and vortex breakdown allow rapid mixing over a short length. Therefore, fuel-injectors with multiple swirlers are typically used when atomization utilizes airblast atomizers [5] (Fuel is atomized by shear with the incoming high speed flow, another possibility is to inject fuel at high-pressure, so called pressure atomizers [5]).

1.4 Problems and challenges

LP combustion allows to reduce the peak temperature, avoiding the formation of pollutants, but stability issues arise. Typical problems are flashback [8, 9], blow-off [8, 10], thermo-acoustic oscillations [11–16], combustion noise [17, 18]. When operating at very lean conditions, the peak temperature in the combustor becomes lower, whereby lowering the NOx emissions levels. On the other hand, providing less heat to the fresh gases, lean flames are susceptible to quenching or flame blow-out. Typical dynamics related to vortex breakdown [19], such as helical structures [20], Precessing Vortex Core (PVC) [21–25], can be a source of unsteady flow and heat release which may trigger instabilities such as thermo-acoustic oscillations (coupling between pressure and heat release fluctuations). Although they have been used and studied for several decades, swirling flows are still an open field of research. To address the stability issues mentioned above, understanding the dynamics of vortex breakdown and swirl-stabilized flames is crucial.

1.5 Strategy and solutions

In recent years, strong efforts have been made both experimentally and numerically to improve the knowledge of the related phenomena and to explore ideas for circumventing flame stability issues in LPP combustors. For example, the dynamic response to axial oscillations of both non-reacting [22, 26–31] and reacting [32–39] swirling flows has been analyzed. The work presented in this thesis has the main goal to contribute to the better understanding of swirling flows and flames. This has been done by using advanced numerical and experimental techniques. Special emphasis has been put on numerical computations by means of Large Eddy Simulation (LES) [40]. LES allows to resolve the major fraction of the turbulent kinetic energy and to capture the unsteady motion of large scale structures. Thereby, it is believed to be indispensable if one wants to address the stability and the dynamics of flow/flames. Large scale coherent structures have been found to have an important role in raising flame instabilities because interacting with the flame they can drive heat release fluctuations [32, 41, 42]. LES provides a rather large amount of data which has to be processed. Normally, one uses statistical tools to characterize the random turbulent fluctuations. The most energetic fraction of the fluctuations can be identified using *Proper Orthogonal Decomposition* (POD) [43]. POD is a well established technique for the analysis and control of cold turbulent flows [44–47], but recently has also gained interest for its application to reacting flows [18, 24, 39, 48–55]. This thesis also aims at encouraging the use of POD as a tool to analize reacting flows and in particular to improve the understanding of flame dynamics. This modal decomposition can be applied to either numerical or experimental data, to extract the fluctuations of the different variables of interest (velocity field, OH-signal, OH-chemiluminesce, etc.) as a set of "modes". Highlighting relevant flow and flame dynamics, it is a powerful tool to investigate the flame stability. Recent POD-derived techniques, such as POD based a-posteriori phase averaging [56, 57], and *Extended POD* (EPOD) [58, 59] (see Section 3.3) may then open new possibilities. The application of EPOD to reacting flows is particularly interesting: correlating variables representing the reaction zone (progress variable, species, temperature, etc.) with the velocity field, the interactions between flow and flame dynamics can be highlighted.

Usually, to investigate fundamental phenomena, one tries to reduce the problem to the study of simple geometry, downscaled laboratory apparatus, an idealized reproduction of reality. We cite here a few examples [22, 26, 60]. Such an approach is indeed very instructive to gain general knowledge, isolate the phenomena, or to validate models. We followed this "modus operandi" in the case of Paper I [61], in which the interaction of PVC and longitudinal oscillations is studied in a simple geometry swirler, the "Lisbon" burner [23, 60], and in Paper II [62], where a simple laminar Bunsen flame interacting with acoustics is used to exemplify the use of EPOD in combustion applications. However, since the reality is much more complicated, it is not guaranteed that the results obtained in such idealized situations can be extrapolated to actual industrial applications. Many factors neglected or removed in a

laboratory can play an important role. For example, more complex geometries are typically used. For this reason, the thesis also studies flows and flames generated through a complex device, the Triple Annular Research Swirler, TARS [63], a model gas turbine fuel-injector, mimicking the ones used in propulsion applications. The investigations of this burner are given in Papers III-VI. Paper III [64] clarifies the complex flow inside and outside the TARS; Paper IV [65] proposes a method for the analysis of thermo-acoustic instabilities in industrial rigs, Paper V [66] explains the stabilization mechanism for a case without central recirculation zone and Paper VI [67] focuses on the dynamics of a very lean flame.

1.6 Thesis contribution

The main achievements accomplished with the work of this thesis are listed below:

- The dynamics of a forced swirling flame are successfully captured by means of LES, allowing to characterize the influence of the PVC motion on the flame stabilization and its interactions with axial fluctuations.
- Proper Orthogonal Decomposition highlighted large scale structures and flame fluctuations of several combustors contributing to the understanding of the dynamics of swirling flames.
- POD based a-posteriori phase averaging was used to study thermo-acoustic oscillations. Applied to experimental data obtained with a simple and relatively cheap (for example compared to laser diagnostics) set-up, but complex geometry and flow, it opens possibilities for application on industrial rigs, enabling phase averaging with a priori unknown period.
- The concept of Extended POD was expanded to combustion applications highlighting the correlations between flow and flame dynamics. For both numerical and experimental data, it gave new insights into flames and their correlation with the flow field.
- More detailed LES of the TARS burner including the upstream portion of it, shed some light on the experimentally observed asymmetry of the flow.

1.7 Thesis outline

This thesis is organized as a collection of the papers which have been produced during this project. The articles are preceded by an introductory overview of the topics which are not treated in details in the papers. In Chapter 2 the theoretical background about turbulence, combustion, turbulent combustion and flame stabilization is briefly treated. In Chapter 3 the methods used to collect and process the information (LES, experimental diagnostics, POD-EPOD) are described. Chapter 4 contains a description of the test cases studied in this work, i.e. the *Lisbon* and

the *TARS* burners. A summary of the main results is reported in Chapter 5. The detailed results are found in the papers appended at the end of the book. Chapter 6 summarizes the content of each paper together with the contribution of the candidate to the paper itself. In Chapter 7 the main conclusions of this work are resumed, together with proposals for future investigations.

Chapter 2

Turbulent reacting flows

2.1 Phenomenological description of turbulence

2.1.1 Laminar and turbulent flows

Most of the flows in industrial applications are turbulent. A turbulent flow is characterized by the fact of being irregular, random and chaotic. A classic way to characterize turbulence is the well known Reynolds experiment. He analyzed the motion of water in a straight pipe visualizing streaks of dye (Fig. 2.1). He showed that the flow depends on a dimensionless parameter; namely, the Reynolds number:

$$Re = \frac{\rho U L}{\mu} \tag{2.1}$$

where ρ and μ are the density and the viscosity of the fluid, U and L are characteristic velocity and length scales for the flow, respectively. When Re is below a critical value the flow is *laminar*: the streak keeps flowing straight and without any perturbation. Above the critical Re, the flow character changes and with increasing Re it becomes *turbulent*: the flow is irregular and random. A sketch of the flow visualizations for different Re, as observed by Reynolds, is depicted in Fig. 2.1.

In a turbulent field, the velocity in a point x as a function of time t is a random vector field u(x,t) [69]. Therefore one tries to characterize turbulence by means of statistical quantities and the velocity field is usually expressed in terms of a mean $\overline{u(x,t)}$ and a fluctuating field $u'(x,t)$ so that $u'(x,t) = \overline{u(x,t)} - u(x,t)$. The random field is *statistically stationary* if all the statistics are invariant under a shift in time, it is *statistically homogeneous* if all the statistics are invariant under a shift in space [69]. If it is the fluctuating velocity field to be statistically homogeneous,

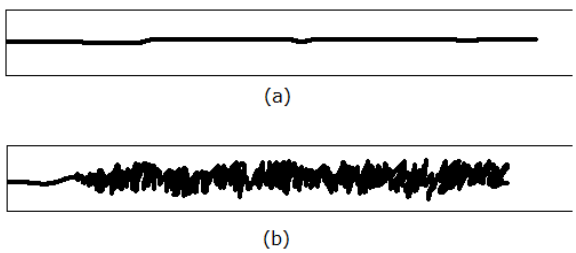

Figure 2.1: Visualization of the Reynolds experiment: laminar (a) and turbulent (b) flow. Sketched after [68].

one talks about *homogenous turbulence*: turbulence is statistically the same in all the points. If the statistics of the fluctuating field are invariant under rotations or reflections of the coordinate system, one talks about *isotropic turbulence* [69] (i.e. directionally independent).

2.1.2 Turbulent scales and energy cascade

A central concept in the turbulence theory is the *energy cascade*. The main idea is that the kinetic energy of turbulent fluctuations, in average is transferred from larger eddies to smaller ones. The length scale of the largest eddies is expressed by the *integral scale*, denoted with l_0. The turbulence kinetic energy is produced mainly at these scales. The large scales are referred to as the *energy containing* range. Eddies break up into smaller eddies by an inviscid process, if the Reynolds number is high. The range of scales at which the inviscid process is dominant is referred to as the *inertial range*. These smaller eddies undergo further break up into even smaller eddies. The process continues until the energy is dissipated into heat by a viscous process (*viscous range*). The small scales at which dissipation dominates are characterized by the *Kolmogorov* length and time scale, denoted with η and τ_η, respectively. This theory is based on Kolmogorov's hypotheses [69]:

> **Kolmogorov's first similarity hypothesis**. At sufficiently high Re the statistics of the smallest scale motions are uniquely determined by the viscosity ν and the dissipation rate of turbulent kinetic energy, ε.

This hypothesis defines a range of scales usually referred to as the *universal equilibrium range*. The universal equilibrium range contains the *inertial subrange* and the *viscous subrange* discussed above. The turbulent eddies in the inertial and the viscous subranges are of universal character and therefore are independent of the particular turbulent flow case. The inertial subrange is defined by:

> **Kolmogorov's second similarity hypothesis**. At sufficiently high Re there is a range of scales such as $\eta \ll l \ll l_0$ where the statistics of the motion are uniquely determined by the dissipation rate of turbulent kinetic energy ε, independently of the viscosity ν.

In this range of scales the viscous effects are negligible and the motions are dominated by inertial effects. Of course, the theory is not universal close to the boundaries of the domain (and in particular solid walls). The range of validity of the theory may be even more restricted when the flow is statistically unsteady, or highly non-isotropic. It is useful to give some definitions of time and length scales for the various ranges:

- **Integral length scale**
  The integral scale can be defined through the autocorrelation function:

$$f(r) = \frac{\overline{u'(x)u'(x+r)}}{\overline{u'(x)u'(x)}} \tag{2.2}$$

where $u'(x)$ is the velocity fluctuation in a point and r is the distance from the point x, the overbar indicates time average. The integral length scale is then defined as the integral of the autocorrelation function:

$$l_0 = \int_0^\infty f(r)\, dr \tag{2.3}$$

and it represents the mean distance at which the fluctuations are correlated, a *memory effect* in space.

- **Taylor scale**
  The Taylor scale can be defined from the second derivative of the autocorrelation function at r=0, as follows:

$$\lambda_f^2 = -\frac{2}{\frac{d^2 f}{dr^2}|_{r=0}} \tag{2.4}$$

  Taylor thought that this length scale could roughly describe the diameter of the smallest eddies responsible for dissipation. However, this happens at the Kolmogorov scales. The Taylor length scale has no clear physical interpretation [69], but it is useful in practical applications since it typically falls in the inertial subrange. Thus, this scale can be used to estimate the required spatial resolution for LES.

- **Kolmogorov scale**
  The Kolmogorov scales are the smallest turbulent scales. The length, time and velocity scales, are denoted with η, τ_η and u_η respectively. These are expressed by:

$$\eta = \left(\frac{\nu^3}{\varepsilon}\right)^{\frac{1}{4}}, \qquad \tau_\eta = \left(\frac{\nu}{\varepsilon}\right)^{\frac{1}{2}}, \qquad u_\eta = (\varepsilon\nu)^{\frac{1}{4}} \tag{2.5}$$

  Using these scales the turbulent Reynolds number $Re_\eta = \frac{u_\eta \eta}{\nu} = 1$, consistently with the fact that the behavior is universal.

Assuming equilibrium between production of turbulent kinetic energy and dissipation, it is possible to derive relations between the integral and Kolmogorov scales [69]:

$$\frac{\eta}{l_0} \sim Re^{-\frac{3}{4}}, \qquad \frac{\tau_\eta}{\tau_0} \sim Re^{-\frac{1}{2}} \tag{2.6}$$

where Re is the turbulent Reynolds number (based on velocity and length scales of the eddies). Therefore the Kolmogorov length scale decreases with increasing Re. For a typical gas turbine, assuming $Re \simeq 10^6$ and $l_0 \simeq 0.1m$, it is of the order of microns: $\eta \simeq 3\mu m$. Fig. 2.2 shows a typical energy spectrum for a homogeneous turbulent flow field. It represents the contribution to the turbulent kinetic energy of the various scales. In the graph the length scales λ are expressed in terms of their wavenumbers $k = 2\pi/\lambda$. It can be shown by dimensional arguments that for homogeneous turbulence the following relation holds in the inertial subrange [69]:

$$E(k) \sim \varepsilon^{\frac{2}{3}} k^{-\frac{5}{3}} \tag{2.7}$$

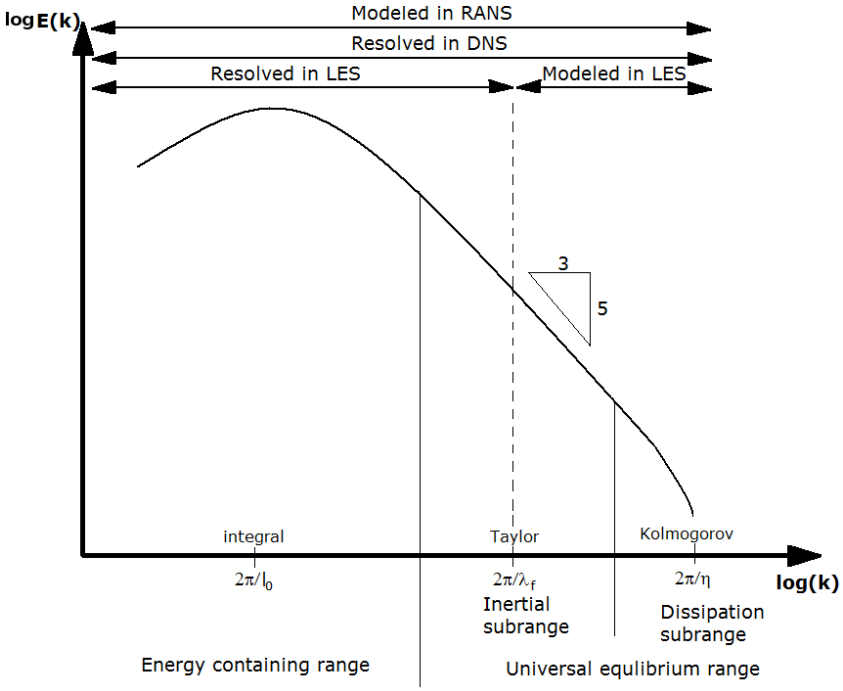

Figure 2.2: Energy spectrum as a function of wave number. Sketched after [70].

2.2 Combustion

2.2.1 Chemical oxidation reactions

Combustion is a chemical process which involves chemical oxidation reactions in gas phase. A generic chemical reaction can be described as follows:

$$\sum_{i=1}^{N_S} \nu_i' Y_i \longleftrightarrow \sum_{i=1}^{N_S} \nu_i'' Y_i \tag{2.8}$$

where Y_i represents the generic chemical species and ν_i', ν_i'' are respectively the stoichiometric coefficients of the reactants and the products. The rate at which the reaction occurs is often given by the Arrhenius law:

$$K = AT^b e^{-\frac{E_a}{\Re T}} \tag{2.9}$$

where A and b are experimental parameters, E_a is the *energy of activation*, $\Re$ is the universal gas constant and T is the temperature. During combustion the *fuel* reacts with the *oxidizer* (in general air or pure oxygen) to form *products*, and a certain amount of heat is released (exotermic reaction). Typical fuels in industrial applications are hydrocarbons burning in air or oxygen. The combustion process is commonly described with one or a very few *global reactions*. An example of one-step global reaction in the case of methane-air combustion is:

$$CH_4 + 2O_2 = CO_2 + 2H_2O \tag{2.10}$$

In reality a larger number of reactions are involved, with formation of intermediate species and radicals. A system of reactions is called a *reaction mechanism*. A *detailed* mechanism may contain thousands of reactions and hundreds of species. If one wants to fully compute a reacting flow, a transport equation for each of the species should be solved, see Section 2.4. This is, however, not feasible for computational reasons due the very high stiffness of the system as well as memory and CPU requirements. For the same reason, one may also introduce simplifications whereby many fast reactions can be eliminated by assuming equilibrium or steady-state. By reducing the chemical system only the most important reactions are kept (*reduced* or *skeletal* mechanisms). Usually skeletal mechanisms contain about 10-20 species which is still computationally rather expensive. As an example the detailed mechanism of air-methane combustion GRI mech 3.0 [71] contains 53 species and 325 reactions. Here only a few reactions are given in Table 2.1. It should be remarked that for heavier and more complex fuels, for example n-heptane or diesel, the number of species and reactions involved dramatically increases.

$CH_4 + M$	$\rightarrow$	$CH_3 + H + M$
$O_2 + H$	$\rightarrow$	$OH + O$
$CH_4 + H$	$\rightarrow$	$CH_3 + H_2$
$CH_4 + O$	$\rightarrow$	$CH_3 + OH$
$CH_4 + OH$	$\rightarrow$	$CH_3 + H_2O$
$CH_3 + OH$	$\rightarrow$	$CH_2 + H_2O$
$CH_3 + O$	$\rightarrow$	$CH_2O + H$
$CH_2 + O$	$\rightarrow$	$CHO + H$
$CH_2 + OH$	$\rightarrow$	$CH + H_2O$
$CHO + H$	$\rightarrow$	$CO + H_2$
$CHO + OH$	$\rightarrow$	$CO + H_2O$
$CO + OH$	$\rightarrow$	$CO_2 + H$

Table 2.1: A few reactions from the GRI mech 3.0 [71] mechanism for air-methane combustion.

2.2.2 Pollutant formation

2.2.2.1 Carbon monoxide

Carbon monoxide is toxic for the human body. It interferes with blood oxygen absorbtion and can lead to death by asphyxiation [3]. CO is formed when the combustion is not complete. The oxidation of CH_4 into CO, through the intermediate reactions listed in Table 2.1, is fast, while the formation of CO_2, through the last reaction in Table 2.1, is slow and requires high temperature. At very high temperatures, the backward reaction rate (dissociation of CO_2 into CO) might become significant, in particular for rich mixtures. CO formation is influenced by several factors. It decreases by increasing air inlet temperature and pressure, and it has a minimum for an optimal equivalence ratio at about $\phi \sim 0.8$. A typical trend of the

CO formation with the flame temperature is reported in Fig. 2.3 [3].

2.2.2.2 Nitrogen oxide

Nitrogen oxides are among the most undesired pollutants in gas turbines. They contribute to photochemical smog and acid rains. NOx can lead to the formation of ozone in the troposphere (related to health problems such as allergies, respiratory illnesses, headaches) and ozone depletion in the stratosphere (which protects the Earth from UV radiations) [3]. In this Section the main routes of formation of NO known in the literature are described.

Zel'dovich mechanism

The Zel'dovich mechanism is also known as *thermal* because of its dependence on the temperature. The following reactions are involved:

$O + N_2$	$\leftrightarrow$	$NO + N$
$N + O_2$	$\leftrightarrow$	$NO + O$
$N + OH$	$\leftrightarrow$	$NO + H$

Table 2.2: Zel'dovich mechanism.

This mechanism is not dominant below 1800-1850 K, explaining why one wants to keep the temperature low in lean premixed flames. It is mainly active in the postflame zone, since it is rather slow as compared to the fuel oxidation. It is therefore important to keep the residence time as short as possible.

Fenimore or prompt mechanism

This mechanism can be active in the reaction zone, where the short-life CH radical is formed. The NO is formed through intermediate amines and cyano compounds and it is particularly important in rich flames [72].

$CH + N_2$	$\leftrightarrow$	$HCN + N$
$C + N_2$	$\leftrightarrow$	$CN + N$
$HCN + O$	$\leftrightarrow$	$NCO + H$
$NCO + H$	$\leftrightarrow$	$NH + CO$
$NH + H$	$\leftrightarrow$	$N + H_2$
$N + OH$	$\leftrightarrow$	$NO + H$

Table 2.3: Fenimore mechanism.

N_2O intermediate mechanism

Another route of NOx formation is through nitrogen oxide N_2O:

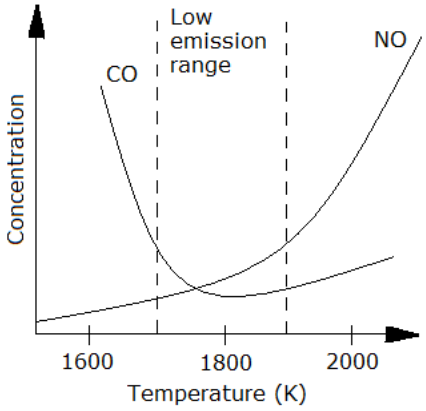

Figure 2.3: Trends of CO and NO emissions as a function of temperature in a gas turbine combustor. After [73].

$O + N_2 + M$	$\leftrightarrow$	$N_2O + M$
$H + N_2O$	$\leftrightarrow$	$NO + NH$
$O + N_2O$	$\leftrightarrow$	$NO + NO$

Table 2.4: N_2O intermediate mechanism.

This mechanism is particularly important at low temperature, i.e. lean flames [72].

Fuel nitrogen mechanism

NOx can be produced when nitrogen in form of amino groups is found in the fuel, for example in the case of coal or biofuels. The nitrogen bound in the fuel can be rapidly converted into HCN or ammonia NH_3. Then the prompt mechanism described above can be activated.

The trends of NO and CO emissions as a function of the temperature are sketched in Fig. 2.3 [73]. One may note that the optimal operating temperature for a gas turbine is in a very narrow range, around 1750-1800 K, where emissions of both CO and NO are small.

2.2.2.3 Unburned hydrocarbons (UHC)

Unburned hydrocarbons (UHC) are toxic and contribute to urban smog [3]. They are typically emitted when the combustion is not complete and especially related to poor atomization and evaporation of liquid fuels, inadequate burning rates. Generally UHC emission is influenced by the same factors leading to CO emissions [3].

2.3 Turbulent combustion

2.3.1 Phenomenological description of flames

A flame is a mode of combustion [72]. One talks about a *flame* when combustion occurs in a thin reaction layer propagating into a flow. A flame is also characterized by light emission. However, combustion may occur without light radiation: distributed in a volume (*flameless* or *mild* combustion [74–76]), or on a surface (*catalytic* combustion).

2.3.1.1 Premixed and diffusion flames

Flames can be distinguished according to the way fuel and oxidizer are mixed together. When fuel and oxidizer are mixed before entering the combustion chamber one talks about *premixed* flames. In *Non-premixed* or *diffusion* flames instead, fuel and oxidizer enter the combustion chamber separately and mix together in the reaction zone. The way fuel and oxidizer are mixed affects the flame structure. Premixed flames are desirable because they allow better temperature control, and therefore enabling low NOx emissions. Diffusion flames always have regions in which fuel and oxidizer are in stoichiometric proportion. They are therefore characterized by higher temperatures, which is bad both in terms of emissions and soot formation.

2.3.1.2 Laminar and turbulent flames

Flames can be also characterized by the Reynolds number. Depending on the nature of the flow, one distinguishes between *laminar* and *turbulent* flames. Laminar flames are interesting from an academic point of view to understand elementary combustion phenomena. The main impact of turbulence is on the burning rate: turbulent flames ensure faster burning and are therefore popular in industrial applications and in particular in gas turbines. This thesis focuses mainly on premixed turbulent flames.

2.3.1.3 Laminar premixed flames

An important parameter to characterize premixed flames is the *equivalence ratio* Φ of the fresh mixture. It is defined as:

$$\Phi = \frac{(Y_F/Y_O)}{(Y_F/Y_O)_{st}} \tag{2.11}$$

where Y_F and Y_O are respectively the fuel and oxidizer mass fractions. The subscript st indicates stoichiometric conditions (fuel and oxidizer in exact amount so that the combustion is complete). The equivalence ratio tells how much fuel and oxidizer are mixed with respect to theoretical stoichoimetric conditions. $\Phi < 1$, $\Phi = 1$ and $\Phi > 1$ correspond to *lean*, *stoichiometric* and *rich* mixtures, respectively. For example $\Phi < 1$ indicates that the oxydant is in excess. In Fig. 2.4 the typical structure of a lean laminar flame is reported. It can be imagined as a flame front (thin reacting

layer) propagating towards the fresh mixture in a tube (a propagating flame front is also referred to as *deflagraton wave*). In a reference frame which moves with the flame front, typical curves of species composition and temperature are given in Fig. 2.4. Combustion occurs in a thin zone called reaction zone which is formed by

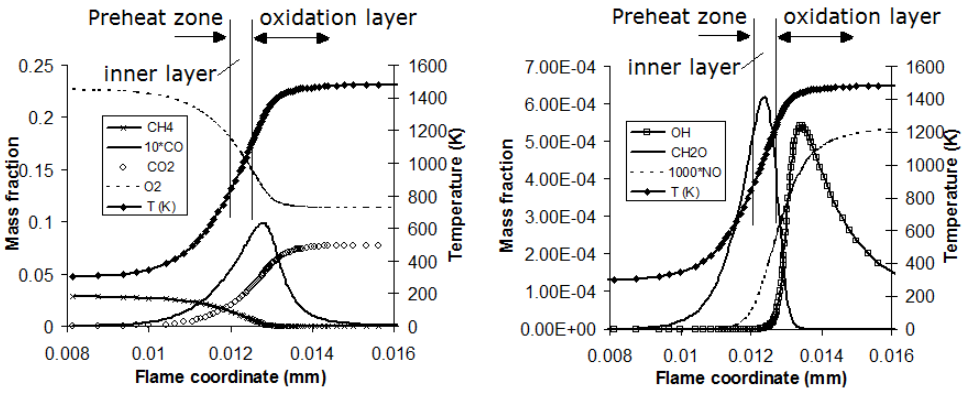

(a) (b)

Figure 2.4: Structure of a lean premixed laminar flame. Methane/air flame, $\phi = 0.5$ and $T_u = 300K$. Computed with GRI 3.0 mechanism [71].

the *inner layer* and the *oxidation layer*. On the fresh mixture side fuel (methane in this case) and oxidizer (oxygen) compositions are constant, the temperature is low. In the *preheat* zone the composition of reactants start to decrease while the temperature increases. In the preheat zones no reactions are occurring and the changes in composition and temperature are only due to molecular and thermal diffusion from the reaction zone. If the mixture is lean, across the reaction zone all the fuel is consumed, there is still oxygen left, and products such as CO and CO_2 are formed. The temperature has a very steep gradient in the inner layer and increases significantly. The zone where the product composition does not vary significantly anymore is called *postflame zone*. It is possible to notice how intermediate species, like for example CH_20, are characterized by a peak in the inner layer. These species would be perfect candidate for Laser Induced Fluorescence (LIF) measurements to track the flame front. LIF of the intermediate species is in practice more difficult and very often OH radicals are used to visualize the flame front, although this species are characteristic of the oxidation layer/postflame zone (Fig. 2.4). The profile of NO (the mass fraction has been multiplied by a factor 1000 for better visualization) is also shown. One may note the correlation of NO with the higher temperature in the postflame zone, as discussed in Section 2.2.2.2. The velocity at which the flame propagates towards the fresh mixture is called *laminar flame speed* and it is usually indicated as S_L. A simple expression is given by the theory of Mallard and Le Chatelier [77]:

$$S_L = \left(\frac{k_{th}}{\rho c_P} \frac{T_f - T_i}{T_i - T_0} w \right)^{1/2} \tag{2.12}$$

where k_{th} is the thermal conductivity, c_P is the specific heat, T_0 and T_i are the temperatures at the beginning and at the end of the preheat zone respectively, T_f is the temperature at the exit of the reaction zone, w is the reaction rate. It is important to remark that the laminar flame speed is a characteristic of the mixture. S_L has a maximum for $\Phi \simeq 1$, because the temperature of the burnt gases is maximum at stoichiometric conditions. At $\Phi = 1$ combustion would be faster but at the same time stoichiometric equivalence ratio is undesirable because of the large NOx emission levels.

2.3.1.4 Turbulent premixed flames

The interaction of turbulence with the flame is complex due to the strong coupling between the two non-linear phenomena. For very thin flames, the main effect of turbulence is that the eddies tend to wrinkle and corrugate the flame front. The flame area is increased and therefore also the combustion rate increases. An explanation was given in 1940 by Damköhler who developed a simple theoretical expression for the turbulent flame speed propagation. One can consider a turbulent flame as a corrugated laminar flame with local laminar flame speed S_L. Balancing the mass flux through the instantaneous turbulent flame front area A_L with the one through the equivalent laminar surface A_M, which is considered to move with the turbulent speed S_T (Fig. 2.5), one obtains:

$$\dot{m} = \rho S_L A_L = \rho S_T A_M \tag{2.13}$$

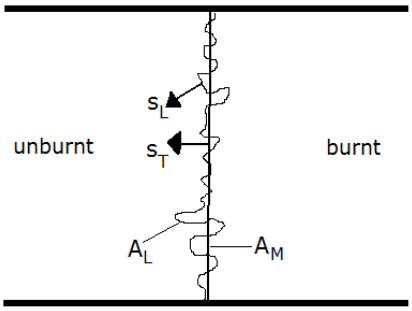

Figure 2.5: Sketch of a flame wrinkled by turbulence.

Unlike laminar flames, the propagation speed depends on the flow characteristics as well. Reshaping Eq. (2.13) shows that the ratio between turbulent and laminar flame speed is equal to the ratio of the surfaces. Clearly, the turbulent flame speed will be higher since the turbulent flame area is larger:

$$\frac{S_T}{S_L} = \frac{A_L}{A_M} \tag{2.14}$$

In reality the situation is more complex. When increasing the Reynolds number, the effect becomes non-linear and the eddies eventually quench the flame because

of high shear and cooling. The flow field can then affect the flame in contrasting ways. On the other hand, it is not only the turbulence affecting the flame, the flame affects the flow as well. Across the flame the flow undergoes a quick change in temperature, density, viscosity. The Reynolds number is reduced in the burnt gases, which in some cases can lead to *relaminarization*, but because of the density change across the flame, the flow is also strongly accelerated leading to instability. These coupled non-linear phenomena are rather complex and depend on different parameters [70]. Two non-dimensional numbers can be defined, the *Damköhler* number Da and the *Karlovitz* number Ka. They both relate chemical and flow time scales, but using different characteristic scales within the turbulent spectrum. The Damköhler number is defined as the ratio between the integral time scale τ_0 and the chemical time scale τ_c. The integral time scale can be expressed as the integral lenght scale l_0 over the velocity fluctuations u'. Indicating with δ_L the laminar flame thickness, the chemical time scale can be expressed as $\frac{\delta_L}{S_L}$, which represents the time in which a laminar flame propagates over the distance of one flame thickness. The Damköhler number is therefore [70]:

$$Da = \frac{\tau_0}{\tau_c} = \frac{l_0 S_L}{\delta_L u'} \tag{2.15}$$

The Karlovitz number instead compares the chemical time scale with the Kolmogorov time scale [70]:

$$Ka = \frac{\tau_c}{\tau_\eta} = \frac{\delta_L u_\eta}{\eta S_L} = \left(\frac{l_0}{\delta_L}\right)^{-\frac{1}{2}} \left(\frac{u'}{S_L}\right)^{\frac{3}{2}} \tag{2.16}$$

According to the values of these parameters, the behaviour of turbulent premixed flames can be characterized through a schematic diagram (known as Borghi's diagram, Fig. 2.6):

- In the bottom left corner of the diagram the Reynolds number is below 1 and the regime is laminar
- When $Ka < 1$, the smallest eddies (Kolmogorov scales) are bigger than the flame thickness. The eddies cannot enter the reaction layer and turbulence can only wrinkle the laminar flame front. If $u' < S_L$ the regime is called *wrinkled flamelets*, if $u' > S_L$ the regime is called *corrugated flamelets*: formation of pockets of burnt and fresh gases is possible [70].
- When $Ka > 1$, the Kolmogorov eddies can interact with the flame. In the range $1 < Ka < 100$, the smallest eddies can interact with the preheat zone but not with the inner layer: the reaction layer is thickened and this regime is referred to as *thin reaction zones*, or *thickened-wrinkled*
- When $Ka > 100$ the Kolmogorov eddies can enter the inner layer. The structure of the flame is not laminar anymore. This regime is called *Broken reaction zones* or *distributed combustion*.

- For $Da < 1$, the large scales turbulent mixing time is smaller than the chemical time: the mixing is very fast and the reaction rate is limited by chemistry. This regime is often called *Well stirred reactor* [70].

Real gas turbines feature very high Reynolds number ($Re = O(10^{6-7})$). The Kolmogorov scales are very small and interact with the inner layer. Real gas turbines therefore typically operate in the broken reaction zones (thickened flame), as sketched in Fig. 2.6. Laboratory scaled combustors typically work at lower Re in the regime of wrinkled-thickened flame with Karlovitz number around unity. This is for example the case for the Lisbon burner [24, 61]. As it will be clarified in the following, the other burner investigated in this thesis, the TARS burner, is characterized by small scale turbulence and is estimated to operate at high Karlovitz numbers, see Fig. 2.6.

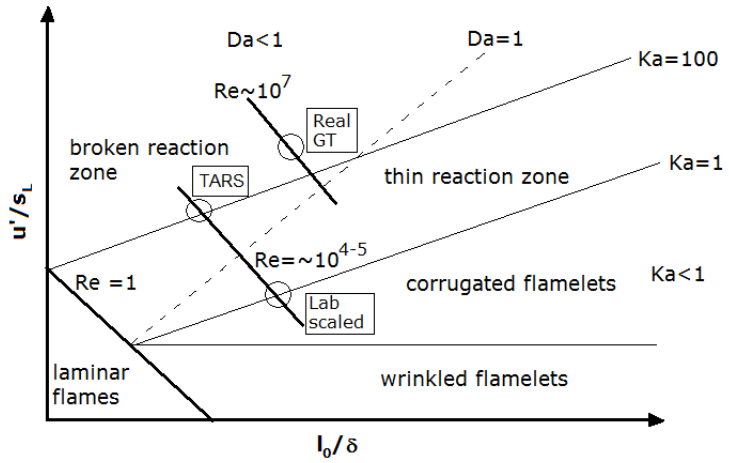

Figure 2.6: Combustion diagram for turbulent premixed combustion.

2.4 LES of turbulent reacting flows

2.4.1 Flow equations and boundary conditions

The equations describing the motions of fluids are the Navier-Stokes equations which describe the conservation of mass, momentum and energy. If there are different species in the fluid one may consider the conservation of mass of each of these species. In all the conservation laws one has to assume certain constitutive relations (i.e. relating often the fluxes to the gradients of the property under consideration). Thus, one assumes Newton-, Fourier- and Fick-law for the diffusion of momentum, heat and mass, respectively. With such assumptions and considering the low Mach number approximation (density does not depend on pressure but only on the temperature), and that the heat capacity C_p is constant, the governing equations read as follows [70]:

$$\frac{\partial \rho}{\partial t} + \frac{\partial}{\partial x_i}(\rho u_i) = 0 \tag{2.17}$$

$$\frac{\partial \rho u_j}{\partial t} + \frac{\partial}{\partial x_i}(\rho u_i u_j) = -\frac{\partial p}{\partial x_j} + \frac{\partial}{\partial x_i}\sigma_{ij} \tag{2.18}$$

$$\frac{\partial \rho T}{\partial t} + \frac{\partial}{\partial x_i}(\rho u_i T) = \frac{\partial}{\partial x_i}\lambda\frac{\partial T}{\partial x_i} + \dot{\omega}_T \tag{2.19}$$

$$\frac{\partial \rho Y_k}{\partial t} + \frac{\partial}{\partial x_i}(\rho u_i Y_k) = \frac{\partial}{\partial x_i}\rho D_k\frac{\partial Y_k}{\partial x_i} + \dot{\omega}_k \tag{2.20}$$

where u is the velocity, p is the pressure, $\sigma_{ij} = \mu\left(\frac{\partial u_i}{\partial x_j} + \frac{\partial u_j}{\partial x_i} - \frac{2}{3}\frac{\partial u_k}{\partial x_k}\delta_{ij}\right)$ is the viscous stress tensor, T is the temperature, λ is the thermal conductivity, $\dot{\omega}_T$ is the heat release. Y_k, D_k, and $\dot{\omega}_k$ are the mass fraction, the diffusivity and the reaction rate of species k, respectively. The system is then closed by the equation of state for ideal gases:

$$p = \rho(T)\Re T \tag{2.21}$$

A domain of interest defines where the equations are solved. At the boundary of the domain a certain number of conditions are needed. In fluid mechanics applications, typically boundary conditions are applied to the *inlet* (boundary where the flow enters the domain), to the *outlet* (boundary through which the flow goes out of the domain), and at the *walls* (boundaries which the flow cannot penetrate). For incompressible flows the character of the problem is elliptic in space (information can travel in all directions) and parabolic in time (information can travel only forward in time). For cases in which no physical boundaries are present close to the region of interest (e.g. flow around an airfoil or unconfined flames), the domain in which the equation are solved should be large enough to avoid significant influence of the boundaries on the region of interest. For cases in which there is geometrical periodicity (for example the flow around identical objects regularly arrayed), *periodical* boundary conditions can be applied at the boundaries: the outcoming velocity at a point on one side is equal to the incoming velocity on correspondent point on the opposite side. When for geometrical reasons the flow is expected to be symmetric, *symmetry* conditions can be applied: the variables are reflected at the limit of the domain. In this way computational time can be saved solving the equations on a smaller domain.

2.4.2 Averaged/filtered equations

Since turbulent flows are chaotic by definition, there is limited meaning in the instantaneous values (pictures, measured or computed flow fields). If the flow is statistically stationary, one may consider the statistical properties of the flow which are the only ones that one is able to reproduce in different realizations. Since only averaged quantities are of interest, one may introduce different types of filtering to reflect

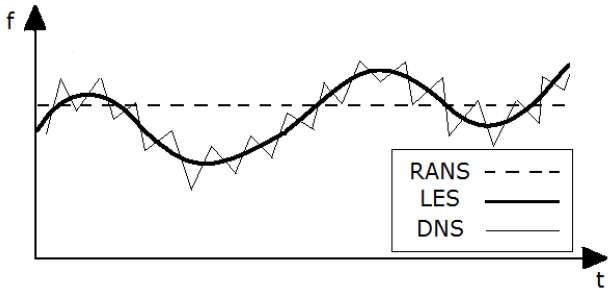

Figure 2.7: Sketch of the time evolution of a generic variable f, using RANS, LES and DNS.

the properties that are of interest. Depending on the filtering procedure, in Computational Fluid Dynamics (CFD) three main approaches are possible: Reynolds Averaged Navier-Stokes (RANS), Large Eddy Simulation (LES), Direct Numerical Simulation (DNS). As it will be clarified in the following, filtering introduces extra unknown terms for which models are needed. The models for the extra terms appearing in the filtered equations are presented in Sections 2.4.3 and 2.4.5. In Fig. 2.7 it is sketched how RANS, LES and DNS would differently capture a generic variable f (for example a velocity component in one point) as a function of time.

- **Reynolds Averaged Navier Stokes (RANS)**: Historically, one has been using the so called Reynolds averaging. A generic variable f can be decomposed into an averaged value $\bar{f}$ plus a fluctuating component f', such that: $f = \bar{f} + f'$. In RANS the instantaneous Navier-Stokes equations are averaged in time:

$$\bar{f} = \lim_{T\to\infty} \frac{1}{T} \int_{t_0}^{t_0+T} f(t)\, dt \tag{2.22}$$

  where T is the period of integration. The averaging procedure introduces an extra unknown quantity, often referred to as the *Reynolds stresses tensor*. This is a *closure* problem and the extra term needs to be modeled. As shown in Fig. 2.2, this model has to take into account all the turbulent scales in the spectrum. For flows of practical interest, the time required to obtain a solution on modern computer is typically of the order of hours or days. For this reason RANS is the most popular CFD tool used in industry. In RANS, one obtains only the steady state solution. It is therefore not suited for the scope of this thesis, which is to study the dynamics of flows and flames.

- **Direct Numerical Simulation (DNS)**: No filtering is performed and the instantaneous equations are directly solved. The whole turbulent kinetic energy is resolved, all the way down to the Kolmogorov scale (Fig. 2.2). The grid spacing Δx should be considerably smaller than the Kolmogorov scale: $\eta \gg \Delta x$. If one wants the size of the domain to be at least one integral scale

l_0, it is possible to estimate the minimum number of grid points N in each direction, so that $l_0 = N\Delta x$, through Eq. (2.6):

$$N > Re^{3/4} \tag{2.23}$$

Since one solves the DNS equations in time, one needs also $O(Re^{3/4})$ time steps, all these leading to an operation count proportional to Re^3. For the high Reynolds numbers typical of practical applications, a very fine grid with a large number of grid points is needed, and DNS is computationally not feasible.

- **Large Eddy Simulation (LES)**: In this case the instantaneous Navier Stokes equations are filtered in space (either spectral or physical space):

$$\bar{f}(x) = \int f(x')F_\Delta(x - x')\,dx' \tag{2.24}$$

where $F_\Delta(x)$ is the LES filter, of width Δ. Typical filters are the cut-off filter in the spectral space, the top-hat or the Gaussian filter in the physical space. After the filtering procedure, several unknown terms appear in the equations, as it will be shown in the following. In LES, the filtered variable $\bar{f}$ is solved for and the unclosed terms represent the unresolved subgrid scales (SGS) fluctuations. The turbulent kinetic energy of the scales larger than the width of the filter size is resolved (Fig. 2.2), while only the effect of turbulent structures smaller than the filter (subgrid scales) needs to be modeled. Typical models developed in the LES framework are summarized in Section 2.4.3. Because of its capability to resolve in time a large fraction of the turbulent kinetic energy, LES is a suitable tool to address the unsteady phenomena object of this thesis. The price to be paid is in terms of computational time: a typical run can require several weeks to obtain converged statistics. Although it is still a tool which is mostly used in the academy, the interest of the industry towards LES is constantly increasing.

For reacting flows, the density cannot be considered as a constant and to simplify the equations Favre (density weighted) filtering is applied:

$$\tilde{f} = \frac{\overline{\rho f}}{\overline{\rho}} \tag{2.25}$$

Favre filtered quantities are indicated with a tilde and the density weighted filtering operator is then expressed as:

$$\bar{\rho}\tilde{f}(x) = \int \rho f(x')F_\Delta(x - x')\,dx' \tag{2.26}$$

A generic variable f can be decomposed into the Favre-filtered value $\tilde{f}$ plus a subgrid component f'', such that: $f = \tilde{f} + f''$. One should note that for filtering,

$\tilde{f}'' \neq 0$, $\widetilde{\tilde{f}f''} \neq 0$, $\tilde{f} \neq \widetilde{\tilde{f}}$. It should be remarked that the exchange of the filtering and derivative operation, $\widetilde{\frac{\partial f}{\partial x}} = \frac{\partial \tilde{f}}{\partial x}$, is not generally valid. The uncertainities due to this operator are generally assumed to be included in the subgrid models [70]. Equations (2.17-2.21) are filtered and read [70]:

$$\frac{\partial \overline{\rho}}{\partial t} + \frac{\partial}{\partial x_i}\left(\overline{\rho}\tilde{u}_i\right) = 0 \tag{2.27}$$

$$\frac{\partial \overline{\rho}\tilde{u}_j}{\partial t} + \frac{\partial}{\partial x_i}\left(\overline{\rho}\tilde{u}_i\tilde{u}_j\right) + \frac{\partial \overline{p}}{\partial x_j} = \frac{\partial}{\partial x_i}\left(\overline{\sigma_{ij}} + \overline{\rho}\tilde{u}_i\tilde{u}_j - \overline{\rho}\widetilde{u_i u_j}\right) \tag{2.28}$$

$$\frac{\partial \overline{\rho}\tilde{T}}{\partial t} + \frac{\partial}{\partial x_i}\left(\overline{\rho}\tilde{u}_i\tilde{T}\right) = \frac{\partial}{\partial x_i}\left(\overline{\rho}\tilde{u}_i\tilde{T} - \overline{\rho}\widetilde{u_i T} + \overline{\lambda\frac{\partial T}{\partial x_i}}\right) + \tilde{\dot{\omega}}_T \tag{2.29}$$

$$\frac{\partial \overline{\rho}\tilde{Y}_k}{\partial t} + \frac{\partial}{\partial x_i}\left(\overline{\rho}\tilde{u}_i\tilde{Y}_k\right) = \frac{\partial}{\partial x_i}\left(\overline{\rho}\tilde{u}_i\tilde{Y}_k - \overline{\rho}\widetilde{u_i Y_k} + \overline{\rho D_k\frac{\partial Y_k}{\partial x_i}}\right) + \tilde{\dot{\omega}}_k \tag{2.30}$$

$$\bar{p} = \rho(\bar{T})\Re\tilde{T} \tag{2.31}$$

2.4.3 Turbulence modeling

After the filtering procedure, several extra unknown terms appear in the equations. In the momentum equation, the aforementioned SGS tensor appears, denoted as τ_{ij}

$$\tau_{ij} = \overline{\rho}\left(\tilde{u}_i\tilde{u}_j - \widetilde{u_i u_j}\right) = \overline{\rho}\tilde{u}_i\tilde{u}_j - \overline{\rho}\left(\widetilde{\tilde{u}_i\tilde{u}_j} + \widetilde{u_i''\tilde{u}_j} + \widetilde{\tilde{u}_i u_j''} + \widetilde{u_i'' u_j''}\right) \tag{2.32}$$

In LES the model to close the momentum equation is less crucial than in RANS because only the subgrid scale turbulence needs to be taken into account. The large eddies, which depend strongly on the particular geometry, are resolved. In the LES models, only a small fraction of the turbulent kinetic energy needs to be accounted for and eventually, the finer the filter width, LES should tend to DNS. According to the turbulent energy cascade theory, the kinetic energy is in average transferred to the small scales where it is dissipated. Instantaneously, it can happen that energy is transferred from small to larger scales (*backscatter*). One should express the SGS stresses τ_{ij} in terms of known filtered quantities, and a good SGS model should take into account both dissipation and backscatter. Several models have been proposed for the closure of the filtered equations. For more detailed discussions, the reader is referred to [40,78]. A brief summary of the most popular LES models is given in the following.

2.4.3.1 Smagorinsky Model

A typical approach to close the problem is to follow the *Boussinesq*'s hypothesis. The turbulent fluctuations increase the mixing and are modelled in analogy to the

diffusion term. A *turbulent viscosity* μ_Δ is introduced and the SGS stresses are rewritten as

$$\tau_{ij} = \overline{\rho}\left(\tilde{u}_i\tilde{u}_j - \widetilde{u_i u_j}\right) = \mu_\Delta\left(\frac{\partial\tilde{u}_i}{\partial x_j} + \frac{\partial\tilde{u}_j}{\partial x_i} - \frac{2}{3}\frac{\partial\tilde{u}_k}{\partial x_k}\delta_{ij}\right) \tag{2.33}$$

The Smagorinsky model [79] is based on the Boussinesq's hypothesis, and is a direct extrapolation of earlier RANS models. The turbulent viscosity is expressed as:

$$\mu_\Delta = \overline{\rho}(C_S\Delta)^2|\tilde{S}| \tag{2.34}$$

where Δ is the filter width, C_S is a constant, $\tilde{S}$ is the filtered rate of strain. The advantage of this model is its simplicity, which makes it very popular. It has drawbacks: it is too dissipative, it does not account for backscatter, it overpredicts viscosity near the walls, it does not converge to 0 for laminar flows.

2.4.3.2 Scale Similarity Model

The idea behind this model [80] is that the unresolved scales should behave similarly to the resolved ones. In particular the assumption is that the most active subgrid scales are those closer to the cutoff wave number, and that the scales with which they interact most are those right above the cutoff [40]. A test filter wider than Δ is introduced, denoted with a hat.

$$\tau_{ij} = \overline{\rho}\left(\tilde{u}_i\tilde{u}_j - \widetilde{u_i u_j}\right) = \overline{\rho}\left(\hat{\tilde{u}}_i\hat{\tilde{u}}_j - \widehat{\tilde{u}_i\tilde{u}_j}\right) \tag{2.35}$$

This model has the advantage that it accounts for some backscatter. The main disadvantage is that it is not dissipative enough. Moreover an extra filter is introduced, which makes it computationally moderately more expensive, and the spatial resolution is reduced.

2.4.3.3 Germano's Dynamic model

With this model Germano et al. [81] improved the Smagorinsky model. The idea is that the coefficient C_S in the Smagorinsky model is not given as an a-priori constant but is dynamically computed during the calculations, based on the behaviour of the smallest resolved scales. The advantage is that it is free from model parameters. Also here a wider filter, denoted with a hat, is introduced. The subtest stresses with the broader filter are:

$$T_{ij} = \overline{\rho}\left(\hat{\tilde{u}}_i\hat{\tilde{u}}_j - \widehat{\widetilde{u_i u_j}}\right) \tag{2.36}$$

The parameter C_S is computed through the Germano identity, which relates the resolved stresses $L_{ij} = \overline{\rho}\left(\hat{\tilde{u}}_i\hat{\tilde{u}}_j - \widehat{\tilde{u}_i\tilde{u}_j}\right)$ to the unresolved subgrid stresses, filtered with the broader filter $\hat{\tau}_{ij} = \overline{\rho}\left(\widehat{\tilde{u}_i\tilde{u}_j} - \widehat{\widetilde{u_i u_j}}\right)$ and subtest stresses T_{ij} [40]:

$$L_{ij} = T_{ij} + \hat{\tau}_{ij} \tag{2.37}$$

T_{ij} and τ_{ij} are expressed with the Smagorinsky model and in this way it is possible to compute dynamically the constant C_S. One of the disadvantages of this model is that the identity in Eq. (2.37) is overdetermined (five independent equations for one coefficient) and needs further treatements. One possibility is to reduce the error by means of a least squares method [82]. This fact, together with the fact that an additional filter is needed, increases the computational efforts.

2.4.3.4 Filtered Smagorinsky

The Filtered Smagorinsky model [83] proposes to iterate a Laplacian high-pass test filter n times over the velocity field, $u_{i_{HP}} = HP^n(\tilde{u}_i)$, before computing the strain tensor $\tilde{S}_{ij_{HP}}$. The idea is that in this way the large scales do not contribute to the eddy viscosity for the SGS. Therefore one takes $\mu_\Delta = \overline{\rho} c_3 \Delta^2 |\tilde{S}_{ij_{HP}}|$.

2.4.3.5 Implicit LES (ILES)

The idea is not to use any subgrid model at all. It is based on the assumption that when the grid or the filter width is decreased, the unresolved fraction of the turbulent kinetic energy is getting smaller and smaller (i.e. second order in the filter size), and the effect of the SGS is of the same order of the truncation error (TE) introduced by discrete schemes. The numerical schemes include dissipation in order to ensure convergence of the numerical procedure. The rationale is that this dissipation (also of order of at least two) does not determine the rate of turbulent energy transfer to the small scales (which by Kolmogorov's theory is dissipation independent). Thus, if one has a spatial resolution of the Taylor scale or better, the effects of physical and numerical viscosity, do not show in the resolved scales (i.e. the large eddies). The implicit SGS model is thus closely connected to the specific numerical algorithm (Section 3.1.2), as theoretically stated in [84, 85], yet the results are expected to be independent of the numerical scheme or algorithm. In the named papers it was shown that the leading truncation error in Monotonically Integrated LES (MILES) may formally acts as an implicit SGS model. The WENO and the other schemes used herein have been proved to be successful in simulations of widely different engineering flows [84–87], and in particular in the context of swirl-stabilized premixed flames [24, 88–90].

2.4.4 Closures for the other SGS terms

Several other terms in the energy and species equations need to be modeled in order to get a closed problem. For high Re, the filtered momentum, heat and mass diffusion terms are often approximated as $\tilde{\sigma}_{ij} = \mu_\Delta \left(\frac{\partial \tilde{u}_i}{\partial x_j} + \frac{\partial \tilde{u}_j}{\partial x_i} - \frac{2}{3} \frac{\partial \tilde{u}_k}{\partial x_k} \delta_{ij} \right)$, $\overline{\lambda} \frac{\partial \tilde{T}}{\partial x_i}$, $\overline{\rho} \overline{D_k} \frac{\partial^2 \tilde{Y}_k}{\partial x_i^2}$. The subgrid scalar transport terms in the energy and species equations ($\overline{\rho} \tilde{u}_i \tilde{T} - \overline{\rho u_i T}$; $\overline{\rho} \tilde{u}_i \tilde{Y}_k - \overline{\rho u_i Y_k}$) are usually modeled with a simple gradient assumption.

For example: [70]

$$\overline{\rho}\tilde{u}_i\tilde{Y}_k - \overline{\rho}\widetilde{u_i Y_k} = -\frac{\mu_\Delta}{Sc_k}\frac{\partial \tilde{Y}_k}{\partial x_i} \tag{2.38}$$

where Sc_k is the Schmidt number of species Y_k and the turbulent viscosity μ_Δ is obtained through the subgrid stresses models. In reacting flows, the main problem is represented by the unclosed reaction rates $\overline{\dot{\omega}}_k$. Typical models developed for the closure of the reaction rates in the context of Large Eddy Simulation of turbulent premixed combustion are presented in Section 2.4.5.

2.4.5 Combustion modeling

When simulating reacting flows by means of LES, the main difficulty lies in the fact that the reaction layer is in most situations thinner than the grid size and therefore cannot be resolved. Models for the filtered reaction rates $\tilde{\dot{\omega}}_k$ are then needed. Several formulations have been proposed in the literature. It should be remarked that LES of turbulent combustion is a relatively recent field of research. There is a variety of models that are valid in different regimes [70]. No "ultimate model", generally valid everywhere, has emerged so far. For premixed combustion a problem is also the lack of comprehensive experimental data for validation [91]. In this section, the main models are described briefly. For a more detailed discussions of the various possibilities, the reader is referred to [70, 91, 92].

2.4.5.1 ILES

The simplest possible model is to compute the production rate of the k-th species directly through the Arrhenius expression, Eq. (2.9). In analogy to SGS modeling, this implies an ILES closure for the filtered reaction rate terms: $\widetilde{\dot{\omega}}_k = \widetilde{f(Y_k, T)} = f(\tilde{Y}_k, \tilde{T})$, (see [93]). Basically, it is assumed that each computational cell is a perfectly stirred reactor, i.e. that the subgrid mixing is faster than chemical reactions. In [93] it was shown that this assumption is reasonable if the Karlovitz number is relatively high and the mesh resolution is fine enough. In this thesis, such model has been used in the simulations of the TARS burner (Papers V [66] and VI [67]. Given the highly turbulent flow with very fine scales due to the narrow vanes of the TARS, high Karlovitz number flames are expected for this burner. For example, in Paper VI [67], it was estimated that $Ka \simeq 160$, supporting the perfectly stirred reactor hypothesis. Such model should then include chemical schemes that are tailored for LES. In this thesis, both global two-steps [94] (in Paper V [66]) and four-steps [95] (in paper VI [67]) chemical schemes have been used.

2.4.5.2 Thickened flame model

The thickened flame model [8, 70, 94, 96] was originally proposed by Butler and O'Rourke [97]. The main idea of this model is to artificially thicken the flame front, so that it can be resolved on the given grid. From the laminar flame theory the

flame speed and the flame thickness can be expressed as:

$$S_L \propto \sqrt{D_{th}B}; \qquad \delta_L \propto \frac{D_{Th}}{S_L} = \sqrt{\frac{D_{Th}}{B}} \tag{2.39}$$

where D_{th} is the thermal diffusivity and B is a constant. Multiplying D_{th} and dividing B by the same factor F, the laminar flame speed is not changed while the thickness is artificially increased. One of the main disadvantages of this method is that the Damköhler number is also decreased of the same factor F. Colin et al. [96] introduced an efficiency function E to correct for the unresolved features. In particular it takes into account the subgrid wrinkling to modify the flame speed as well.

2.4.5.3 Filtered density function

The Filtered density function model [70,98] is based on a statistical approach. If one knows the probability density function (pdf) of the variables of interest (for example mass fractions of the species, temperature) in all the points, then the reaction rate can be expressed in terms of the probability functions [70]:

$$\tilde{\dot{\omega}} = \int_{Y_1,Y_i,\cdots,Y_N,T} \omega(Y_1,Y_i,\cdots Y_N,T)p(Y_1,Y_i,\cdots Y_N,T)dY_1dY_i\cdots dY_NdT \tag{2.40}$$

The pdf can be extracted from experimental data or DNS, can be presumed, can be transported with a dedicated balance equation. The advantage of these models is that no closure is needed. A drawback lies in the fact that the pdfs are difficult to measure or to guess. Moreover, if transport equations are involved, they are computationally expensive.

2.4.5.4 G-equation

The G-equation model is based on the hypothesis that the flame is in the flamelet regime. The turbulent structures cannot modify the reaction layer, but only wrinkle and corrugate the flame front. This model considers the flame to be a propagating surface represented by the variable G. The equation governing such motion is the following [99]:

$$\frac{\partial\overline{\rho}\tilde{G}}{\partial t} + \frac{\partial\overline{\rho}\tilde{u}_i\tilde{G}}{\partial x_i} = \rho_0\overline{S}_T|\nabla\overline{G}| \tag{2.41}$$

where S_T is the flame propagation speed relative to itself, in a direction normal to the flame front. In order to close Eq. (2.41), the turbulent velocity $\overline{S_T}$ needs to be modeled. Usually the following expression is used [70]

$$\frac{\overline{S}_T}{S_L} = 1 + \alpha\left(\frac{\overline{u'}}{S_L}\right)^n \tag{2.42}$$

where the parameters α and n and the subgrid velocity fluctuation u' need to be estimated. This technique is very popular for the simulation of turbulent premixed

flames [100–102], but has drawbacks: the turbulent flame speed has not a well defined and accepted model, Eq. (2.41) is prone for numerical instability and requires "renormalization", it tends to generate cusps, it is not straightforward to couple with mass fraction or energy balance equations [70].

2.4.5.5 Progress variable; the c-equation

In this model the combustion process is summarized only by one variable, c, which is called the *progress variable*. This variable is defined in terms of properties of the unburnt (subscript u) and burnt (subscript b) gases. For example the temperatures T_u and T_b or the fuel mass fractions Y_F^u and Y_F^b can be used [70]:

$$c = \frac{T - T_u}{T_b - T_u}, \qquad c = \frac{Y_F - Y_F^u}{Y_F^b - Y_F^u} \tag{2.43}$$

In this way it varies between the values 0 in the unburnt gases and 1 in the completely burnt gases. A transport equation is derived from the energy equation (2.19). This method is particularly advantageous in terms of computational time, because there is no need to consider several species. Only one equation (the so called c-equation) is used, while the properties of the laminar structure of the flame can be computed with detailed chemistry. The c-equation reads [70]:

$$\frac{\partial \rho c}{\partial t} + \frac{\partial}{\partial x_i}\left(\rho u_i c\right) = \frac{\partial}{\partial x_i}\left(\rho D_{th}\frac{\partial c}{\partial x_i}\right) + \dot{\omega}_c = \rho S_d \sqrt{\frac{\partial c}{\partial x_i}\frac{\partial c}{\partial x_i}} \tag{2.44}$$

where S_d is the local flame displacement speed. The filtered LES equation for c reads:

$$\frac{\partial \overline{\rho}\tilde{c}}{\partial t} + \frac{\partial}{\partial x_i}\left(\overline{\rho}\tilde{u}_i\tilde{c}\right) + \frac{\partial}{\partial x_i}\left(\overline{\rho u_i c} - \overline{\rho}\tilde{u}_i\tilde{c}\right) = \frac{\partial}{\partial x_i}\overline{\rho D_{th}\frac{\partial \tilde{c}}{\partial x_i}} + \overline{\dot{\omega}}_c = \overline{\rho S_d \sqrt{\frac{\partial c}{\partial x_i}\frac{\partial c}{\partial x_i}}} \tag{2.45}$$

Usually the subgrid transport term $\frac{\partial}{\partial x_i}\left(\overline{\rho u_i c} - \overline{\rho}\tilde{u}_i\tilde{c}\right)$ is modeled through a simple classical gradient expression. Several closure are possible for the filtered reaction rates. One possibility is for example the Flame Surface Density (FSD) model [70, 103]:

$$\overline{\rho S_d \sqrt{\frac{\partial c}{\partial x_i}\frac{\partial c}{\partial x_i}}} = \rho_u S_L \Sigma \tag{2.46}$$

Σ is the subgrid flame surface density, i.e. the ratio between the flame area and the subgrid volume. A closure for this term is needed. Closures have been proposed both with algebraic expressions or with a transport equation for Σ [103]. With respect to the G-equation, this model relies on a more physical ground.

2.4.5.6 Filtered flamelet model with tabulated chemistry

In this work, a similar approach is followed and a flamelet model with a c-equation is used (in Paper I). The unclosed terms in Eq. (2.45) are modeled through a

diffusion term plus a production term. Introducing the diffusion coefficient D_0:

$$\frac{\partial \overline{\rho}\tilde{c}}{\partial t} + \frac{\partial}{\partial x_i}\left(\overline{\rho}\tilde{u}_i\tilde{c}\right) = \rho_0 D_0 \frac{\partial^2 \tilde{c}}{\partial x_i^2} + \pi\left(\tilde{c}, D_0\right) \tag{2.47}$$

It should be noted that the production term $\pi\left(\tilde{c}, D_0\right)$ is also dependent on the diffusion coefficient and incorporates both the filtered reaction rate and the subgrid transport terms. In this way it is avoided to introduce two separate models and correct flame propagation is ensured. The production term (burning rate) is modeled as a filtered Dirac function (with a Gaussian filter of size Δ) [88]:

$$\pi(x) = \rho_u S_L \frac{6}{\pi}\frac{1}{\Delta} exp\left(-\frac{6x^2}{\Delta^2}\right) \tag{2.48}$$

and the structure of the flame is obtained through a 1D filtered c-equation. A parameter $a = \rho_u \Xi S_L \Delta / \rho_0 D_0$ results from the 1D equation which determines the filtered flame structure [88, 90]. This parameter expresses the ratio between the burning rate and diffusion. High values of the parameter a lead to a thinner flame front, low values correspond to a thicker one. It should be noted that the symbol Ξ denotes a factor accounting for the subgrid wrinkling. The wrinkling factor is expressed as [104]

$$\Xi = MAX\left[\left(\Gamma\frac{\sqrt{u_{\Delta_i}u_{\Delta_i}}}{S_L}\right)^{D-2}, 1\right] \tag{2.49}$$

where Γ is an efficiency function introduced in [105] and D is a fractal dimension. The fractal dimension is modeled as in [104]:

$$D = \frac{2.05}{1+\sqrt{u_{\Delta_i}u_{\Delta_i}}/S_L} + \frac{2.35}{1+S_L/\sqrt{u_{\Delta_i}u_{\Delta_i}}} \tag{2.50}$$

u_{Δ_i} indicates a subgrid velocity fluctuation vector and it is modeled following [96]

$$u_{\Delta_i} = 2\Delta^3 \frac{\partial^2}{\partial x_l^2}\left(\varepsilon_{ijk}\frac{\partial \tilde{u}_k}{\partial x_j}\right) \tag{2.51}$$

where ε_{ijk} is the Levi-Civita symbol. This model is based on geometrical considerations and it enables a simple algebraic closure. It is therefore preferred to less natural and computationally more expensive closures with a transport equation for Ξ, such as for example the one in [106]. Eq. (2.47) is closed expressing the right hand side as a function of the parameter a.

$$\frac{\partial \overline{\rho}\tilde{c}}{\partial t} + \frac{\partial}{\partial x_i}\left(\overline{\rho}\tilde{u}_i\tilde{c}\right) = \frac{\rho_u S_L \Xi \Delta}{a}\frac{\partial^2 \tilde{c}}{\partial x_i^2} + \rho_u S_L \Xi \frac{1}{\Delta}\Pi_c\left(\tilde{c}, a\right) \tag{2.52}$$

The production term is tabulated as a function of the progress variable and the parameter a before starting the simulations. $\Pi(\tilde{c}, a)$ is stored in look-up tables accessed during the computations [24, 88, 90]. A visualization of the production term distribution is reported in Fig. 2.8. More details about the model are found in [24, 88, 90]. This flamelet model has been successfully used to simulate turbulent premixed flames [89,90] and in particular swirl-stabilized turbulent premixed flames [24, 88]

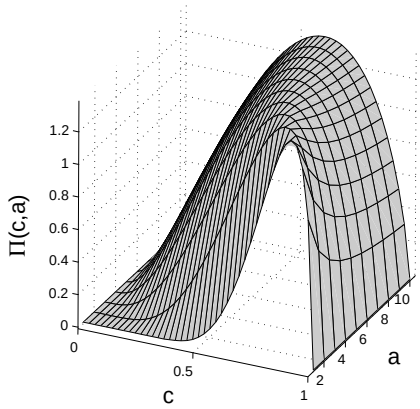

Figure 2.8: Production term $\Pi_c(\tilde{c}, a)$.

2.5 Stabilizaton and combustion instabilities

2.5.1 Swirl stabilization

A flame is stabilized or, more correctly expressed, anchored, when its velocity of propagation matches the incoming flow speed. A way to achieve this is to place a *bluff body* in the middle of the flow and anchor the flame in the wake that it generates. The main disadvantage of the bluff body stabilization is that there is the necessity of having a body close to the flame with related consequences on the materials. The preferred way to stabilize a flame in modern combustors is instead by vortex breakdown. The recirculation is created by aerodynamical means: the incoming mixture is given a swirling motion; as the swirling jet expands in radial direction, an adverse pressure gradient is created in the centerline. The main parameter controlling the behaviour of swirling jets is the swirl number S. Several definitions have been proposed, here it is defined as the ratio of the axial flux of tangential momentum to the axial flux of axial momentum times the equivalent exit radius [7]. If S is large enough, breakdown of the vortex occurs and a reversed flow is formed in the center (see Fig. 2.9). In the literature the recirculating bubble is usually referred to as Central Recirculation Zone (CRZ) or Inner Recirculation Zone (IRZ). In Fig. 2.9 the typical flow configuration for a swirl-stabilized combustor is reported [34]. Besides the IRZ, an Outer Recirculation Zone (ORZ) is also found. It is usually a toroidal vortex which is formed because of the sudden expansion and the presence of the combustor walls. In between the two recirculating zones, there is the annular swirling jet. An outer shear layer is generated between the ORZ and the jet, an inner one between the jet and the IRZ. Such complex aerodynamics are subject to dynamics and instabilities. Some of these are listed [34].

- Internal Recirculation Zone dynamics
  - axial and radial flow oscillations

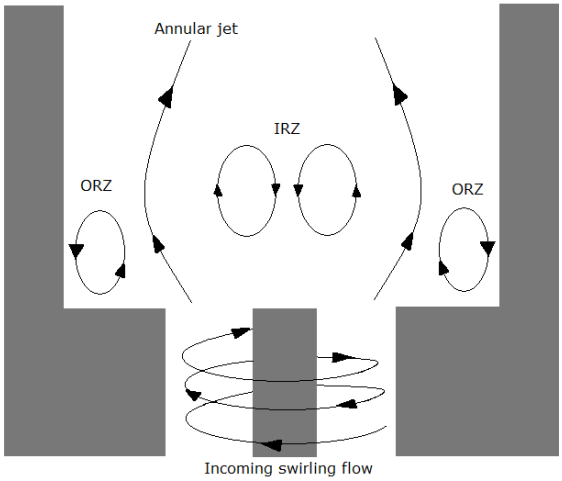

Figure 2.9: Sketch of typical swirl-stabilized combustor flow configuration.

  - PVC

- Swirling jet dynamics
  - large scale coherent structures
  - helical structures
  - central counter rotation
- Shear layers dynamics
  - vortex roll-up due to Kelvin-Helmoltz instability
  - centrifugal instabilities
- Outer Recirculation Zone dynamics
  - axial and radial oscillations
  - periodical shrinkage
  - periodical detachments

These systems of vortices are interacting with each other in a non-linear manner which is not always completely understood. Both the large and the small scales associated with the above mentioned structures affect the flame holding and steadiness of the flame/flow.

2.5.1.1 Precessing Vortex Core

Among the instabilities listed above, the PVC has been the subject of extensive research; a recent review can be found in [21]. The PVC is a 3-D unsteady asymmetric flow structure. It develops when a central vortex core precesses around the

axis of symmetry at a well defined frequency [5]. There are evidences that the PVC is essentially helical in nature [21]. It is usually related to the phenomenon of vortex breakdown. Typically is situated on the boundary of the recirculation zone [5] and originates at the stagnation point. In Fig. 2.5.1.1 a typical vortex core precessing around the axis is sketched (in a cross section perpendicular to the axis).

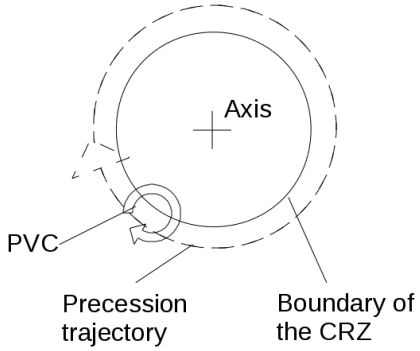

Figure 2.10: Sketch of a PVC after [21].

The PVC might have beneficial effects since it enhances turbulence intensity, and thereby mixing and combustion efficiency. However, being an unsteady coherent structure, it is largely undesirable, since it may possibly lead to resonance with the acoustic modes of the combustor itself. Such conditions can trigger thermo-acoustic instabilities.

2.5.2 Thermo-acoustic instabilities

The coupling between acoustic waves and flames is a topic of growing interest [70]. Unsteady heat-release is a source of acoustic waves. With unsteady heat release the density changes in time leading to pressure fluctuations that travel with the acoustic speed. Acoustic resonance may lead to structural fatigue and also to environmental issues (in form of combustion noise [17,18]). Most importantly, there is the problem of thermo-acoustic oscillations. The combustor is a confined chamber and the acoustic waves are reflected by the walls. They interact with the flow and inlet fuel/air feed. Resonance phenomena can happen if the pressure and the heat release are in phase. A sketch of the feedback loop is reported in Fig. 2.11. These phenomena are usually referred to as thermo-acoustic instabilities or combustion dynamics [6, 107]. Thermo-acoustic oscillations are in most cases undesirable as several problems can occur: noise, incomplete combustion with consequent emission of pollutants, flame quenching, vibrations that can even lead to serious mechanical damages. It should be remarked that the energy needed to sustain such unsteady motions is only a small part of the energy released by the combustion process. They constitute then one of the most challenging areas in combustion research [107]. A lot of efforts are made in order to gain deeper understanding of these phenomena therefore enabling their control [107, 108].

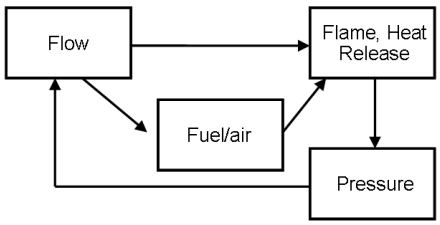

Figure 2.11: Flow chart of thermo-acoustic instabilities.

Generally these kind of instabilities are classified according to the frequency [5]. Low-frequency instabilities occur below 30-50 Hz and are usually related to incipient blow-out. Intermediate-frequencies, between 50-1000 Hz, usually correspond to the longitudinal mode of the combustion chamber and can relate to the coupling between fuel-air ratio and the acoustic oscillations. High frequency instabilities are instead often associated to tangential acoustical modes [5]. A simple parameter monitoring thermo-acoustic instabilities is the time averaged *Rayleigh* index G:

$$G = \frac{1}{T} \int \dot{\omega}_T(x,t) p(x,t)\, dt \tag{2.53}$$

where T is a time period, $\dot{\omega}_T(x,t)$ the unsteady heat release and $p(x,t)$ the acoustic pressure. A region of the combustor where oscillations are excited is characterized by $G > 0$ [70].

Combustion instabilities are not considered to be an issue for diffusion flames [5]. However they still represent a challenge for the design of modern LP low-NOx combustors, for a series of reasons: to achieve low emissions, one operates close to lean blow-out; the flame is compact and usually placed at one of the acoustic pressure nodes; no dilution air is supplied along the combustor liner (which in traditional diffusion flame type of combustors often acts as an acoustic attenuator) [5]; the absence of diffusive mixing time makes premixed flame more sensitive to acoustic excitation [21].

Chapter 3

Methods

3.1 Numerical methods

The Navier-Stokes set of equations (Eq. 2.17-2.20) is a *mathematical model* to describe the motion of fluids. It is a system of non-linear Partial Differential Equations (PDE). Analytical solutions are only possible if simplifying assumptions are made (for example, two dimensional potential flow). For the full 3-D set of time-dependent equations, a possibility is to get a numerical solution with the help of computers. The field of numerical methods applied to fluid dynamics is generally called *Computational Fluid Dynamics* (CFD). The equations are discretized into an algebraic system of equations which can be solved on computers [109]. They are solved on a discrete set of points in space, comprising a *grid* or *mesh*. Time is also discretized. Most often, the three common discretization methods are the *Finite Difference* (FD), the *Finite Volume* (FV) and the *Finite Elements*. These three discretizations are related since they use polynomials for approximating the continuous variables. A common approach for low Re computations on simple geometries is based on *spectral* approximations instead of polynomial ones, leading to a higher accuracy with given number of degrees of freedom. However, for most CFD applications polynomial based approaches are used to be able to handle non-trivial geometries. FD methods are popular in academy because of their simplicity and superior accuracy. A limitation is that complex geometries are difficult to handle. In this thesis, the FD approach was used in the simulation of the Lisbon burner (Paper I). An In-house code [110] was used for this scope. In contrast, FV methods, although at the price of accuracy loss, are suitable for complex geometries. Therefore we used a FV approach for the simulations of the TARS burner (Papers III,V,VI). Most commercial codes make use of FV Methods. We chose the Open Source CFD tool box OpenFOAM [111, 112]. It is a rather complete CFD library including both incompressible and compressible, non reacting and reacting solvers, and a wide range of models. One can access the source code, and possibly modify it according to one's own needs. In the following sections some details on the discretization methods and the softwares used in this thesis are briefly introduced.

3.1.1 Finite Difference

In the Finite Difference method, the variables and their discrete derivatives are stored at the grid points. The finite difference method enables to easily implement high-order accurate schemes. This is due to the fact that finite differences are

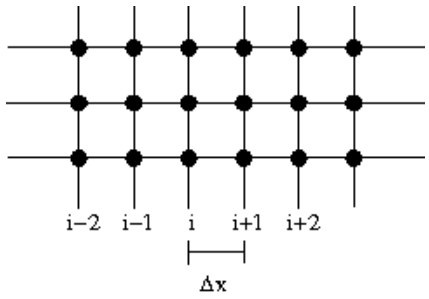

Figure 3.1: Sketch of a Cartesian structured grid.

practically only possible on structured grids on the computational space. As already stated, a limitation is that complex geometries may be more difficult to handle. A possibility to overcome this problem is the use of immersed boundary methods [113]. A possible way to derive a finite difference discretization scheme is by using Taylor expansions. An example is presented in the following. A Cartesian grid (see Fig. 3.1) $(x_{i-2}, x_{i-1}, x_i, x_{i+1}, x_{i+2}...)$, with equally spaced grid points ($\Delta x = x_{i+1} - x_i = h$) is considered. It is possible to express a variable ϕ at point x_{i+1} as a Taylor expansion around point x_i:

$$\phi(x_{i+1}) = \phi(x_i) + h\left(\frac{\partial\phi}{\partial x}\right)_i + \frac{h^2}{2}\left(\frac{\partial^2\phi}{\partial x^2}\right)_i + \frac{h^3}{6}\left(\frac{\partial^3\phi}{\partial x^3}\right)_i + O(h^4) \tag{3.1}$$

The same can be done for other neighboring points, for example:

$$\phi(x_{i-1}) = \phi(x_i) - h\left(\frac{\partial\phi}{\partial x}\right)_i + \frac{h^2}{2}\left(\frac{\partial^2\phi}{\partial x^2}\right)_i - \frac{h^3}{6}\left(\frac{\partial^3\phi}{\partial x^3}\right)_i + O(h^4) \tag{3.2}$$

Subtracting Eq. (3.2) from Eq. (3.1) one obtains:

$$\phi(x_{i+1}) - \phi(x_{i-1}) = 2h\left(\frac{\partial\phi}{\partial x}\right)_i + 2\frac{h^3}{6}\left(\frac{\partial^3\phi}{\partial x^3}\right)_i + O(h^5) \tag{3.3}$$

The first derivative at point x_i can then be expressed as:

$$\left(\frac{\partial\phi}{\partial x}\right)_i = \frac{\phi(x_{i+1}) - \phi(x_{i-1})}{2h} + O(h^2) \tag{3.4}$$

This is a *central* scheme, since it uses points on opposite sides to approximate the derivative. Proceeding in a similar way, several different possibilities arise and *forward* and *backward* differences can also be obtained. Scheme (3.4) is *second order accurate*: the truncation error is $TE \sim O(h^2)$. Using more neighboring points higher-order accurate schemes can be achieved. As stated above, the FD approach is used in the simulation of the Lisbon burner, characterized by a geometry which is simple enough to use a structured mesh, with the advantages previously mentioned. A Cartesian staggered grid is used, to avoid numerical pressure-velocity decoupling. Time derivatives are discretized with a second order accurate implicit backward

scheme. The diffusive terms are discretized with a fourth order central scheme, while for the convective terms a fifth-order WENO scheme is adopted. The high-order accuracy of the WENO scheme ensures low numerical dissipation. Moreover, it is suitable to capture the steep gradients at the flame front. The different schemes are briefly described in the following.

- **Second order time derivative scheme**
  The time derivative of a generic variable ϕ is dicretized in the following way: [110]
  $$\left(\frac{\partial \phi}{\partial t}\right)_j^{n+1} = \frac{3\phi_j^{n+1} - 4\phi_j^n + \phi_j^{n-1}}{2\Delta t} \tag{3.5}$$
  where Δt is the time step, the indices j and n refer to space and time, respectively. The scheme is implicit: the derivative at the new time $n+1$ is depends also on the value of variable ϕ at time $n+1$.

- **Fourth order central scheme**
  Being h the mesh size, this scheme has the following expression [109]:
  $$\left(\frac{\partial^2 \phi}{\partial x^2}\right)_j = \frac{-\phi_{j+2} + 16\phi_{j+1} - 30\phi_j + 16\phi_{j-1} - \phi_{j-2}}{12h^2} + O(h^4) \tag{3.6}$$

- **Fifth-order Weighted Essentially Non Oscillatory (WENO) scheme**
  The basic idea of the WENO [114] scheme is that instead of using one fixed stencil to approximate the derivatives, several candidate stencils are considered. In the following its implementation is briefly described. For simplicity a one-dimensional problem, the scalar conservation law, is considered:
  $$u_t + L(u) = u_t + f(u)_x = 0 \tag{3.7}$$
  To approximate the derivatives at x_j the spatial operator L uses the fluxes values f at half cell:
  $$L = \frac{1}{\Delta x}\left(\hat{f}_{j+1/2} - \hat{f}_{j-1/2}\right) \tag{3.8}$$
  where the hat indicates the discrete representation of the fluxes. The stencil in WENO schemes is not fixed but adaptive. Using a number r of candidate stencils, an order of accuracy of $2r-1$ is achieved. For a fifth-order accurate scheme then $r = 3$ and the three candidate stencils reported in Fig. 3.2 are considered to interpolate the fluxes. The interpolation schemes on the three stencils respectively have the following expressions [114]:
  $$\hat{f}_{j+1/2}^{(1)} = \frac{1}{3}f_{j-2} - \frac{7}{6}f_{j-1} + \frac{11}{6}f_j \tag{3.9}$$
  $$\hat{f}_{j+1/2}^{(2)} = -\frac{1}{6}f_{j-1} + \frac{5}{6}f_j + \frac{1}{3}f_{j+1} \tag{3.10}$$
  $$\hat{f}_{j+1/2}^{(3)} = \frac{1}{3}f_j + \frac{5}{6}f_{j+1} - \frac{1}{6}f_{j+2} \tag{3.11}$$

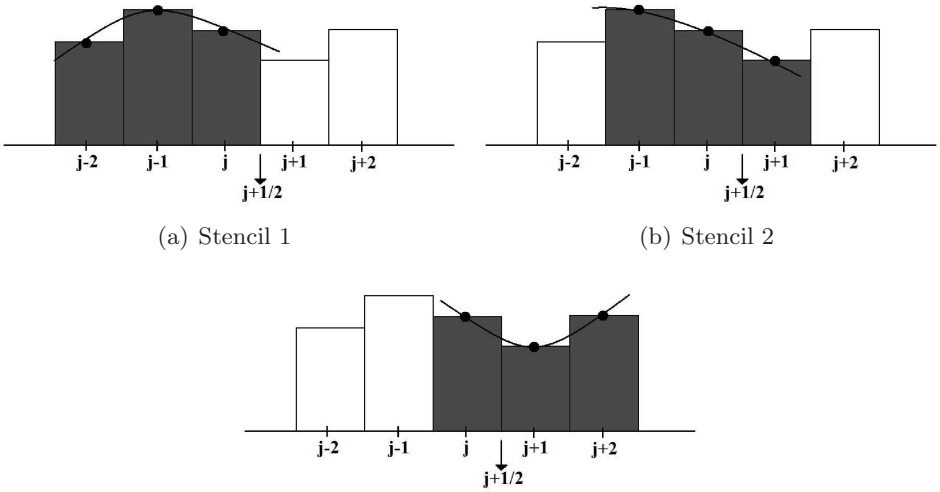

(a) Stencil 1

(b) Stencil 2

(c) Stencil 3

Figure 3.2: Canditate stencils for WENO schemes.

For each stencil a smoothness indicator IS_k is computed as follows [114]:

$$IS_1 = \frac{13}{12}\left(f_{j-2} - 2f_{j-1} + f_j\right)^2 + \frac{1}{4}\left(f_{j-2} - 4f_{j-1} + 3f_j\right)^2 \quad (3.12)$$

$$IS_2 = \frac{13}{12}\left(f_{j-1} - 2f_j + f_{j+1}\right)^2 + \frac{1}{4}\left(f_{j-1} - 4f_{j+1}\right)^2 \quad (3.13)$$

$$IS_3 = \frac{13}{12}\left(f_j - 2f_{j+1} + f_{j+2}\right)^2 + \frac{1}{4}\left(3f_j - 4f_{j+1} + f_{j+2}\right)^2 \quad (3.14)$$

The WENO schemes are actually an improvement of the formerly introduced Essentially Non Oscillatory (ENO) schemes [115]. The ENO schemes would choose the smoothest of the three stencil to interpolate the fluxes, ensuring an accuracy of order r. Choosing the best stencil these schemes are particularly suited to handle discontinuities. The WENO schemes [114] instead introduce a weight w_k for each stencil:

$$\hat{f}_{j+1/2} = w_1 \hat{f}^{(1)}_{j+1/2} + w_2 \hat{f}^{(2)}_{j+1/2} + w_3 \hat{f}^{(3)}_{j+1/2} \quad (3.15)$$

In this way they ensure an accuracy of order r (like ENO) close to discontinuities while in smooth regions of the flow the accuracy increases to $2r - 1$. The (non linear) weights are implemented as follows:

$$w_k = \frac{\alpha_k}{\alpha_1 + \alpha_2 + \alpha_3} \quad (3.16)$$

where the parameters α_k are defined as:

$$\alpha_k = \frac{\gamma_k}{\left(\varepsilon + IS_k\right)^2} \quad (3.17)$$

and γ_k are the linear weights

$$\gamma_1 = \frac{1}{10}; \quad \gamma_2 = \frac{6}{10}; \quad \gamma_3 = \frac{3}{10}; \tag{3.18}$$

ε is a very small number (typically $\varepsilon = 10^{-6}$) to avoid that the denominator ever becomes zero.

3.1.1.1 In-house solver details

A semi-incompressible formulation is used, implying that density is function of temperature only. Thus, the density is assumed to depend on the temperature but not on the pressure (low-Mach number approximation). With such an approximation, no pressure dependent term is found in the energy (or progress variable) equation. It is possible to solve the pressure and the velocity independently from the c-equation. This is not straightforward since the gradient of the pressure appears in the momentum equations but no explicit equation is found. The classical approach of solving a Poisson equation for the pressure is followed. Taking the divergence of the momentum equation, a Poisson equation for the pressure is derived, namely a scalar equation in which the Laplacian of the pressure $\nabla^2 p$ is explicitly expressed in terms of the velocity. In this way it is possible to solve the coupling between the pressure and the velocity with an iterative approach.
Gauss-Seidel iterations are used to smooth the approximations, and a multigrid method is used to get faster convergence. The multigrid method features several levels of grids (from fine to coarser grids). The idea is that the low frequencies components of the errors converge faster on the coarser grids, where the solution is computed at very little computational cost, while the high frequency components are converged on the finest grid. Smoothing the residuals from a fine to a coarser grid is called *restricting*, interpolating from a coarse to a finer grid level is called *prolonging* [109]. Several "paths" can be followed to obtain the final solution: depending on the sequences of restrictions and prolongations different *cycles* are possible. Typical multigrid paths are sketched in Fig. 3.3.

3.1.2 Finite Volume

In the Finite Volume method the conservation laws of mass, momentum and energy are formulated in a (small) control volume. The computational domain is the ensemble of such small control volumes. The computational nodes are placed in the centers of these volumes. An advantage of FV methods is that they are conservative (fluxes between contiguous volumes are identical). Moreover, they can handle unstructured meshes and therefore they are suitable for complex geometries. As mentioned above, the main drawback is the fact that it is less straight-forward to implement high order discretization schemes for the derivatives in unstructured meshes. In FV, the terms of the Navier-Stokes equation need to be integrated over a volume V before being discretized. Typically the derivatives of a generic variable

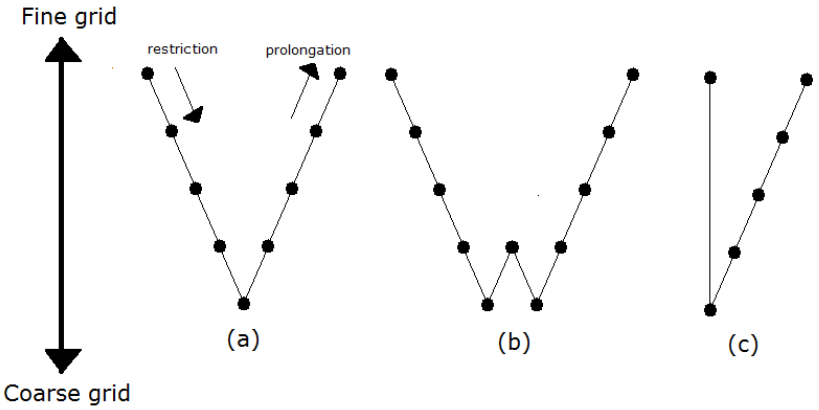

Figure 3.3: (a) V cycle; (b) W cycle; (c) Saw-tooth cycle.

ϕ are transformed into integrals over the surface S of the cells, through Gauss's theorem:

$$\int_V \nabla * \phi dV = \oint_S \phi * dS \tag{3.19}$$

where $*$ might represent any tensorial product operation. As an example, we report here the discretization of the convection term [116]

$$\int_V \nabla \cdot (\rho U \phi) dV = \oint_S dS \cdot (\rho U \phi) = \sum_f S_f \cdot (\rho U \phi)_f = \sum_f F_f \phi_f \tag{3.20}$$

where S_f is the vector normal to the faces of the cell, the subscript f indicates the value of a quantity in the center of the face, and $F_f = S_f \cdot (\rho U)_f$ is the mass flux through the face. Clearly, the value of the variable ϕ_f at the face is needed, and there are different ways to obtain the interpolated value. A possibility is to assume that the variable ϕ varies linearly between the two cells with centers P and N that share the face f, obtaining the following scheme [116]

$$\phi_f = f_x \phi_P + (1 - f_x)\phi_N \tag{3.21}$$

where $f_x = \overline{fN}/\overline{PN}$ is the ratio of the distances between the face and the cell center N and between the two faces (see Fig. 3.4). This "linear"(or central differencing scheme) is second order accurate but it can cause undesired oscillations. An "upwind"scheme,

$$\phi_f = \phi_P \; if \; F \geq 0; \; \phi_N \; if \; F < 0 \; , \tag{3.22}$$

instead, ensures boundedness of the variable at the price of loss of accuracy (it is only first order). A possibility to preserve both accuracy and boundedness is to use a "Gamma"scheme which is a combination of the two previous schemes through the blending factor γ:

$$\phi_f = (1 - \gamma)\phi_{f_{upw}} + \gamma \phi_{f_{lin}} \tag{3.23}$$

Clearly, $0 \leq \gamma \leq 1$, and the extreme values $\gamma = 0$ and $\gamma = 1$ retrieve the upwind and the linear schemes, respectively.

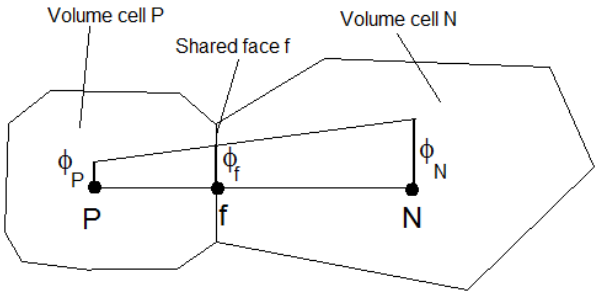

Figure 3.4: Sketch for the linear scheme.

3.1.2.1 Accuracy of the schemes in OpenFOAM

Besides the few ones presented above, several other possibilities exist and a large variety of discretization schemes is available in OpenFOAM. It is not the intention to report here the details of the schemes, instead we present the results of a brief test assessing their accuracy. The test was performed through the 1-D discretization of a known function g(x), namely $g(x) = x^3 e^{-ax^2}$, with the parameter $a = 50$. The convection term $f(x) = \int_V \nabla \cdot (\rho g g) dV$ was then computed with OpenFOAM on a discrete grid (taking $\rho = 1$) and compared, since the derivative is known, to its exact value reported in Fig. 3.5(a). All the schemes approximate well the curve, however Fig. 3.5(a) does not tell much about the accuracy of the discretization. Gradually halving the resolution of the mesh, a typical accuracy test can be performed. The results are given in Fig. 3.5(b). It is possible to see that the "upwind"and the "linear"are first and second order accurate, respectively, as expected. All the other schemes that have been tested did not report accuracy order higher than 2. In the simulations of the TARS burner reported in this thesis and in the included papers, unless differently specified, the "linear"scheme is used for the spatial derivative. A FV implementation of second order backward differencing is used for the time derivatives, see Eq. (3.5).

3.1.2.2 OpenFOAM details and scalability

Incompressible (isothermal case in Paper III) and Low-Mach number (reacting cases in Paper V and VI) solvers are used. The pressure-velocity coupling is treated with a PISO algorithm, together with a blend of conjugate gradient and multi-grid methods to speed up the coupling steps. The OpenFOAM tool box easily allows to run in parallel. In Fig. 3.6 the results from a speed-up test are reported. A typical test case of the TARS burner was used. The scalability was found to be very good with almost linear speed-up. Depending on the number of cells of the mesh, the optimal ratio of cells/processor was found to be $\simeq 150000$.

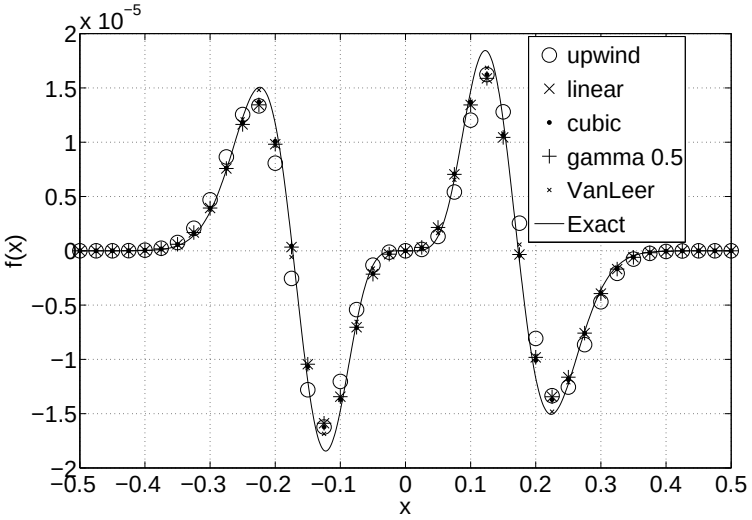

(a) Discretization of the convection term using different schemes

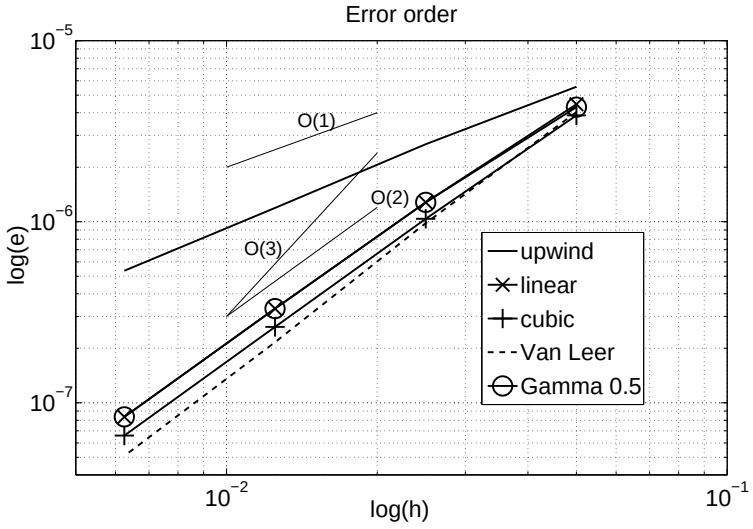

(b) Accuracy of the convection term using different schemes

Figure 3.5: Analysis of the schemes for the convection term.

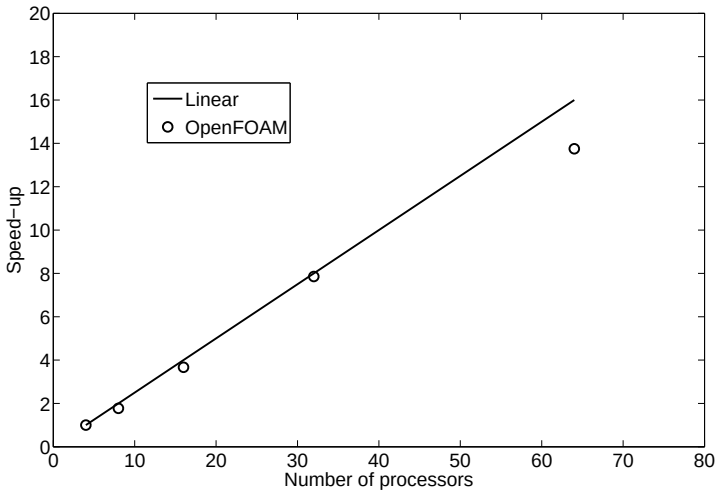

Figure 3.6: OpenFOAM speed-up test.

3.2 Experimental techniques

In the last decades the experimental techniques available for fluid dynamics investigations underwent enormous progresses. Thanks to the use of lasers, in particular optical diagnostics became available and useful tools to study both non-reacting and reacting flows. The non-intrusiveness of these techniques is especially appealing in the combustion field, where the use of probes is problematic while altering the flow and the flame. The development of optical diagnostics such as Particle Image Velocimetry (PIV) and Laser Induced Fluorescence (LIF) gave a better insight into the flow and flames structures. PIV measures the velocity field, LIF visualizes and quantifies the concentration of certain molecular species, thereby (in the case of e.g. OH) the distribution of the flame can be determined. Nowadays complex set-ups can be built and these techniques can be combined giving multiple simultaneous information about the flow/flame [25, 117, 118]. In this section the basic working principle of PIV and PLIF is described.

3.2.1 Particle Image Velocimetry

Particle Image Velocimetry is an experimental fluid dynamics technique to measure the velocity field (two or three components) in a flow. It has a double advantage: it is not intrusive (like for example Hot Wire Anemometry) and it allows to get information on the velocity field on a 2D plane instead of in a single point (unlike Laser Doppler Velocimetry or Hot Wire Anemometry). The principle is to compute the velocity from the displacement of small tracking particles that can follow the flow accurately. These particles scatter the light of a laser sheet. A Charge Coupled Device (CCD) camera records the scattered light in two subsequent images shifted by a known time interval Δt. To track the particles' displacements, the images are

subdivided in interrogation areas and a spatial 2D cross-correlation between the intensities F_i and F_j in corresponding interrogation areas is performed.

$$R_{i,j}(r_1, r_2) = \int\int F_i(x, y) F_j(x + r_1, y + r_2)\, dxdy \tag{3.24}$$

The displacement vector $\vec{\Delta r} = [r_{1peak}, r_{2peak}]$ corresponds to the location of the peak of the cross-correlation, i.e. the average displacement within the interrogation area. The velocity is just $\vec{\Delta r}/\Delta t$. This procedure is repeated for each interrogation area and therefore the full velocity vector map is obtained. Fig. 3.7 helps in understanding the technique. A major source of difficulty is related to the particles.

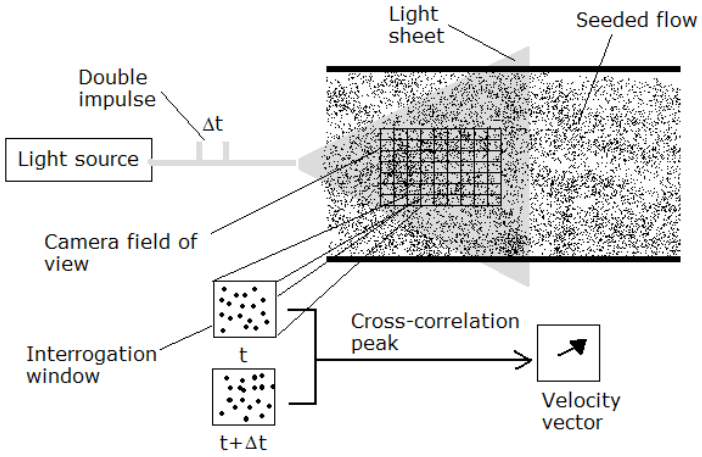

Figure 3.7: PIV technique working principle.

Good seeding may be difficult and the particles have to follow the flow with high fidelity. The particles must be as small and as light as possible with respect to the density of the fluids so that their effect on the flow itself is negligible (Stokes number much smaller than 1). Too small particles pose also a problem, since these must be captured clearly by the CCD camera. For gas turbine applications, usually seeding particle size is of the order of microns. An additional requirements is that the particles should not combust.

3.2.2 Laser Induced Fluorescence

The Laser Induced Fluorescence is an optical diagnostic technique which allows to visualize molecular species in a flow (in particular combustion products in a reacting flow). Nowadays LIF is mainly used to give 2D information showing the distribution of the desired species in a plane (Planar Laser Induced Fluorescence, PLIF). For LIF no seeding is needed since a laser is used to excite the fluorescence of the species of interest. The molecules of the species absorb photons from the laser and re-emit photons with a longer wavelenght [119]. These photons are recorded through a band-pass filter in front of a digital camera. A sketch of the LIF system is

given in Fig. 3.8. The technique is completely non-intrusive, although it should be mentioned that in cold applications if no appropriate species are available naturally, one has to add such a tracer. In this work OH-PLIF results will be shown. Although

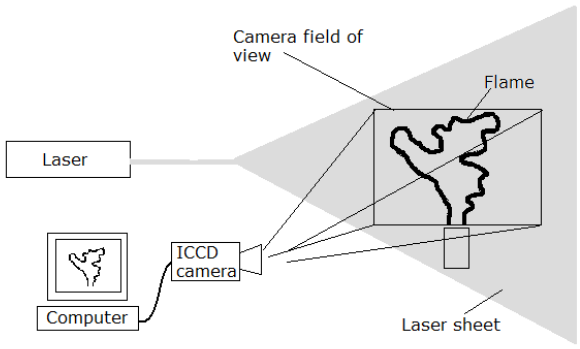

Figure 3.8: Schematics of PLIF set-up.

the OH radical is more a postflame zone species (Fig. 2.4), OH-LIF is widely used and is a well established diagnostic technique in combustion applications to detect and visualize the flame position.

3.2.3 Chemiluminescence

Using only an Intensified CCD camera together with the filter at the selected wavelength (for OH around 310 nm), photons emission of desired species can be detected. The species are excited by the heat and emit a photon to return to the ground state. With respect to LIF, the chemiluminescence signal is weaker. Moreover, the source of the luminescence is spread throughout the domain (in contrast to a plane in LIF), whereby the strength of the luminescence is the integrated value over the line of sight of the camera. On the other hand this technique is simple to perform, since it only needs optical access in one direction, and is relatively cheap with respect to laser diagnostics.

3.3 Proper Orthogonal Decomposition

3.3.1 POD

The Proper Orthogonal Decomposition (POD) is a post-processing tool to obtain a modal decomposition of a given ensemble of data. After performing experiments or numerical simulations one obtains a certain number of realizations of the flow (instantaneous samples) $u(x,t)$. For simplicity, we assume here that the quantity $u(x,t)$ represents a scalar field. After applying the POD procedure an instantaneous realization at time t_k $u(x,t_k)$ can be reconstructed in terms of a basis of

eigenfunctions $\phi_j(x)$, which represent typical *modes* of the ensemble:

$$u(x,t_k) = a_0\phi_0(x) + \sum_{j=1}^{\infty} a_j(t_k)\phi_j(x) \tag{3.25}$$

In Eq. (3.25) $\phi_0(x)$, or mode 0, represents the time averaged field while subsequent modes capture the fluctuations and therefore the dynamics. The coefficients $a_j(t_k)$ are referred to as *time coefficients*. POD can be seen as analogous to the Fourier modal analysis. Whereas in the Fourier decomposition the modes are a-priori chosen to be sinusoidal, in POD the basis is empirical, in the sense that it depends on the data. The basis is in fact sought so to maximize the quantity [43, 44]:

$$\frac{\langle |(u,\phi)|^2 \rangle}{\|\phi\|^2} \tag{3.26}$$

In Eq. (3.26) $\langle\cdot\rangle$ denotes the time or ensemble average, (a,b) represents an inner product and $||c||$ a norm:

$$(a,b) = \int_{\Omega_x} a \cdot b^* \, dx \qquad ||c|| = (c,c) \tag{3.27}$$

where Ω_x is the domain of interest in which $u(x)$ and $\phi(x)$ are defined. The asterisk (*) represents complex conjugation. Maximization of the quantity in Eq. (3.26) reduces to an eigenvalue problem [43, 44]:

$$\int_{\Omega_x} \langle u(x,t)u(x',t)\rangle \, \phi(x') \, dx' = \lambda \, \phi(x) \tag{3.28}$$

It is not the purpose of this section to treat in details the theory, for the derivations and the implementation of POD the reader is referred to [43,44,47,62]. However, in practical applications, the domain Ω_x is discretized in a certain number of discrete points M and the eigenvalue problem has a size MxM. To solve the eigenvalue problem is computationally expensive. Applying Sirovich's *Method of snapshots* [120] Eq. 3.28 is recast into a lighter eigenvalue problem of size NxN, where N is the number of instantaneous samples, or snapshots (typically, $M \gg N$). The eigenvalue problem reads:

$$\begin{Bmatrix} b_{11} & \cdots & b_{1N} \\ \vdots & \ddots & \vdots \\ b_{1N} & \cdots & b_{NN} \end{Bmatrix} \begin{Bmatrix} c_1 \\ \vdots \\ c_N \end{Bmatrix} = \lambda \begin{Bmatrix} c_1 \\ \vdots \\ c_N \end{Bmatrix} \tag{3.29}$$

where

$$b_{rt} = \int_{\Omega_x} u(x,t_r)u(x,t_p) \, dx \tag{3.30}$$

It is important to remark that as a result of the eigenvalue problem, one obtains N eigenvalues λ_j. To each eigenvalue λ_j corresponds a mode $\phi_j(x)$ and N eigenvectors

$c_j(t_k)$. In the method of snapshots the modes are expressed as a linear combination of the instantaneous realizations:

$$\phi_j(x) = \frac{1}{\lambda_j N} \sum_{k=1}^{N} c_j(t_k) u(x, t_k) \tag{3.31}$$

The eigenvalues are ordered in descending order $\lambda_j > \lambda_{j+1}$ and represent the *energetic content* of the modes. Thus, if the variable u to which the decomposition is applied represents the velocity, the first POD modes have the highest turbulent kinetic energy content and typically identify coherent structures. The time coefficients in Eq. (3.25) are computed projecting the modes on the snapshots. The time coefficient relative to the j-th mode and the k-th instantaneous sample reads:

$$a_j(t_k) = \phi_j(x) \cdot u(x, t_k) \tag{3.32}$$

3.3.2 Extended POD

The main idea behind Extended-POD (EPOD) is to see how events are correlated in space or time. One considers a second realization $\alpha(x,t)$ which is obtained simultaneously to $u(x,t)$. For example, $\alpha(x,t)$ might represent another variable like pressure, temperature, species concentration, progress variable, or even the same variable u on a different domain. The idea is then to project the second data set on the eigenvectors of the original POD analysis. In this way the procedure "distillates" the part of the signal of the variable α which is correlated to the POD modes of the original variable of analysis u. The extended modes $\psi_j(x)$ are defined as [58, 59, 62]:

$$\psi_j(x) = \frac{1}{\lambda_j N} \sum_{k=1}^{N} c_j(t_k) \alpha(x, t_k) \tag{3.33}$$

In other words statistical quantities conditioned to the dominant fluctuations of u are generated. Conditioned variables have been a key tool for understanding fluctuations in flames. EPOD extends the idea by linking any unsteady variable (OH concentration, progress variable) with statistical quantities describing the large scale fluctuations of the field u (velocity in this case).

In the papers presented in this thesis, EPOD is applied to realizations in which the variable α is representative of the flame (progress variable for the numerical simulations, Paper I [61], OH-signal for experimental data, Paper II, [62]). In this way it is possible to highlight the correlations between flow and flame dynamics. This procedure is therefore very helpful to investigate combustion dynamics. For more details on theory and implementation, the reader is referred to [58, 59, 62].

3.3.3 Time coefficients information and interlink with phase averaging

A "very special property" [121] of the Proper Orthogonal Decomposition is the spatio-temporal relation between the modes and the instantaneous samples through

the time coefficients. Through Eq. (3.32) the time coefficients summarize the temporal variations of the different modes. It is then possible to obtain the frequency spectrum of a mode performing a simple Fourier analysis of the corresponding sequence of time coefficients. This is of course only possible if the mode is harmonic and if the temporal resolution is sufficient, for example in the case of LES data or time resolved PIV/PLIF.

However, the information contained in the time coefficients is very useful also when the time resolution of the instantaneous samples is too slow as compared to the frequencies of the modes (for example this is typically the case of experimental data acquired with standard PIV or PLIF systems). The time coefficients in fact should be seen as "labels"or "weights"which are assigned to the instantaneous samples. Thus, the time coefficient $a_j(t_k)$ tells "how much"of mode j is contained in the instantaneous sample at time t_k. They allow discriminating within the ensemble and relate to conditional averaging and in particular to phase averaging [56, 57, 65]. As a matter of fact it is often the case that two modes are complementary, i.e. they are a pair of modes representing the same periodical dynamics. Independently of the frequency of acquisition, if the number of samples is statistically significant, a scatter plot of the time coefficients of the two modes would fill up a circumference like in Fig. 3.9 (details in the results section) [31, 56, 57, 65, 122, 123].

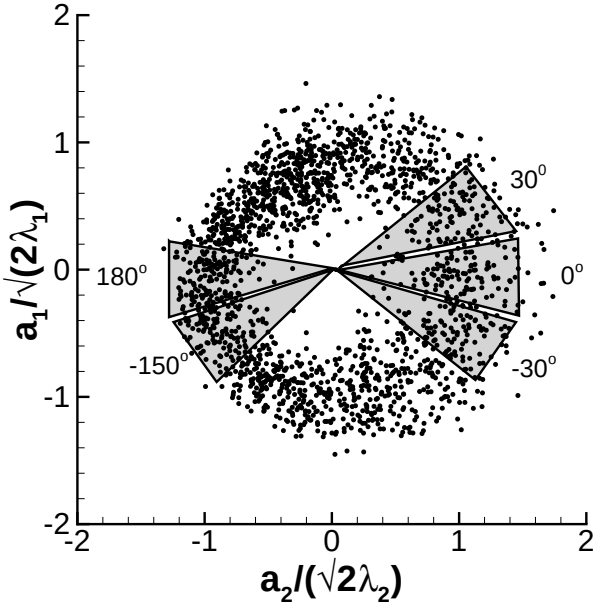

Figure 3.9: Scatter plot of time coefficients from the POD analysis, $a_1(t)$ vs. $a_2(t)$.

Each point in Fig. 3.9 represents an instantaneous snapshots whose phase angle can be expressed as:

$$\theta(t_k) = arctan\left(\frac{a_1(t_k)\sqrt{\lambda_2}}{a_2(t_k)\sqrt{\lambda_1}}\right) \tag{3.34}$$

Thus, one can subdivide the circumference into a desired number of arcs, each

sector corresponding to a given phase-angle. With this information, it is possible to perform an a-posteriori phase average of the original instantaneous snapshots ensemble. No additional information (phase-locking, simultaneous pressure signal) is needed beside the ensemble of independent and randomly acquired samples.

Chapter 4

Problem Set-up

In this thesis, two academic research burners are studied: the *Lisbon* and the *TARS* combustors. In this chapter, their geometrical features will be detailed. For the cases investigated, the operating conditions, the experimental and numerical set-ups will be given. Brief overview of previous studies will also be presented. The Lisbon burner, given its simplicity, is believed to be a good test-case to investigate the dynamics of swirling flames and in particular the response of vortex breakdown/flame stabilization to axial oscillations. The TARS fuel-injector combines laboratory flexibility and complex geometry, similar to a real aero-engine design. In this work it is investigated both numerically and experimentally. The analysis is challenging given the multi-scale physics and the complexity of the flow and the flame.

4.1 Lisbon burner

A sketch of the Lisbon combustor [23] is shown in Fig. 4.1. Following the flow from left to the right, the combustor is composed by:

- **Swirl generator:** It features adjustable blade angles to set the desired swirl number.
- **Converging annulus:** Connecting the swirler to the premixing tube.
- **Premixing tube:** A premixing pipe of 0.05 m diameter ensures a mixture with the fuel which is injected at the exit of a bluff body downstream the swirl generator.
- **Throat** The premixing tube is connected to the combustion chamber through a converging diverging nozzle with minimum diameter equal D=0.04 m.
- **Combustion chamber** The combustion chamber is axysymmetric and has a diameter of 0.11m. It is 0.336 m long.

This model combustor was experimentally studied at Lisbon Technical University mainly using LDV, flow visualization techniques, pressure probes, and gas temperature sampling [20, 23, 42, 60]. Both reacting and non-reacting flows revealed the existence of helical structures and PVC for high enough swirl numbers. This combustor has also been numerically computed by means of LES [24]. The simulations successfully reproduced the experimental data and with the help of Proper Orthogonal Decomposition highlighted the structures found in the experiments. The PVC

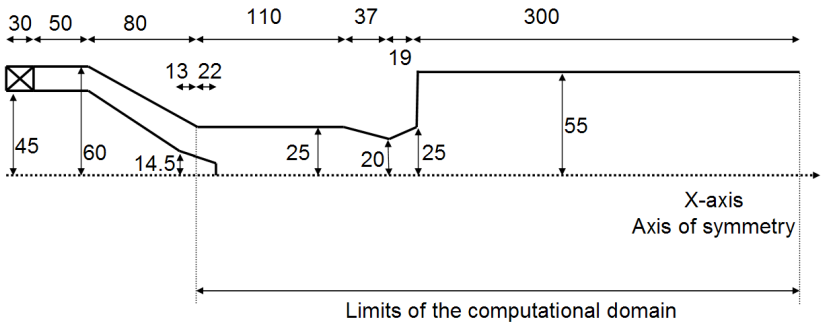

Figure 4.1: Schematics of the Lisbon burner. Lengths in [mm] [23, 24].

was characterized by a frequency $f = 880Hz$ corresponding to a Strouhal number $St = \frac{fD}{U_0} \simeq 0.6$. The combustor has been further simulated in this thesis. The operating conditions are given in Table 4.1. The effect of axial oscillations on the flame dynamics and their interaction with the vortex breakdown has been investigated (Paper I, [61]).

Equivalence ratio (propane-air)	0.5
Inlet gas temperature	573 K
Bulk velocity in the nozzle U_0	59 m/s
Reynolds number	81000
Swirl number	1.05

Table 4.1: Operating conditions for the Lisbon combustor.

4.1.1 Computational domain and boundary conditions

The computational domain covers a fraction of the experimental rig, as sketched in Fig. 4.1, and includes the premixing tube, the contraction and the combustion chamber. The swirler is not included in the domain. The flow enters the premixing tube through an annulus surrounding a conical bluff body. The premixing tube, including the annulus and the converging diverging nozzle, is 4.14D long. The diameter of the premixing tube is 1.25D and reduces to 1D at the contraction. The conical bluff body is $\simeq 0.6D$ long. The cylindrical combustion chamber has a diameter of 2.75D and a length of 8.4D. The reference frame is chosen such that X=x/D is aligned along the symmetry axis and its origin is in the sudden expansion plane ($X > 0$ is the combustion chamber, $X < 0$ is the premixing tube). In Fig. 4.1 Y=y/D corresponds to the axis perpendicular to the view while Z=z/D is perpendicular to the X-axis. The Navier-Stokes equations are discretized with a finite differences approach on a 3D Cartesian staggered grid. The mesh is composed of 1.9 millions computational cells, and it is refined in the premixing tube and in the flame zone, where the size of a cell is $h \simeq D/46$, while it is coarser near the outlet. The time step is $\Delta t = 3.2 \cdot 10^{-6} s$, corresponding to a Courant number of

$\simeq 0.2$.

Boundary conditions are applied as follows. At the inlet, the velocity vector is imposed [24] so to give the desired swirl number. No artificially generated turbulence is imposed at the inlet. The premixing pipe is assumed to be long enough for turbulence to develop before reaching the flame. A sensitivity analysis of the effect of (steady) boundary conditions ensured the validity of this hypothesis [24]. To emulate the effect of axial oscillations, a periodic mass flow is imposed:

$$\dot{m}(t) = \dot{m}_0 \left[1 + A sin\left(2\pi f t\right)\right] \tag{4.1}$$

where $\dot{m}_0$ is the average mass flow, t is the time, A and f are respectively the amplitude and frequency of the excitation. The frequencies of excitations are chosen among harmonics and sub-harmonics of the PVC found in previous studies [23, 24]. At the outlet, zero gradient boundary conditions are applied for all the variables:

$$\nabla\phi \cdot \vec{n} = 0 \tag{4.2}$$

where $\vec{n}$ is the normal to the outlet. If needed, the velocity at the outlet is corrected in order to ensure global mass conservation. The walls are assumed to be adiabatic (zero gradient for the progress variable) and no-slip is applied for the velocity:

$$\vec{v} = 0 \tag{4.3}$$

No boundary conditions are needed for the pressure because of the staggered grid. Initial conditions are also needed to have a well-posed problem. When starting computations from the scratch, all the variables are set to zero, with the exception of the progress variable. The c field is set to zero in the swirler, the premixing tube and the expansion region. The combustion chamber is filled with burnt gases (c is set equal to unity) to ensure ignition of the incoming mixture. When restarting previous computations, the fields at the last time step are used as initial conditions.

4.2 TARS

4.2.1 TARS burner

The TARS is a research fuel-injector with design features mimicking an actual aero-engine one. It was developed by Delavan Gas Turbine Products, a division of Goodrich Corporation, in collaboration with General Electric Aircraft Engines. The TARS is composed by three swirlers: outer, intermediate, and inner swirler with three corresponding air passages. In Fig. 4.2 the individual swirlers are visualized (not at the same scale) together with a 3D view of the assembled burner (Fig. 4.2(d)). The inner (Fig. 4.2(c)) and intermediate (Fig. 4.2(b)) vanes are axial swirlers, the outer one (Fig. 4.2(a)) is radial. The planar cuts shown in Fig. 4.2(e) help to better visualize the geometry. Each swirler can be easily interchanged with a similar one having different vane angles and/or rotating direction (clockwise, counter-clockwise). Different configurations of the TARS can be realized

corresponding to different swirling flow fields. It is designed following the concept of Lean Direct Injection (LDI), which is often used in aero-engines for pollution control [5]. Multiple points fuel injections, together with three concentric air passages with narrow vanes, enhance liquid fuel atomization and provide rapid mixing, so that no stoichiometric regions are present in the flame (with beneficial consequences on the maximum temperature and consequently emissions). However, the burner can be operated both in premixed and non-premixed mode, both with liquid and gaseous fuels. The diameter of the outlet nozzle is 50.8 mm, and used as a reference for non-dimensional coordinates. In the past, the TARS has been mostly studied

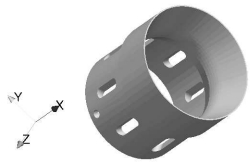

(a) Outer radial swirler.

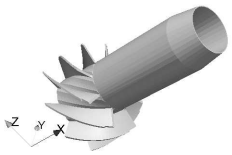

(b) Intermediate axial swirler.

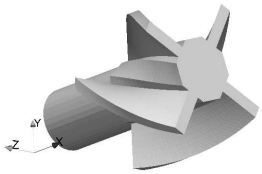

(c) Inner axial swirler.

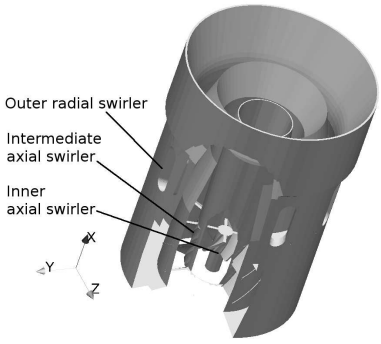

(d) 3D view of the assembled TARS.

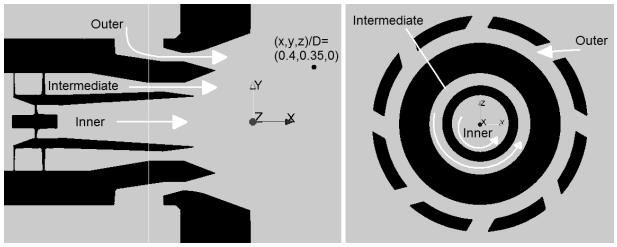

(e) Planar cuts of the TARS geometry (z/D=0, x/D=-0.6).

Figure 4.2: TARS geometry details.

experimentally [63,124–126]. A large database of experimental studies can be found in the literature, concerning non-reacting and reacting cases, open-air and confined configurations. Several issues have been addressed, we cite here a few examples: the significance and impact of inlet and outlet boundary conditions on non-reacting and reacting flows and emissions in the latter case [63], appearance and location of vortex breakdown for non-reacting cases [124], mutual relation of vortex breakdown bubble and flame stabilization point [125], combustion dynamics [65,126]. However, insights on the flow inside the swirler (not accessible to experiments) can only be given by a CFD analysis. Only two works [87, 127] applied LES to simulate the TARS, but without focusing on the flow through the swirlers, or resolving it at all. Grinstein et al [87] performed LES only of the flow downstream the TARS, using

available velocity measurements close to the nozzle outlet as inlet conditions. In the same work, the flow inside the TARS was instead simulated by RANS, and only on a 90 degree pie sector. Fureby et al [127] extended the LES domain including also the TARS in the computational mesh. However the inlet boundary conditions upstream the three swirlers had to be presumed. As a matter of fact LES (and numerical simulations in general) are strongly dependent on the applied (mainly inlet) boundary conditions, and as pointed out in that work, a further improvement would be to include the plenum before the TARS in the computational domain. This has been done in this work. Moving the inlet further upstream, one can let the mass flow to split through the swirler vanes according to the geometry of the TARS itself, leading to a more realistic simulation, affected by less assumptions, getting a more reliable view of the dynamics. Furthermore, as it will be clarified in the following, we even include in the computational domain the items upstream the TARS, namely the support arms and the fuel supply pipes, see Fig 4.4.

4.2.2 Burner support facility and diagnostic systems

An atmospheric combustion test rig (Fig. 4.3) is used to investigate the TARS. The rig consists of an inlet flange, a flow conditioning chamber (609.6 mm long, 133.4 mm inner diameter) and a plenum chamber (361.9 mm long, 133.4 mm inner diameter). The rig is vertical and the burner is centered on a mounting plate (6.35 mm, thick). In the plenum, the TARS is supported by two arms parallel to the flow. Upstream the TARS some bent pipes for fuel feeding are also present (Fig. 4.4). More detailed information on the TARS burner and the rig can be found in [63]. Several measurement techniques were used. Longitudinal cross-sections have been investigated by means of PIV and PLIF (Fig. 4.3(c)). OH* chemiluminescence line of sight measurements have been performed for a confined case (Fig. 4.3(b)). For this confined case the combustion chamber consisted of a quartz cylinder (0.4 m long, 0.11 m inner diameter).

4.2.3 Computational Domain and boundary conditions

The mesh that will be described here refers to the isothermal case study of Paper III [64], for which we report some results in Section 5.2. Slightly different meshes are used in the papers dealing with reacting cases, Papers V-VI, to which the reader is referred to for details. The computational domain (Fig. 4.4) contains a part of the plenum upstream the TARS, the TARS itself, and the mounting plate. The inlet is about $5.5D$ upstream the mounting plate. The open-air domain is about $10D$ long. A frustum boundary connects the edges of the mounting plate to the outlet of the domain. The coordinates origin is placed at the center of the TARS nozzle outlet, so that x/D=0 corresponds to the mounting plate (Fig. 4.4). The mesh is almost uniform since most of the cells are cuboids and slightly elongated in the direction of the flow (cell side ratios 1.12:1:1). Unstructured body-fitted polyhedral cells are used only close to the walls. Layers of refined cells are added in the proximity of

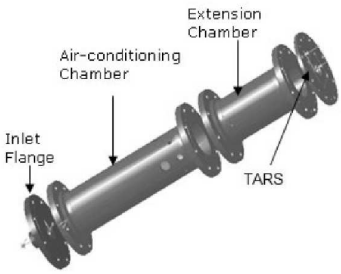

(a) Schematics of the TARS support.

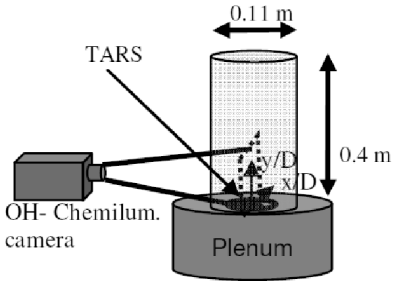

(b) Confined set-up.

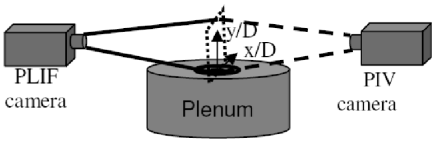

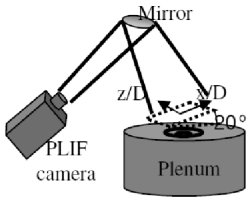

(c) Unconfined set-up.

Figure 4.3: TARS rig setups.

the walls, so that $y_+ \sim 1-2$ at the cell layer closest to the walls in the air passages. The mesh is refined inside the swirlers and downstream the TARS it is progressively coarsened towards the outlet and the external boundary. The mesh is composed of 11.1 millions cells. At the finest level the smallest dimension of a cuboid cell is about D/162. The diameters at the throats of the intermediate and outer passages are resolved with 14 cells. The narrowest duct in the inner air passage is behind the swirler blades, and is resolved with 12 cells. At the outlet of the inner air passage, 46 cells are placed along the diameter. The resolution in the premixing pipe, upstream the fuel-injector, is equal to $D_{pl}/110$, D_{pl} being the diameter of the plenum. Around the fuel supply pipes, the resolution is $D_{fp}/6$ where D_{fp} is the diameter of the fuel pipes, the thinnest bodies upstream the TARS. Boundary conditions are imposed as follows. For the velocity, at the inlet a constant top-hat axial velocity profile is imposed so to fulfil the measured mass flow rate. At the outlet zero gradient is imposed. The plenum chamber, the bodies upstream the TARS, the swirler vanes and the two sides of the mounting plate are considered walls, and no-slip condition is applied. In the frustum boundary, a very low constant axial velocity (ca. one fortieth of the inlet) is imposed giving a co-flow allowing entrainment. The pressure is fixed at the outlet (reference pressure = 0) and zero gradient boundary conditions are applied everywhere else.

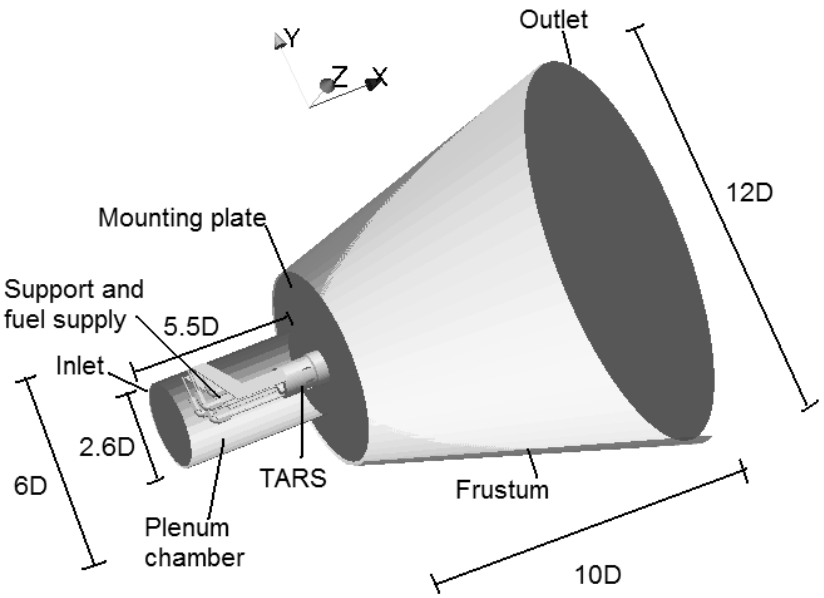

Figure 4.4: 3-D view of the computational domain (Case Isothermal).

4.2.4 Summary of operating conditions

This burner is investigated throughout papers III-VI. A wide range of cases with different operating conditions were studied. Table 4.2 gives the cases for which results are presented in Section 5.2. For further details the reader is referred to the papers included at the end of the thesis. The case "Isothermal" refers to the LES study of an unconfined (Fig. 4.3(c)) cold case which clarifies and details the complex flow inside and outside the TARS (Paper III [64]). The case denoted "Confined" refers to the confined (Fig. 4.3(b)) flame studied in Paper IV [65]. OH* chemiluminescence and POD are used to investigate the dynamics of the thermo-acoustics oscillations, proposing a method for the analysis of instabilities in industrial rigs.

Case	$\dot{m}_a$ (g/s)	$\dot{m}_f$ (g/s)	ϕ	Re	Paper	Note
Isothermal	13.8	-	-	18900	III	LES details of the flow
Confined	5.4	0.34	1.19	7849	IV	Thermo-acoustic instability

Table 4.2: Operating conditions for the TARS burner. $\dot{m}_a$ and $\dot{m}_f$ represent air and fuel flow rate, respectively. Inlet gas temperature 293 K, Pressure 1 atm.

Chapter 5

Summary of results

In this chapter relevant exemplifying results are briefly summarized. For a more detailed analysis and the complete set of problems and cases the reader is further referred to the papers enclosed at the end of this thesis.

5.1 Lisbon burner

The works of [23, 24] describe for this combustor the existence of a pair of counter-rotating helical structures leading to a precessing vortex core. Such structures have a characteristic frequency of 880 Hz, corresponding to a Strouhal number $St = 0.6$. This section summarizes the effect of axial forcing at half the frequency of the PVC ($St = 0.3$). The excitation is performed by means of sinusoidal fluctuations of the inlet mass flow, see Eq. (4.1). The amplitude of the excitation is set to 20% of the average mass flow.

5.1.1 Statistics

In Fig. 5.1 the average effect of the axial forcing is shown. The top frame shows the unforced case while in the bottom frame the time averaged field for the forced case is shown. The isolines describe the progress variable c (thus the flame). The flow features the typical IRZ caused by vortex breakdown and the toroidal ORZ between the walls and the expansion. The flame is located at the shear layers between the recirculation zones but is decoupled from the recirculating bubble, because of the PVC. As a global effect of the excitation, the flame is stabilized further upstream in the forced case, and the IRZ is also pulled upstream on average. Averaged quantitative profiles are shown in Fig. 5.2 quantifying a shifting in axial stabilization point of $\Delta X \sim 0.25$.

5.1.2 POD analysis

When averaging with traditional statistics, all the information about the dynamics is smoothed out. Therefore, POD is applied to characterize the most energetic modes of the flow. The results of the POD analysis in a longitudinal section are given in Fig. 5.3. Modes 1-4 for the forced case are shown. For each mode, the power spectrum of the time coefficients sequence gives a characteristic frequency of the mode itself. Modes 1 and 2 are a pair: they represent the same dynamics, namely axial fluctuations in the premixing tube. They correspond to the imposed forcing as confirmed by the peak at the same frequency as the excitation (St=0.3). Modes

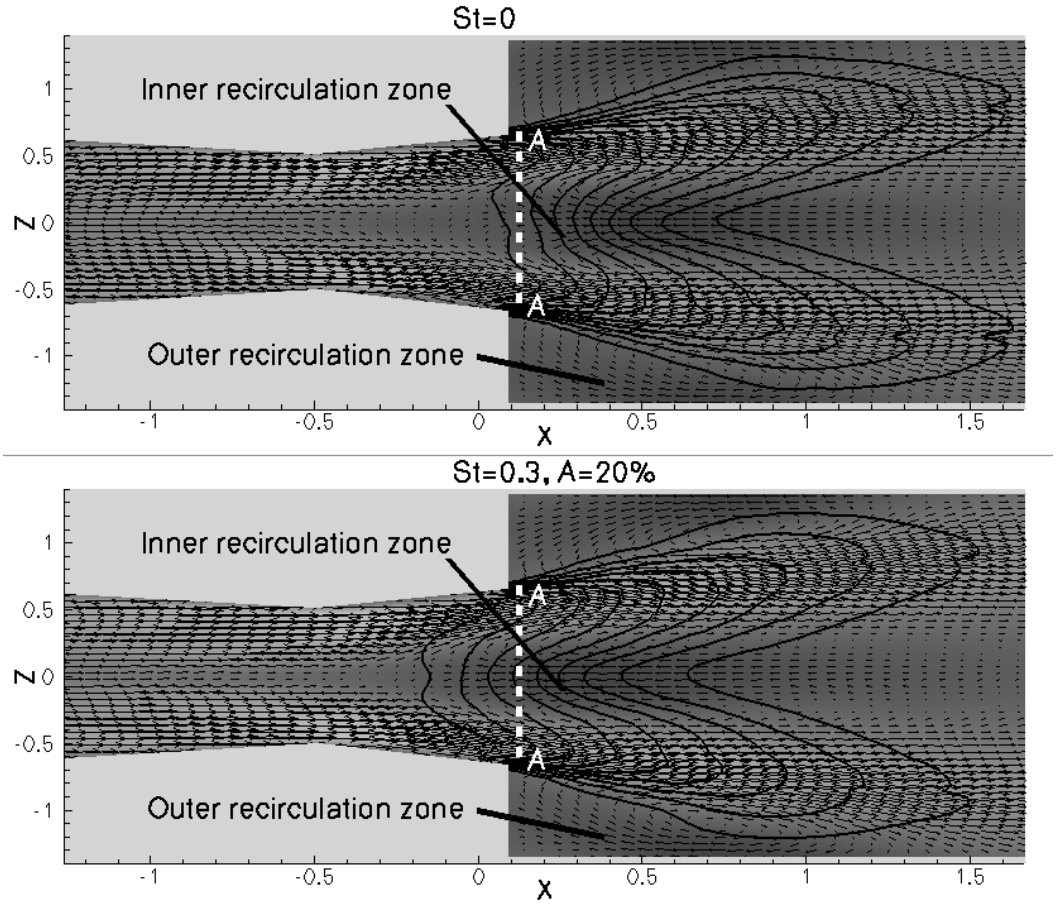

Figure 5.1: Average field. Axial velocity contour plot and vector map. Equally spaced progress variable isolines (from 0.05 to 0.95). Unforced (top) and forced (St=0.3, A=20%, bottom) cases.

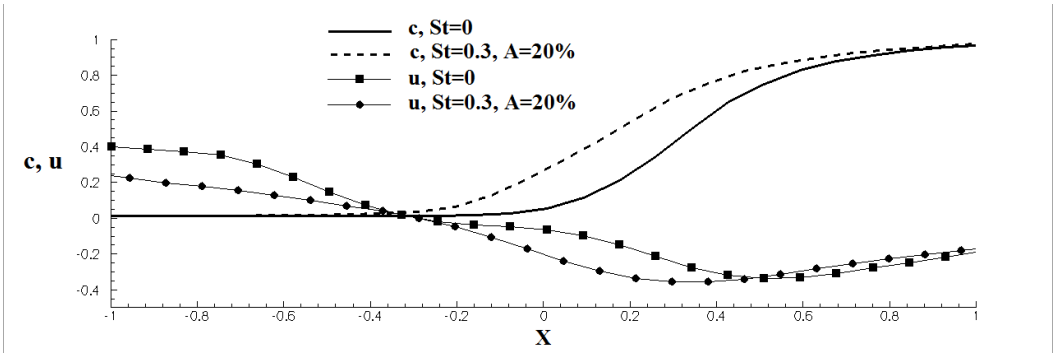

Figure 5.2: Progress variable c and normalized axial velocity u/U_0 profile along the symmetry axis (Z=0).

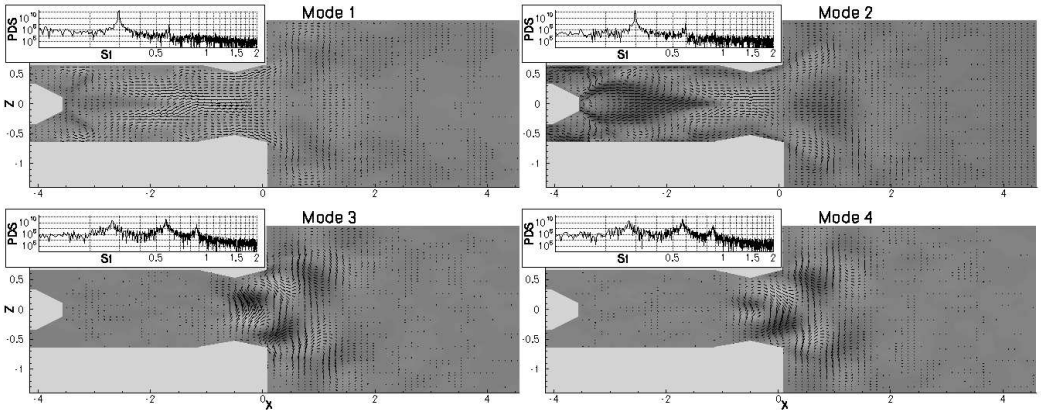

Figure 5.3: POD modes 1-4 in the axial cross-section and corresponding power density spectra of the time coefficients. Vector map and axial velocity contour plot. Forced case, (St=0.3, A=20%).

3-4 also compose a pair. They represent the helical structures leading to the PVC and keep a frequency peak at St=0.6 (although harmonics and sub-harmonics are noticed). In Fig. 5.4, the PVC is highlighted by the POD analysis in a cross section perpendicular to the axis, located just after the expansion. Modes 1 and 2 have two counter rotating helices which characterize the precession of the recirculation zone. Basically they are the section in this plane of the same helical structures visualized above and in fact have the same frequency peak at St=0.6. In the instantaneous snapshot shown in Fig. 5.5, a 3-D visualization of these two counter-rotating helical structures is depicted. The flame is affected by these dynamics and it follows the vortex core in its precession. These structures are of particular interest because they might be source of thermo-acoustic instabilities. Nonetheless, in this flame the PVC has also a beneficial effect. By keeping the flame instantaneously off-axis, it decouples the flame from the central recirculation zone and prevents flashback.

5.1.3 EPOD analysis

In order to assess the effect of the excitation on the flame in the forced case, the analysis is completed with Extended POD. Extended modes are computed for the progress variable through Eq. (3.33), taking the velocity as a reference variable. By doing so, the progress variable field which is correlated to the velocity modes is "distillated". In Fig. 5.6 time sequences of reconstructed snapshots (by means of Eq. (3.25)) are shown in the longitudinal plane. Mode 0 is complemented by modes 1-2 which we recall to represent axial fluctuations. The extended modes 1-2 of the progress variable are also shown as isolines. Scatter plots of the time coefficients ($a_1(t)$vs $a_2(t)$) are also shown, featuring a perfectly circumferential shape since the modes are pairs. The square represents the couple of values of the time coefficients for the considered reconstructed snapshot, thus denoting the phase angle. The data shown here are analogous to phase-averaged quantities that one would obtain

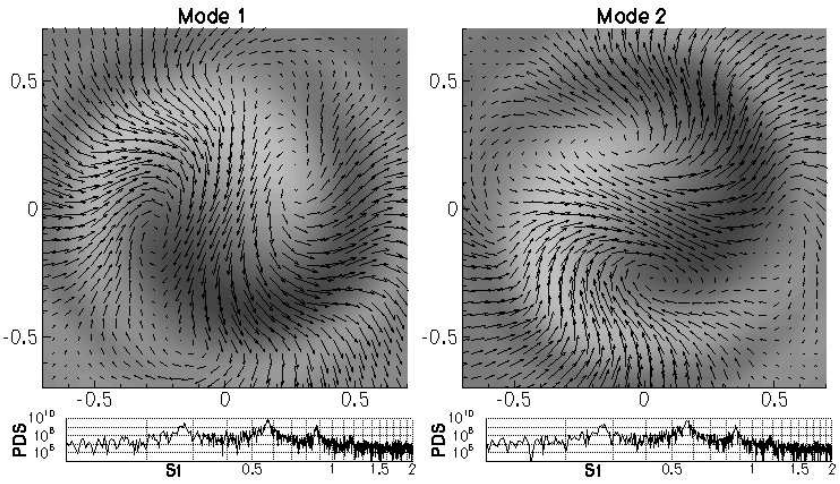

Figure 5.4: POD modes 1-2 in the perpendicular cross-section and corresponding power density spectra of the time coefficients. Vector map and axial velocity contour plot. Forced case (St=0.3, A=20%).

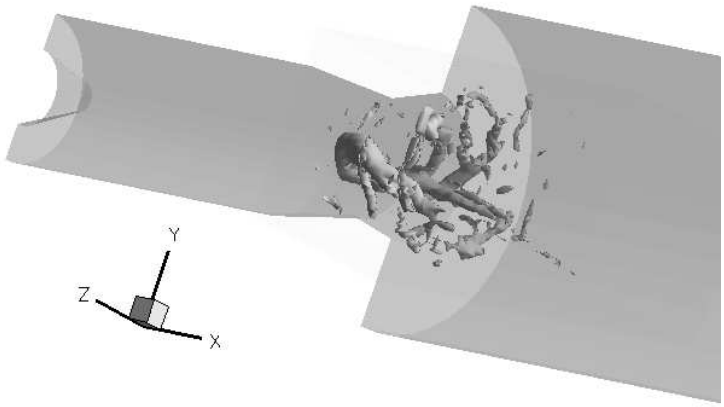

Figure 5.5: Visualization of the two helical structures by means of the λ_2 technique.

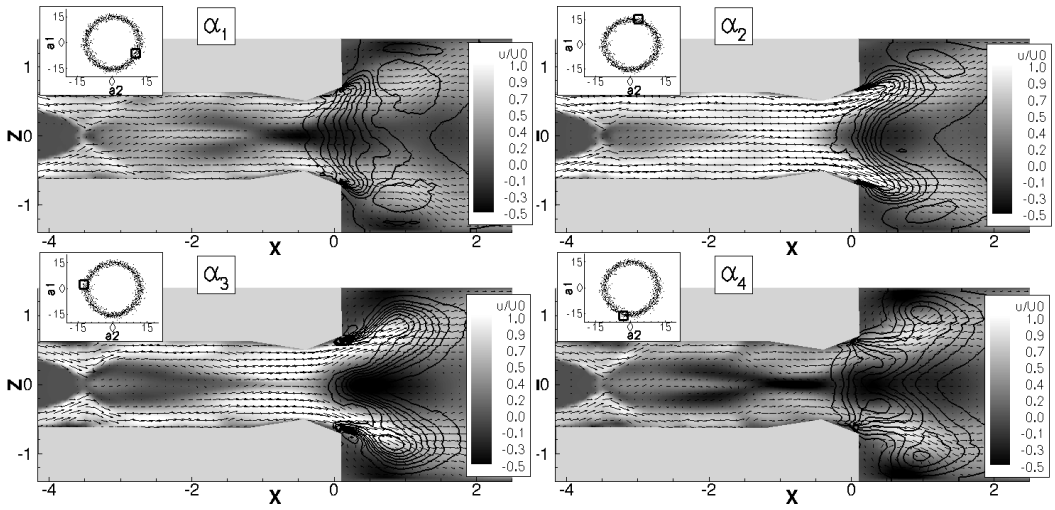

Figure 5.6: Reconstruction of instantaneous snapshots in the longitudinal plane. POD end EPOD Modes 0-2. Axial velocity contour plot and vector map. Progress variable isolines (From 0.05 to 0.95). Scatter plots of time coefficients (a1(t) vs a2(t)) in the boxes. Forced case (St=0.3, A=20%).

applying the procedure described in Section 3.3.3. In the top left of Fig. 5.6 the mass inflow at the inlet is increasing. At this phase angle α_1 the flame is rather elongated and the IRZ is inside the contraction pulling the flame upstream. At the phase angle α_2 (top right) the mass inflow has reached its maximum and the flame is compact. At phase angle α_3 the flame brush has a tulip shape and its leading edge is out of the contraction. The mass inflow has started decreasing and a negative velocity region appears in the wake of the bluff body. The recirculation zone is enforced and when the inflow reaches its minimum (α_4) a long intense recirculation zone is seen. The flame is pulled upstream, it starts to be elongated again and a new cycle can start. The long recirculation at low inflow velocity explains the flame stabilization differences. The EPOD analysis confirms the power of this tool to correlate flow and flame dynamics, in this case depicting how the vortex breakdown and flame stabilization are affected by the axial fluctuations.

5.2 TARS

A selection of the most relevant results obtained for the TARS burner are given in the following. In Section 5.2.1 the isothermal flow trough this fuel-injector, simulated by LES, is presented (case “Isothermal”in Table 4.2). In Section 5.2.2 it is exemplified how the POD analysis is able to extract relevant information from a set of data which would be lost of traditional statistical approach. The analysis is performed on OH* chemiluminescence images of a flame undergoing well-defined continuous thermo-acoustic oscillations (case “Confined”in Table 4.2).

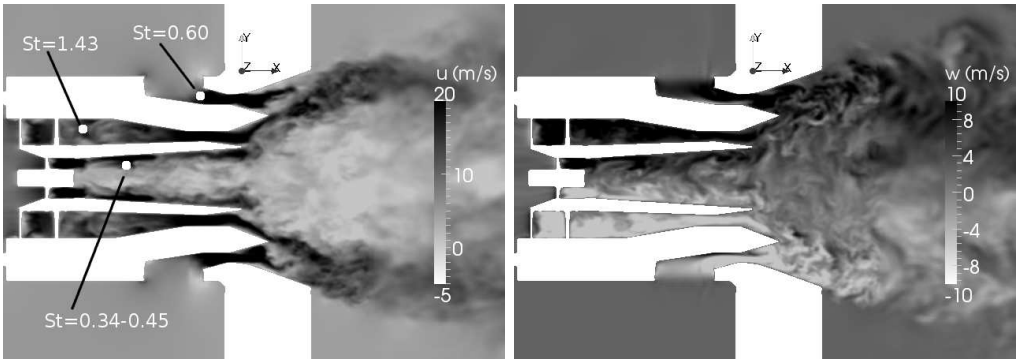

Figure 5.7: Axial (left) and out-of-plane (right) velocity components contour plot. Longitudinal (z/D=0) planar cut. Case Isothermal.

5.2.1 Details of the flow inside the TARS by LES

5.2.1.1 Instantaneous flow

In Fig. 5.7 instantaneous fields are shown. In a longitudinal plane (z/D=0), the contour plot of axial (u) and out-of-plane (w) velocity components are shown. The flow is characterized by a wide range of scales, small inside the TARS, larger downstream the nozzle. One can note the complexity of the flow through the different swirlers. Three swirling jets generated by the three sets of vanes and the shear layers between them merge together near the TARS nozzle outlet. Downstream the TARS, the field presents a typical configuration for an open-air swirling flow. An annular swirling jet surrounds a Central Recirculation Zone. The inner shear layers (between the jet and the CRZ), as well as the outer shear layers (between the jet and the fluid at rest) generate larger scales and it is possible to see stretched, separated pockets of high tangential velocity. A peculiar characteristic of the TARS swirler should be remarked. Since the inner swirler is followed by a pipe, the vortex breakdown can propagate upstream: a recirculation zone is also observed inside the central swirler connected with the CRZ.

5.2.1.2 Statistics and origin of the asymmetry

The flow inside the TARS is highlighted in Fig. 5.8 where the average field is shown. The axial velocity contour is plotted together with a vector map. The highest velocities are found at the throats of the narrow vanes, and the interaction between the jets coming from the three air passages is visualized in details. Regions of annular reversed flow are found at the tips of the inner and intermediate swirlers, favouring the merging of the jets. The zero velocity iso-line highlights the shape of the CRZ, which is narrow and elongated in the inner air passage and then suddenly expands in the TARS nozzle. The toroidal recirculation zone at the inner tip interconnects with the CRZ and as a result of this interaction a toroidal M-shaped region of reverse flow is observed. Detachment of the boundary layer along the walls of the

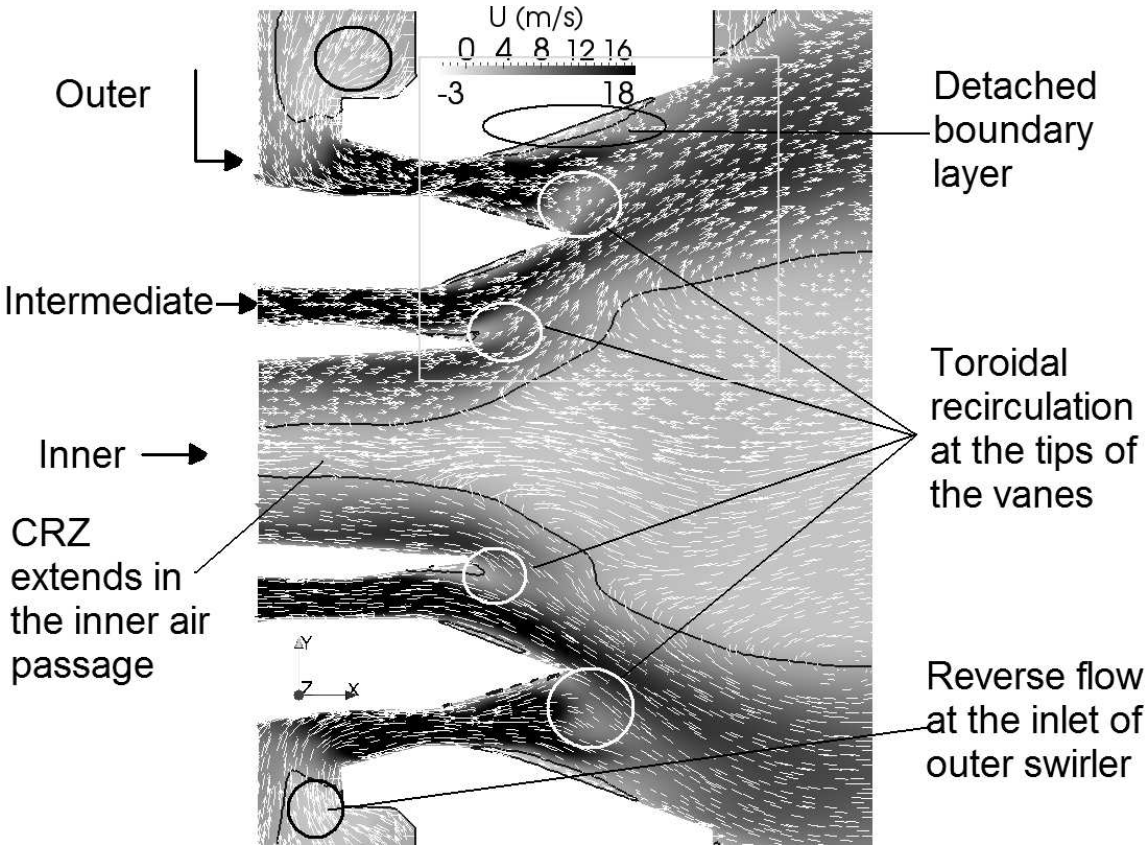

Figure 5.8: Mean axial velocity contour plot and vector map. Longitudinal planar cut (z/D=0). The vectors have constant length to favour their visualization.

TARS nozzle should also be mentioned, as well as reverse flow at the entrance of the outer swirler vanes. Looking at the vectors in Fig. 5.8 it is possible to observe the asymmetrical features of the average flow. Such asymmetrical features are highlighted in Fig. 5.9 where iso-lines of the mean axial velocity are depicted, showing the influence on the flow of the bodies upstream the TARS. By looking at the grey iso-line in Fig. 5.9, it is clear that the effect of the wakes generated behind the arms of the support and the fuel pipes is felt at the entrance of the outer swirler vanes, and the low speed flow has circumferential nonuniformity before entering the vanes. This variability is conserved or amplified during the acceleration through the swirler vane, and still present downstream of the nozzle, as visible both in the jet and in the CRZ (for example, looking at the white and black isolines in the region between and around x/D=-0.2 and x/D=0.1 in Fig. 5.9). Such asymmetrical features have been found also in PIV measurements, available in different azimuthal planes. Single azimuthal profiles from the computations are compared to two opposite profiles in the experiments in Fig. 5.10, which shows that the simulations are able to capture the azimuthal variability particularly immediately downstream of the TARS. Further downstream the LES is more symmetric. When averaging circumferentially,

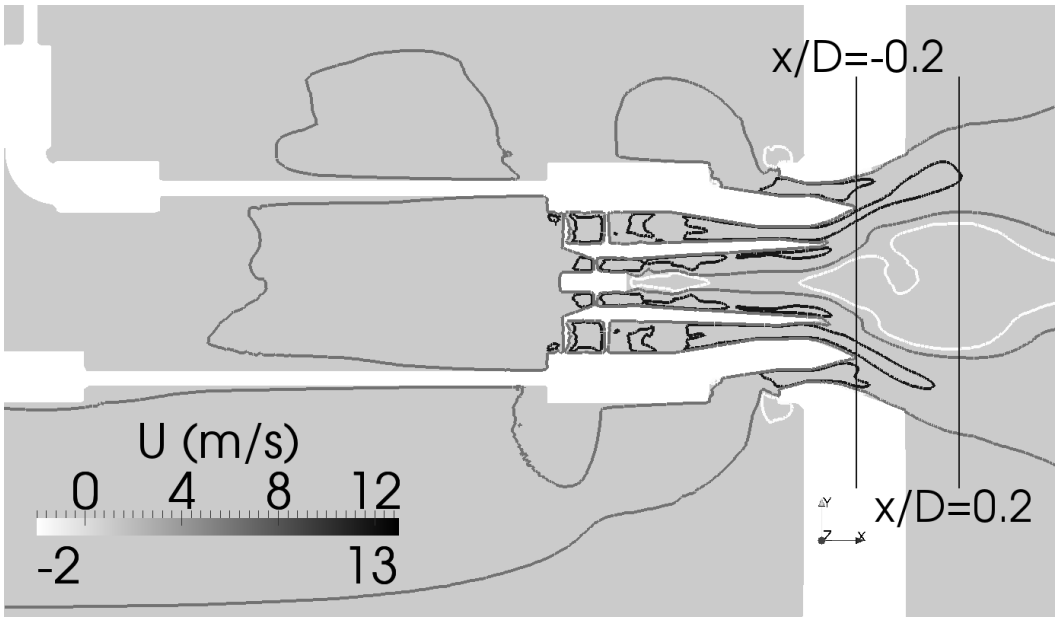

Figure 5.9: Mean axial velocity isolines. Longitudinal (z/D=0) planar cut.

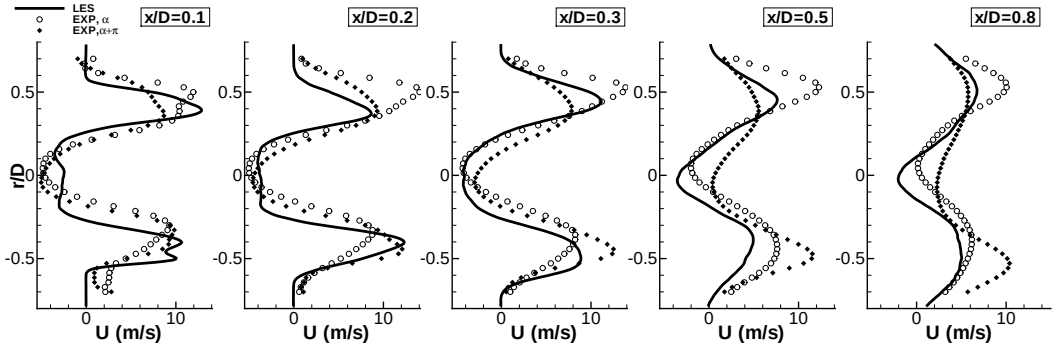

Figure 5.10: Asymmetry in single azimuthal profiles.

the profiles are nearly symmetric in both LES and PIV (Fig. 5.11). The agreement between LES and PIV is reasonable, given the complexity of the flow. For example, the radial positions of the peaks are well captured and both LES and PIV show a width of the CRZ of approximately 0.5D.

5.2.1.3 PVC identification by means of POD

In Fig. 5.12 an iso-surface of the (instantaneous) axial velocity (u=-1.5 m/s) is depicted in dark grey. The CRZ is visible, and one can also note the reverse flow at the outer swirler inlet. The CRZ is highly wrinkled by the small scale turbulence generated in the very complex flow inside the TARS. Nonetheless, large scale coherent structures also seem to coexist. In light grey an instantaneous pressure iso-surface is also depicted. It suggests the existence of a PVC, with the typical shape

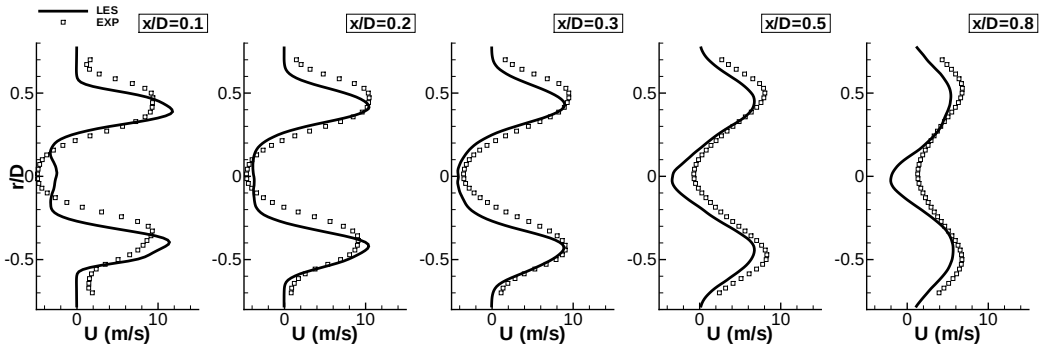

Figure 5.11: Azimuthally averaged mean axial velocity profiles.

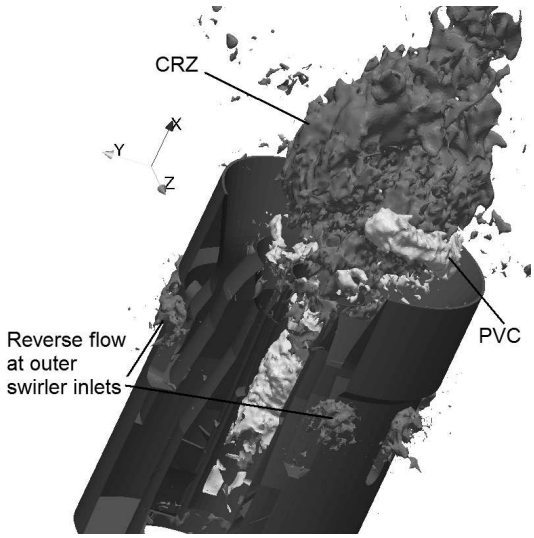

Figure 5.12: Dark grey:Instantaneous axial velocity iso-surface (U=-1.5 m/s); Light grey: instantaneous pressure iso-surface (p=-50Pa).

of an helical structure wrapped around the CRZ [21]. It should also be remarked that the PVC here seems to originate in the inner air passage. Analyzing the PVC (for example estimating its frequency) by visually tracking its structure is rather difficult since, as it was shown throughout this section, the flow inside and outside the TARS is very complex. It features multiple shear layers, multiple recirculation zones, boundary layer detachments, a wide range of structures. To identify and characterize large scale coherent structures, smoothing out the random turbulent fluctuations, we therefore apply POD. The results are reported in the following. The POD analysis is performed on two-dimensional slices of the domain, the longitudinal plane (z/D=0) and a perpendicular plane downstream the TARS nozzle outlet (x/D=0.05). Modes 0-3 in the longitudinal section are depicted in Fig. 5.13. The contour of the axial velocity component is plotted. Mode 0 corresponds to the mean field, as stated earlier. Modes 1-3 hint the existence of helical modes,

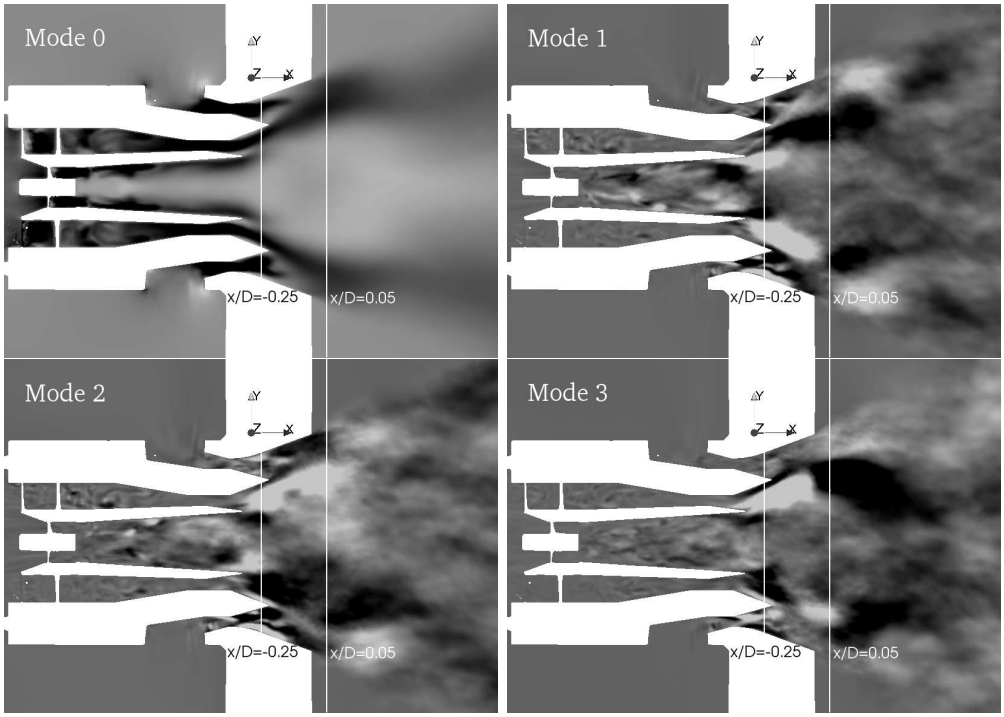

Figure 5.13: Modes 0, 1, 2, 3. Contour plot of axial velocity (arbitrary scale). Planar cut: z/D=0.

similar to the ones found for the Lisbon burner in Fig. 5.3. Here, they do not seem to be strong enough so that POD would clearly distinguish them from the other asymmetrical features of the flow which we have seen to be significant. They originate in the inner swirler, and are still present in the nozzle, despite the merging with the jets emanating from the intermediate and outer swirlers. The POD results in the perpendicular cross section are presented in Fig. 5.14, which describes the first three modes. The mean flow field (mode 0) contains the traces of the flow passage through the eight vanes of the intermediate and outer swirlers. One should also notice once more the azimuthal asymmetry. Modes 1-2 capture the precessing vortex core, which exhibit the typical shape for this kind of instability, similar to what reported for the Lisbon burner in Fig. 5.4. A Fourier analysis of the time coefficients, not presented here, shows that the flow has multi-frequency components, with important contributions at 175 Hz and 350 Hz, in both the planar cuts.

5.2.2 Thermo-acoustic instability analysis by POD based phase averaging

5.2.2.1 Statistics

Traditional statistics (average and RMS) of the OH* chemiluminescence images are shown in Fig. 5.15. The only information that one can get from these data is that

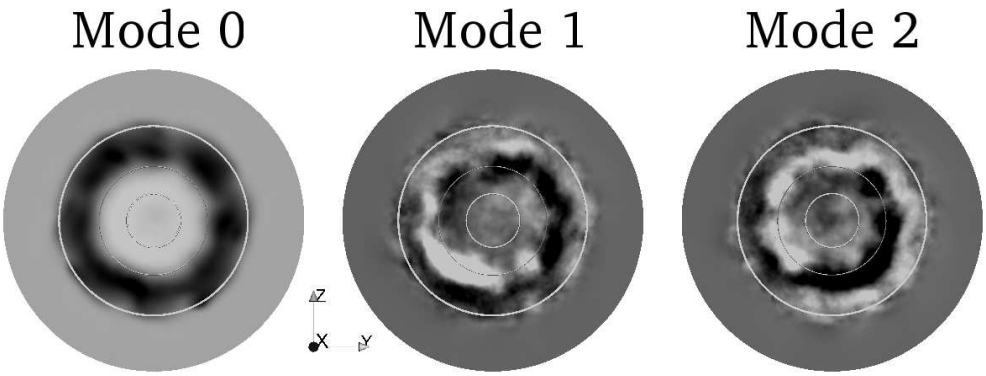

Figure 5.14: Modes 0, 1, 2. Contour plot of axial velocity (Arbitrary scale). Planar cut: x/D=0.1.

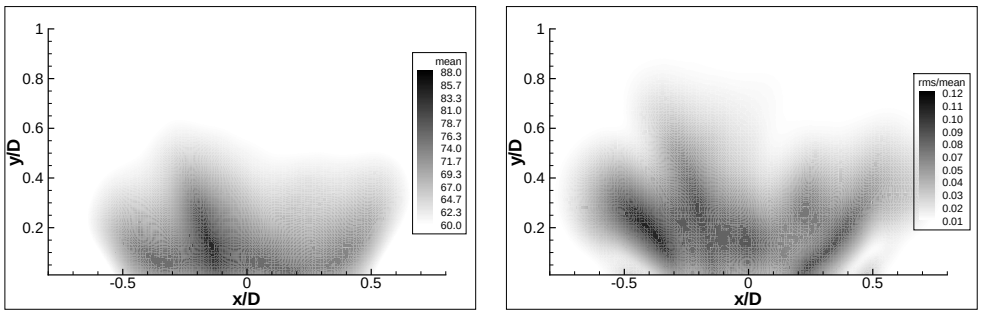

(a) (b)

Figure 5.15: Mean (a) and RMS/Mean (b) OH-chemiluminescence signal contour plot. Arbitrary units.

the mean field is not symmetric, and that the largest fluctuations are found in the outer shear layers. Nothing can be said about the dynamics using this approach. A way to retain the dynamics is then to perform Proper Orthogonal Decomposition. The results of this analysis are shown in the following section.

5.2.2.2 POD analysis

The POD highlights the most energetic fluctuations or modes of the flame. In Fig. 5.16 the first two modes are shown. They represent axial oscillations of the flame which are not symmetric in radial direction. For example, in Mode 1, non uniform bright and dark areas are found along radial lines $y/D = 0.2$ and $y/D = 0.4$, respectively.

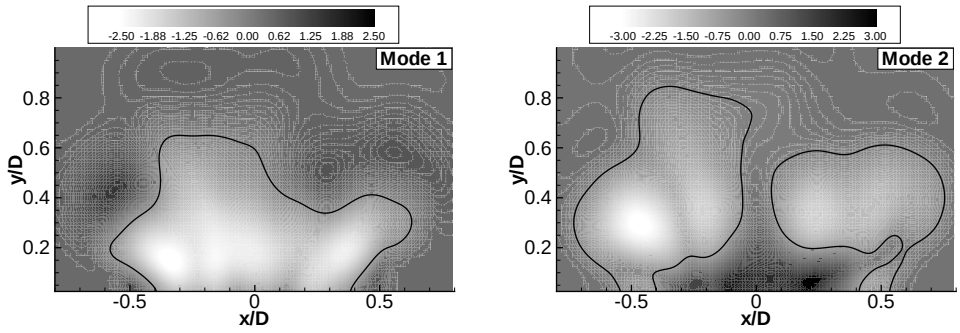

(a) (b)

Figure 5.16: Mode 1 (left) and mode 2 (right). Contour plot of OH-chemiluminescence signal. Arbitrary scale and sign. The solid black line indicates the 0 iso-contour.

5.2.2.3 POD based phase averaging

In contrast to the previous cases, here the frequency of these dynamics cannot be extracted from the time coefficient analysis, because the acquisition rate (7 Hz) was much slower than the combustion dynamics (estimated to be about 245 Hz from the spectral analysis of an ambient microphone acquistion). However the time coefficients of modes 1 and 2 feature an interesting property as shown in Fig. 3.9: the scatter plot $a_1(t)$ vs $a_2(t)$ assumes a circumferential pattern. These modes are therefore a pair of harmonic modes and they are eligible candidates for the a-posteriori phase averaging procedure presented in Section 3.3.3. The results are shown in Fig. 5.17, where the averages over one cycle of thermo-acoustic oscillation (four different phase angles, spaced by $\pi/2$) are shown. The flame is elongated in frame (a), pulled back close to the inlet in frame (b), pushed again downstream in frame (c) and reaches the maximum elongation at frame (d), then another cycle is repeated. Spatially integrating the OH images, the heat relase can be estimated. A phase average of the integrals (not presented here, see Paper IV) shows that the heat release follows a sine-like curve during one cycle of oscillation. The power of POD for extracting relevant dynamics of flames is demonstrated. The POD based phase averaging offers clear advantages with respect to traditional approaches. It isolates and visualizes the modes responsible for the instability, with their relative energetic content, and follows their evolution through the time coefficients series. This is precious extra-information. Neither phase-locking nor a simultaneous pressure transducer acquisition are needed. One does not need to know a-priori the frequency of the instability, and the instability does not necessarily need to be strong, as one needs with a pressure transducer for example. One might find out for example possible connections with higher harmonic modes, or, if existing, deal with different modes at different frequencies (not necessarily sub or higher harmonics) within the same acquisition. The analysis procedure here presented extracts non-trivial dynamics of a flame under thermo-acoustic instability, using a complex geometry

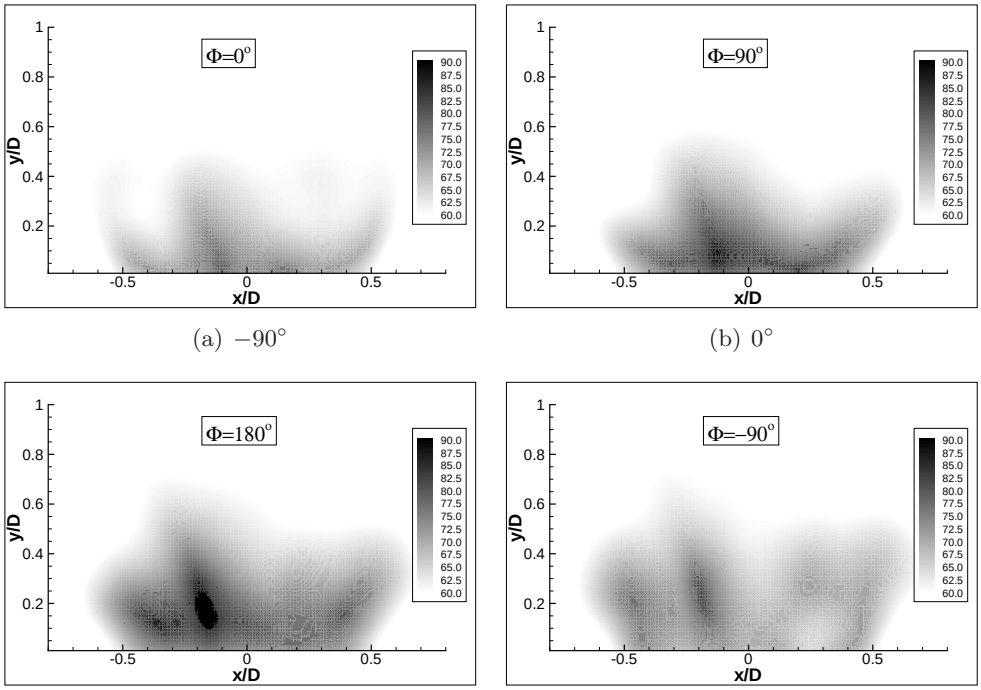

(a) $-90°$ (b) $0°$

(c) $90°$ (d) $180°$

Figure 5.17: POD based phase average over one thermo-acoustic cycle. Phase angles from $-90°$ (top left) to $180°$ (bottom right). Contour plot of OH chemiluminesce (Arbitrary Unit).

burner but relatively simple, cheap, fast to set-up experimental equipment. It therefore enables to post-process industrial data where practical and economical issues often prohibit complex laser diagnostic apparatus.

Chapter 6

Summary of the papers and author contribution

Paper I

P. Iudiciani and C. Duwig, "Large Eddy Simulation of the sensitivity of vortex breakdown and flame stabilization to axial forcing", *Flow, Turbulence and Combustion, 86, 639–666, 2011*

In this paper, the effect of axial forcing on the flame/vortex breakdown interaction is studied, with particular focus on the PVC. LES, together with a filtered flamelet model describing the subgrid combustion, is performed to study a lean premixed flame undergoing mass flow fluctuations in a wide range of frequencies and amplitude. In average, forcing at frequencies lower than the PVC characteristic frequency moves the recirculation zone upstream the combustor in the premixing tube, while higher frequencies do not relevantly affect the flow/flame. With the help of POD a detailed analysis of the dynamics of the central recirculation zone is performed showing how the excitation at lower frequencies weakens the PVC and allows the flame to propagate upstream. Extended POD is also applied to illustrate the flow/flame interactions during the excitation cycle.

The code, the combustion model and the test case were developed and set-up in previous works by C. Duwig and L. Fuchs. The candidate carried out the new simulations, post-processed the results, performed the POD-EPOD analysis and wrote a major part of the paper under the supervision of C. Duwig.

Paper II

C. Duwig and P. Iudiciani, "Extended Proper Orthogonal Decomposition Analysis of Flame/Acoustic Interaction". *Flow, Turbulence and Combustion, 84, 25-47, 2010*

In this work, simultaneous OH-PLIF and PIV acquisitions of a laminar premixed flame forced with acoustic waves are used to exemplify and promote the usage of POD and Extended POD in combustion applications. The concept of Extended

POD, to highlight the correlations and interaction of flow/flame dynamics, is applied for the first time in the field of combustion. POD is applied separately on PIV and PLIF data, both in an unforced and forced case. The PIV-POD performs well only in the forced case, in which the fluctuations are amplified by the excitations. PLIF-POD instead detects equally well the flame dynamics in both cases and it is therefore chosen as a suitable base for the EPOD analysis. When applying the EPOD analysis, the fluctuations in the velocity field are highlighted in both unforced and forced cases, overcoming problems such as bad seeding in the burnt gases and low number of available samples.

The data were acquired by the candidate for his Master's thesis work at the ENEA Research Centre (New Technologies, Energy and Environment Agency) "Casaccia" in Rome (Italy) in collaboration with the Department of Mechanics and Aeronautics of the University of Rome "La Sapienza". The candidate performed the POD and EPOD analysis, and wrote the paper together with C. Duwig.

Paper III

P. Iudiciani, C. Duwig, R.Z. Szasz, L. Fuchs, S.M. Hosseini, and E.J. Gutmark, "LES investigation of the flow dynamics in a realistic gas turbine multi-swirl fuel-injector". *Manuscript, submitted to AIAA journal, 2012*

In this paper, the flow through a fuel-injector with three swirlers, the TARS, has been studied by means of Large Eddy Simulation and PIV measurements. Good agreement was found between the computational and experimental data highlighting also the features of the flow inside the TARS burner. Sensitivity to the grid and to the SGS model was determined to be within the range of experimental uncertainty. The flow azimuthal structure was shown to be mainly affected by the flow passage through multiple vanes of the three swirlers, and by the upstream structure that supports the fuel injector and supply fuel. Precise inlet boundary conditions that include these geometrical elements were critical to obtain accurate prediction of the complex flow structure. This finding is important because practical combustor in aeroengines have similar geometry which is often ignored in experimental and computational investigations. Proper Orthogonal Decomposition analysis helped to separate coherent structures from the complex turbulent flow, revealing the existence of helical structures leading to a precessing vortex core.

The candidate carried out the LES simulations, post-processed the results, and wrote a major part of the paper, with additions from S.M. Hosseini, under the supervision of E. Gutmark, C. Duwig, R.Z. Szasz and L. Fuchs.

Paper IV

P. Iudiciani, C. Duwig, S.M. Hosseini, R.Z. Szasz, L. Fuchs and E.J. Gutmark, "Proper Orthogonal Decomposition for experimental investigation of swirling flame instabilities". *Accepted for publication in AIAA journal, to appear 2012*

An experimental investigation of premixed flames undergoing thermo-acoustic instability is presented. The paper focuses on the data post-processing, aiming at extracting information about the dynamics that are lost through classical time averaging approach. Proper Orthogonal Decomposition together with a derived a-posteriori phase averaging procedure are applied to OH* chemiluminescence data, obtained with a simple experimental set-up at low acquisition rate. The combustion dynamics are successfully reconstructed from the raw data, without the need of extra acquisitions or of phase locking the measurements, and providing extra-information about the instability modes. The method was validated against high speed camera direct light measurements. In an intermittent case close to bifurcation, the procedure further helps to sort out different states of the flame.

The candidate participated to the experimental campaign. The experimental rig was set-up by M.S. Hosseini, and R.Z. Szasz. The candidate post-processed the results and performed the POD analysis. The candidate wrote a major part of the paper, with additions from S.M. Hosseini, and the supervision of E. Gutmark, C. Duwig, R.Z. Szasz and L. Fuchs.

Paper V

P. Iudiciani, C. Duwig, R.Z. Szasz, L. Fuchs, S.M. Hosseini and E.J. Gutmark, "Numerical and experimental investigation of swirling flows and flames generated through a multi-swirl fuel injector". *ISABE-2011-1132, 12-16 September 2011, Gothenburg, Sweden*

In this paper, reacting flows in a complex geometry fuel injector of interest for aero-engines applications have been simulated by means of LES. The proposed formulation captures well the dynamics of the flow/flame in a stable case. For different operating conditions, a dual behaviour is observed, in which stabilization in the wake of the burner and flashback coexists depending on the initial conditions. Useful insights about the flame holding mechanism are provided. The LES results are in qualitative agreement with the experimental measurements.

The candidate carried out the LES simulations, post-processed the results, and wrote a major part of the paper, with additions from S.M. Hosseini, under the supervision of E. Gutmark, C. Duwig, R.Z. Szasz and L. Fuchs.

Paper VI

P. Iudiciani, C. Duwig, R.Z. Szasz, L. Fuchs and E.J. Gutmark, "LES of the interaction between a premixed flame and complex turbulent swirling flow". *13th European Turbulence Conference ETC13. Journal of Physics: Conference Series, 318(9):092007*

In this paper the TARS, a fuel injector characterized by complex design with three concentric air passages, has been studied numerically. A swirl-stabilized lean premixed flame has been simulated by means of LES. The computations characterize successfully the dynamics of the flame and their interactions with the complex swirling flow. The flame is stabilized upstream the fuel injector exit, and the dynamics are led by a PVC which seems to originate in the inner air passage. The results obtained by POD analysis are in agreement with previous findings in the context of swirling flows/flames.

The candidate carried out the LES simulations, post-processed the results, and wrote a major part of the paper, under the supervision of E. Gutmark, C. Duwig, R.Z. Szasz and L. Fuchs.

Chapter 7

Conclusions and future work

7.1 Conclusions

In this work, advanced techniques (LES, POD, and optical diagnostic techniques) have been applied to analyze swirl stabilized flames, relevant to gas turbine applications. The methods used enhance the understanding swirling flame dynamics. In particular, Large Eddy Simulations of a forced flame (the so called Lisbon burner) showed the influence of axial oscillations on the flame stabilization by vortex breakdown. Forcing at frequencies lower than the PVC weakened the PVC itself allowing the flame to stabilize more upstream, while frequencies equal or higher than the PVC did not significantly affect the flame stabilization. Lock-in of the PVC with the excitation frequency was not observed. Moreover the mean flame front was found not to coincide with the shear-layer surrounding the CRZ because of the PVC motion.

For the TARS burner, the LES presented here clarified the details of the complex flow through the fuel-injector, and characterized the dynamics of the swirling flow downstream the TARS. In order to reduce uncertainties, the LES simulation of the complete burner was carried out, including relevant details of the rig, such as the support arm and fuel supply pipes upstream the TARS. It was shown that the upstream details play an important role for the variability of the azimuthal structure in an isothermal case. An LES formulation with finite rate chemistry was tested in reacting cases. The formulation was able to explain the peculiar stabilization mechanism in a case where the CRZ was destroyed by thermal expansion, to capture dual behavior/hysteresis phenomena, to describe the dynamics of a lean flame and its interaction with the PVC. The present formulation is therefore promising for the more detailed study of selected test-cases from the current and future database of experiments.

The analyses presented in this thesis included Proper Orthogonal Decomposition applied to both numerical and experimental data in order to explore the flame dynamics. Large scale flow and flame fluctuations due to coherent structures have been highlighted in different academic combustors encouraging the use of Proper Orthogonal Decomposition in combustion applications. A POD-based a-posteriori phase averaging procedure was used to study combustion dynamics, enabling the reconstruction of cycles of thermo-acoustic instabilities. Using a simple and relatively cheap set-up, such technique may be applied for in-situ industrial measurements.

Finally, this work introduced the usage of Extended POD for the analysis of the interaction between flow and flame dynamics. Such technique was applied

for the first time in the context of reacting flows. In particular it highlighted the mechanism by which axial oscillations weaken the PVC in a swirl-stabilized flame in the numerical study mentioned above. Applied in an experimental study, it related the dynamics of a laminar flame to vortex shedding in the shear layers.

7.2 Future work

Recently, the TARS test-rig has been modified to include a premixing tube added at the TARS outlet and both confined and unconfined flames have been measured. The goal is to study the influence of vortex breakdown on flame stabilization and flashback. In particular the mutual positions of the recirculation zone and the flame position are addressed. Effects of varying equivalence ratios are considered. Simulations of these new test-cases would certainly positively complement the experimental results. Some limiting assumptions should still be listed as base for further work. First, the assumption of adiabatic walls might be refined, especially inside the swirler vanes since they are thin and rather close to the flame. In order to capture the possible complex stabilization at the swirler edges, more refined wall temperature modeling as well as a detailed chemical mechanism might be required.

Clearly, these new databases will also open new possibilities to confirm the validity of POD and EPOD analysis to address the dynamics of swirling flows and flames.

Acknowledgements

This thesis is the result of the four years that I spent at the division of Fluid Mechanics, Lund University. At the end of this journey a few people should be thanked, to have made this possible, valuable, and fun.

Firstly, I would like to acknowledge my supervisor, Prof. Laszlo Fuchs, for giving me the opportunity to join the group. Thank you for always being stimulative towards scientific critical thinking and for continuously reminding what it means to do *re-search*.

A grateful thank goes to my co-supervisor, Dr. Christophe Duwig, for being the motor of this research (re-search, sorry Laszlo!) project. Thank you for all the precious discussions about combustion, dynamics of swirling flows and flames, POD, and for the friendliness demonstrated during these years. Especially, thank you for the extreme rapidity, simplicity and efficiency in answering my e-mails! Now you can tell me your secret, how do you manage?!

Many thanks go to my other co-supervisor, Dr. Robert Szasz, for always kindly, friendly and readily answering all my questions about CFD. Thank you for helping me with computer related issues and for introducing me to the wonderful world of Linux. Can I finally get the root password now?!

I would also like to acknowledge Prof. Effie Gutmark for all the valuable discussions and suggestions. Thank you for always making me feel at ease while sharing your vast experience during your visits to Lund.

Robert Collin, Andreas Lantz, and Mohammad Seyed Hosseini are also acknowledged for the great work done during the experiments in the lab.

The simulations were run on several computational centers throughout Sweden: LUNARC at Lund University, Akka at Umeå University, PDC at the Royal Institute of Technology in Stockholm.

This work would not have been possible without the entities who financially supported the project: Vetenskap Rådet (VR), the Centre for Combustion Science and Technology (CECOST) and the Swedish energy authority (STEM).

Therefore, thanks to the Swedish tax payers, who indirectly finance these institutions. About this, I would like to remark that, being an Italian, the first time I read such an acknowledgement in previous theses, I thought it was written with irony! How many things you have taught me during these years, dear Sverige.

I also want to thank and salute all my colleagues, present and past ones, at the divisions of fluid mechanics and combustion physics. More in particular, thank you:

Eric "typically"Baudoin, for leaving the entire office for me. Just kidding. Seriously, thanks because since you left we do not go to Finn Inn anymore. Kidding again, you were a great office mate and friend!

"Giovane Esploratore"Tobias Joelsson, aka "Wolf", for allowing me to contemporarily obtain a Ph.D. on the Vietnam War. Thank you also for constant good mood and smiles!

Holger "Oliver"Grosshans, for having spent uncountable hours together trying to find the analytical solution of the NS equations. I hope you will mention me while holding the speech for your future Nobel Prize. Which, I remind you though, we have higher chances to win for peace in the world. Let's love turbulence and use it for change!

Jiangfei and Fan, for always bringing me back nice gifts from China;

Rixin and Mehdi, for never banal discussions at Fysikum about work related topics, and non;

Alper, Hesam, Aurelia, Rickard and Henning, thank you for being a very nice regular company during lunches and (a bit less regular, unfortunately) evening beers.

Then, it's your turn, my dear Lundian friend. If you ever got to read this thesis, well first thank you because it means that you probably came to listen to the boring dissertation! I will name only you who *actually* have some chances to *actually* read this! So, in kind of chronological order, thank you Ale "De André"Barni, Julioccini, Adri Le"t's dance"pur, the "apples"Keyvan and Viveka, Moe "that's a good question"Takemura, Anna "once in a lifetime"Beek, Michele "che boss"Giunta, Anna "baking queen"G (som Gemma!), Cristin "what is this?"Giessler, and all of you guys it would take for ever to mention. I heartily thank you for all the lovely time spent together in Lund during the last four years.

Biggest thanks and love to Emilijute, for making the last two years even more special. My wish is that one day we will write a paper together about the turbulence of indian slums!

Infine, un sentito grazie ai miei genitori, Francesca and Tonio, e alla mia sorellina cairota Laura. Mi dispiace tanto di non trascorrere abbastanza tempo insieme a voi, tuttavia é un sollievo sapere che il baricentro della famiglia resta sempre in Abruzzo!

Bibliography

[1] International Energy Agency. Key world energy statistics. Technical report, IEA report, 2009.

[2] Princeton Environmental Institute. Princeton's next generation jet fuel project. Technical report, Princeton University, 2009. http://www.princeton.edu/pei/energy/presentations/, last access april 2010.

[3] A.H. Lefebvre. The role of fuel preparation in low-emission combustion. *Journal of Engineering for Gas Turbines and Power*, 117, 1995.

[4] D.W. Bahr. Gas turbine combustion and emission abatment technology. current and projected status. *Proceedings of the International Gas Turbine Congress 1999 Kobe*, 1999.

[5] Y. Huang and V. Yang. Dynamics and stability of lean-premixed swirl-stabilized combustion. *Progress in Energy and Combustion Science*, 35(4):293–364, 2009. doi:10.1016/j.pecs.2009.01.002.

[6] T. Lieuwen. Combustion dynamics in lean-premixed prevaporized (LPP) gas turbines. *Journal of Propulsion and Power*, 19, 2003.

[7] O. Lucca-Negro and T. O'Doherty. Vortex breakdown: a review. *Progress in Energy and Combustion Science*, 27(4):431–481, 2001. doi:10.1016/S0360-1285(00)00022-8.

[8] Y. Sommerer, D. Galley, T. Poinsot, S. Ducruix, F Lacas, and D. Veynante. Large eddy simulation and experimental study of flashback and blow-off in a lean partially premixed swirled burner. *Journal of Turbulence*, 5, 2004.

[9] M. Konle, F. Kiesewetter, and T. Sattelmayer. Simultaneous high repetition rate PIV-LIF measurements of CIVB driven flashback. *Exp. Fluids*, 44:529–538, 2008.

[10] S. Nair and T. Lieuwen. Near-blowoff dynamics of a bluff-body stabilized flame. *Journal of Propulsion and Power*, 23(2):421–427, 2007.

[11] E. Gutmark, T.P. Parr, D.M. Parr, and K.C. Schadow. Evolution of vortical structures in flames. *Twenty-Second International Symposium on Combustion/The Combustion Institute*, pages 523–529, 1988.

[12] Balachandran et al. Experimental investigation of the nonlinear response of turbulent premixed flames to imposed inlet velocity oscillations. *Comb. Flame*, 143:37–55, 2005.

[13] O.J. Teerling, A.C. McIntosh, J. Brindley, and V.H.Y Tam. Premixed flame response to oscillatory pressure waves. *Proceedings of the Combustion Institute*, 30:1733–1740, 2005.

[14] S. Shanbhogue and T. Lieuwen. Studies on the vorticity field of harmonically excited bluff body flames. *46th AIAA Aerospace Sciences Meeting and Exhibit, AIAA 2008–122. Reno, USA*, 2008.

[15] T. Schuller, D. Durox, and S. Candel. Self-induced combustion oscillations of laminar pre-mixed flames stabilized on annular burners. *Comb. Flame*, 135:525–537, 2003.

[16] D. Durox, S. Ducruix, and S. Candel. Experiments on collapsing cylindrical flames. *Comb. Flame*, 125:982–1000, 2001.

[17] S. Candel, D. Durox, S. Ducruix, A. L. Birbaud, N. Noiray, and T. Schuller. Flame dynamics and combustion noise: progress and challenges. *International Journal of Aeroacoustics*, 8(1-2):1–56, 2009.

[18] R. Szasz, C. Duwig, and L. Fuchs. Noise generated by a lifred flame in a vitiated co-flow. *Proceedings of ASME Turbo Expo 2008: Power for Land, Sea and Air*, GT2008-51186, 2008.

[19] C. Duwig, L. Fuchs, A. Lacarelle, M. Beutke, and C.O. Paschereit. Study of the vortex breakdown in a conical swirler using LDV, LES and POD. *Proceedings of ASME Turbo Expo 2007*, GT2007-27006, 2007.

[20] S.I. Shtork, N.F. Vieira, and E.C. Fernandes. On the identification of helical instabilities in a reacting swirling flow. *Fuel*, 87(10-11):2314–2321, 2008. doi:10.1016/j.fuel.2007.10.016.

[21] N. Syred. A review of oscillation mechanisms and the role of the precessing vortex core (PVC) in swirl combustion systems. *Progress in Energy and Combustion Science*, 32(2):93–161, 2006. doi:10.1016/j.pecs.2005.10.002.

[22] F. Martinelli, A. Olivani, and A. Coghe. Experimental analysis of the precessing vortex core in a free swirling jet. *Exp. Fluids*, 42(6):827–839, 2007. doi:10.1007/s00348-006-0230-x.

[23] P.M. Anacleto, E.C. Fernandes, M.V. Heitor, and S.I Shtork. Swirl flow structure and flame characteristic in a model lean premixed combustor. *Combust. Sci. and tech.*, 175:1369–1388, 2003.

[24] C. Duwig and L. Fuchs. Large eddy simulation of vortex breakdown/flame interaction. *Phys. Fluids*, 19(075103), 2007. doi:10.1063/1.2749812.

[25] M. Stöhr, R. Sadanandan, and W. Meier. Experimental study of unsteady flame structures of an oscillating swirl flame in a gas turbine model combustor. *Proceedings of the Combustion Institute*, 32:2952–2932, 2009.

[26] S. Khalil, K. Hourigan, and M.C. Thompson. Response of unconfined vortex breakdown to axial pulsing. *Phys. Fluids*, 18, 2006.

[27] S.V. Alekseenko et al. Effect of axisymmetric forcing on the structure of a swirling turbulent jet. *International Journal of Heat and Fluid Flow*, 29:1699–1715, 2008.

[28] S. Wang, S.Y. Hsieh, and V.Yang. Unsteady flow evolution in swirl injector with radial entry. II. External excitation. *Phys. Fluids*, 17(045107), 2005. doi:10.1063/1.1874932.

[29] F. Gallaire, S. Rott, and J.M. Chomaz. Experimental study of a free and force swirling jet. *Phys. Fluids*, 16, 2004.

[30] A. Lacarelle, T. Faistmann, D. Greenblatt, C.O. Paschereit, O. Lehmann, D.M. Luchtenburg, and B.R. Noach. Spatio-temporal characterization of a conical swirler flow field under strong forcing. *Journal of Engineering for Gas Turbine and Power*, 131(031504), 2009. doi:10.1115/1.2982139.

[31] K. Oberleithner, M. Sieber, C.N. Nayeri, C.O. Paschereit, C. Petz, H.-C. Hege, B.R. Noack, and I. Wygnasnki. Three-dimensional coherent structures in a swirling jet undergoing vortex breakdown: stability analysis and empirical mode construction les of chemical and acoustic forcing of a premixed dump combustor. *J. Fluid. Mech.*, 679:383–414, 2011. doi:10.1017/jfm.2011.141.

[32] C.O. Paschereit, E. J. Gutmark, and W. Weisenstein. Coherent structures in swirling flows and their role in acoustic combustion control. *Phys. Fluids*, 11(9):2667–2678, 1999.

[33] D.M. Kang, F.E.C. Culick, and A. Ratner. Combustion dynamics of a low-swirl combustor. *Comb. Flame*, 151:412–425, 2007.

[34] S.K. Thumuluru and T. Lieuwen. Characterization of acoustically forced swirl flame dynamics. *Proceedings of the Combunstion Institute*, 32:2893–2900, 2009.

[35] B.D. Bellows, M.K. Bobba, A. Forte, J.T. Seitzman, and T. Lieuwen. Flame transfer function saturation mechanism in a swirl-stabilized combustor. *Proceedings of the Combustion Institute*, 31:3181–3188, 2007.

[36] P. Palies, D. Durox, T. Schuller, and S. Candel. The combined dynamics of swirler and turbulent premixed swirling flames. *Combustion and Flame*, 157(9):1698–1717, 2010.

[37] Uyi Idahosa, Abhishek Saha, Chengying Xu, and Saptarshi Basu. Non-premixed acoustically perturbed swirling flame dynamics. *Combustion and Flame*, 157(9):1800–1814, 2010.

[38] K.T. Kim, J.G. Lee, B.D. Quay, and D.A. Santavicca. Spatially distributed flame transfer functions for predicting combustion dynamics in lean premixed gas turbine combustors. *Combustion and Flame*, 157(9):1718–1730, 2010.

[39] A.M. Steinberg, I. Boxx, M. Stöhr, C.D. Carter, and W. Meier. Flow-flame interactions causing acoustically coupled heat release fluctuations in a thermo-acoustically unstable gas turbine model combustor. *Combustion and Flame*, 157(12):2250–2266, 2010.

[40] U. Piomelli. Large-eddy simulation: achievements and challenges. *Progress in Aerospace Sciences*, 35(4):335–362, 1999. doi:10.1016/S0376-0421(98)00014-1.

[41] C.M. Coats. Coherent structures in combustion. *Prog in Energy and Comb. Sci.*, 22:427–509, 1996.

[42] C.E. Cala, E.C. Fernandes, M.V. Heitor, and S.I. Shtork. Coherent structures in unsteady swirling jet flow. *Exp. Fluids*, 40:267–276, 2006.

[43] G. Berkooz, P. Holmes, and J.L. Lumley. The proper orthogonal decomposition in the analysis of turbulent flows. *Annu. Rev. Fluid Mech.*, 25:539–575, 1993. doi:10.1146/annurev.fl.25.010193.002543.

[44] T. Smith, J. Moehlis, and P. Holmes. Low-dimensional modelling of turbulence using the proper orthogonal decomposition. a tutorial. *Nonlinear Dyn.*, 41:275–307, 2005.

[45] L. Perret, J. Delville, R. Manceau, and J.P. Bonnet. Turbulent inflow conditions for large-eddy simulation based on low-order empirical model. *Phys. Fluids*, 20, 2008.

[46] S. Bernero and H.E. Fiedler. Application of particle image velocimetry and proper orthogonal decomposition to the study of a jet in a counterflow. *Exp. Fluids*, 29:274–281, 2000.

[47] K.E. Meyer, J.M. Pedersen, and O. Ozcan. A turbulent jet in crossflow analysed with proper orthogonal decomposition. *J. Fluid Mech.*, 583:199–227, 2007.

[48] K. Bizon, G. Continillo, E. Mancaruso, S.S. Merola, and B.M. Veglieco. POD-based analysis of combustion images in optically accessible engines. *Comb. Flame*, 157(4):632–640, 2010.

[49] C. Alvarez-Herrera, D. Moreno-Hernandez, and B. Barrientos-Garcia. Temperature measurement of an axisymmetric flame by using a schlieren system. *J. Optics A-Pure and Applied Optics*, 2008.

[50] H.G. Sung. Combustion dynamics in a model lean-premixed gas turbine with a swirl stabilized injector. *J. Mech. Sci. and Technology*, 21(3):495–504, 2007.

[51] X.M. Huang and W.T. Baumann. Reduced-order modeling of dynamic heat release for thermoacoustic instability prediction. *Comb Sci Tech.*, 179(3):617–636, 2007.

[52] A. Kodal et al. Turbulence filter and POD analysis for velocity fields in lifted CH4-air diffusion flames. *Flow, Turbulence and Combustion*, 70:21–41, 2003.

[53] A. Lacarelle, D.M. Luchtenburg, M.R. Bothien, B.R. Noack, and C.O. Paschereit. A combination of image post-processing tools to identify coherent structures of premixed flames. *Int. Conf. on Jets, Wakes and Separated Flows, ICJWSF-2008, 16-19 September 2009, Berlin, Germany*, 2009.

[54] C. Duwig and L. Fuchs. Large eddy simulation of a H2/N2 lifted flame in a vitiated coflow. *Comb. Sci. and Tech.*, 180(3):453–480, 2008.

[55] A. Roux, L.Y.M. Gicquel, Y. Sommerer, and T.J. Poinsot. Large eddy simulation of mean and oscillating flow in a side-dump ramjet combustor. *Combustion and Flame*, 152(1-2):154–176, 2008.

[56] B. W. van Oudheusden, F. Scarano, N. P. van Hinsberg, and D. W. Watt. Phase-resolved characterization of vortex shedding in the near wake of a square-section cylinder at incidence. *Experiments in Fluids*, 39:86–98, 2005.

[57] Tony Ruiz, C. Sicot, L. Brizzi, J. Borée, and Y. Gervais. Pressure/velocity coupling induced by a near wall wake. *Experiments in Fluids*, 49:147–165, 2010.

[58] S. Maurel, J. Borée, and J.L. Lumley. Extended proper orthogonal decomposition: Application to jet/vortex interaction. *Flow, Turbulence and Combustion*, 67:125–136, 2001.

[59] J. Borée. Extended proper orthogonal decomposition: a tool to analyse correlated events in turbulent flows. *Experiments in Fluids*, 35:188–192, 2003.

[60] E.C. Fernandes, M.V. Heitor, and S.I. Shtork. An analysis of unsteady highly turbulent swirling flow in a model vortex combustor. *Exp. Fluids*, 40(2):177–187, 2006. doi:10.1007/s00348-005-0034-4.

[61] P. Iudiciani and C. Duwig. Large eddy simulation of the sensitivity of vortex breakdown and flame stabilisation to axial forcing. *Flow, Turbulence and Combustion*, 86:639–666, 2011.

[62] C. Duwig and P. Iudiciani. Extended proper orthogonal decomposition analysis of flame/acoustic interaction. *Flow, Turbulence and Combustion*, 84(1):25–47, 2010. doi:10.1007/s10494-009-9210-6.

[63] G. Li and E.J. Gutmark. Effect of exhaust nozzle geometry on combustor flow field and combustion characteristics. *Proceedings of the Combustion Institute*, 30(2):2893–2901, 2005. doi:10.1016/j.proci.2004.08.189.

[64] P. Iudiciani, C. Duwig, R.Z. Szasz, L. Fuchs, S.M. Hosseini, and E.J. Gutmark. LES investigation of the flow dynamics in a realistic gas turbine multi-swirl fuel-injector. *Manuscript, submitted to AIAA journal*, 2012.

[65] P. Iudiciani, C. Duwig, S.M. Hosseini, R.Z. Szasz, L. Fuchs, and E.J. Gutmark. Proper orthogonal decomposition for experimental investigation of flame instabilities. *Accepted for publication in AIAA journal, to appear*, 2012.

[66] P. Iudiciani, C. Duwig, R.Z. Szasz, L. Fuchs, S.M. Hosseini, and E.J. Gutmark. Numerical and experimental investigation of swirling flows and flames generated through a multi-swirl fuel injector. In *ISABE-2011-1132, 12-16 September 2011, Gothenburg, Sweden.*

[67] P. Iudiciani, C. Duwig, R.Z. Szasz, L. Fuchs, and E.J. Gutmark. LES of the interaction between a premixed flame and complex turbulent swirling flow. *Journal of Physics: Conference Series*, 318(9):092007, 2011. doi:10.1088/1742-6596/318/9/092007.

[68] O. Reynolds. An experimental investigation of the circumstances which determine wheter the motion of water shall be direct or sinuous, and the law of resistance in parallel channels. *Philos. Trans. R. Soc. London Ser. A174*, pages 935–982, 1883.

[69] S. Pope. *Turbulent Flows.* Cambridge University Press, 2000.

[70] T. Poinsot and D. Veynante. *Theoretical and Numerical Combustion.* Edwards, 2000.

[71] G. Smith, T. Bowman, M. Frenklach, B. Gardiner, et al. GRI mechanism. *http://www.me.berkeley.edu/gri-mech/, last access june 2011.*

[72] S. Turns. *An introduction to combustion.* McGraw-Hill, 2000.

[73] A.H. Lefebvre. *Gas Turbine Combustion, second edition.* Taylor and Francis, 1999.

[74] C. Duwig, D. Stankovic, L. Fuchs, G. Li, and E.J. Gutmark. Experimental and numerical study of flameless combustion in a model gas turbine combustor. *Combust. Sci. and Tech.*, 180:279–295, 2000.

[75] P.J. Coelho and N. Peters. Numerical simulation of a mild combustion burner. *Comb. Flame*, 124:503–518, 2001.

[76] Antonio Cavaliere and Mara de Joannon. Mild combustion. *Progress in Energy and Combustion Science*, 30(4):329–366, 2004.

[77] E. Mallard and H.L. Le Chatelier. Recherches expérimentales et théoriques sur la combustion des mélanges gazeux explosifs. *Ann. des Mines*, 1883.

[78] C. Fureby. On subgrid scale modeling in large eddy simulations of compressible fluid flow. *Physics of Fluids*, 8(5):1301–1311, 1996.

[79] J. Smagorinsky. General circulation experiments with the primitive equations: I. the basic equations. *Mon. Weather Review*, 91:99–164, 1963.

[80] J. Bardina, J.H. Ferziger, and W.C. Reynolds. Improved subgrid-scale models for large-eddy simulation. *AIAA Paper No.*, (80-1357), 1980.

[81] A. Germano, U. Piomelli, P. Moin, and W.H. Cabot. A dynamic subgrid-scale eddy viscosity model. *Phys. Fluids*, 3:1760–1765, 1991.

[82] D.K. Lilly. A proposed modification of the Germano subgrid-scale closure method. *Phys. Fluids A*, 4:633, 1991. doi:10.1063/1.858280.

[83] P. Sagaut, P. Comte, and F. Ducros. Filtered subgrid-scale models. *Physics of Fluids*, 12(1):233–236, 2000.

[84] L. G. Margolin, W. J. Rider, and F. F. Grinstein. Modeling turbulent flow with implicit LES. *Journal of Turbulence*, 7(15), 2006. doi:10.1080/14685240500331595.

[85] C. Fureby and F.F. Grinstein. Monotonically integrated large eddy simulation of free shear flows. *AIAA journal*, 37(5), 1999.

[86] C. Fureby. ILES and LES of complex engineering turbulent flows. *Journal of Fluids Engineering*, 129:1514–1523, 2007.

[87] F.F. Grinstein, T.R. Young, E.J. Gutmark, G. Li, G. Hsiao, and H.C. Mongia. Flow dynamics in a swirl combustor. *Journal of Turbulence*, 3(030), 2002. doi:10.1088/1468-5248/3/1/030.

[88] C. Duwig and L. Fuchs. Study of flame stabilization in a swirling combustor using a new flamelet formulation. *Combust. Sci. and tech.*, 177:1485–1510, 2005.

[89] C. Duwig and C. Fureby. Large eddy simulation of unsteady lean stratified premixed combustion. *Comb. and Flame*, 151:85–103, 2007.

[90] C. Duwig. Study of a filtered flamelet formulation for large eddy simulation of premixed turbulent flames. *Flow, Turbulence and Combustion*, 2007.

[91] H. Pitsch. Large-eddy simulation of turbulent combustion. *Annual Review of Fluid Mechanics*, 38(1):453–482, 2006. doi:10.1146/annurev.fluid.38.050304.092133.

[92] J. Janicka and A. Sadiki. Large eddy simulation of turbulent combustion systems. *Proceedings of the Combustion Institute*, 30(1):537 – 547, 2005. doi:10.1016/j.proci.2004.08.279.

[93] C. Duwig, K-J. Nogenmyr, C-K. Chan, and M.J. Dunn. Large eddy simulations of a piloted lean premix jet flame using finite-rate chemistry. *Combustion Theory and Modelling*, 15(4):537–568, 2011.

[94] L. Selle, G. Lartigue, T. Poinsot, R. Koch, K. U. Schildmacher, W. Krebs, B. Prade, P. Kaufmann, and D. Veynante. Compressible large-eddy simulation of turbulent combustion in complex geometry on unstructured meshes. *Combustion and Flame*, 137(4):489–505, 2004.

[95] O. Kruger, K. Gockeler, S. Göke, C. O. Paschereit, C. Duwig, and L. Fuchs. Numerical investigations of a swirl-stabilized premixed flame at ultra-wet conditions. *GT2011-45866, Proceedings of ASME Turbo Expo 2011, Vancouver, Canada*, 2011.

[96] O. Colin, F. Ducros, D. Veynante, and T. Poinsot. A thickened flame model for large eddy simulations of turbulent premixed combustion. *Physics of Fluids*, 12(7):1843–1863, 2000.

[97] T.D. Butler and P.J. O'Rourke. A numerical method for two-dimensional unsteady reacting flows. *16th Int. Symp. on Combustion. the Combustion Institute*, 1977.

[98] V. Raman and H. Pitsch. A consistent les/filtered-density function formulation for the simulation of turbulent flames with detailed chemistry. *Proceedings of the Combustion Institute*, 31(2):1711 – 1719, 2007. doi:10.1016/j.proci.2006.07.152.

[99] A.R. Kerstein, W. Ashurt, and K. W. Williams. Field equation for interface propagation in an unsteady homogeneous field. *Phys. Rev.*, 37, 1988.

[100] N. Peters. The turbulent burning velocity for large-scale and small-scale turbulence. *Journal of Fluid Mechanics*, 384(1):107–132, 1999.

[101] H. Pitsch and L. Duchamp de Lageneste. Large-eddy simulation of premixed turbulent combustion using a level-set approach. *Proceedings of the Combustion Institute*, 29(2):2001 – 2008, 2002. doi:10.1016/S1540-7489(02)80244-9.

[102] K.-J. Nogenmyr, C. Fureby, X.S. Bai, P. Petersson, R. Collin, and M. Linne. Large eddy simulation and laser diagnostic studies on a low swirl stratified premixed flame. *Combustion and Flame*, 156(1):25–36, 2009.

[103] M. Boger, D. Veynante, H. Boughanem, and A. Trouve. Direct numerical simulation analysis of flame surface density concept for large eddy simulation of turbulent premixed combustion. *27th Int. Symp. on Combustion*, 1998.

[104] C. Fureby. A fractal flame-wrinkling large eddy simulation model for premixed turbulent combustion. *Proceedings of the Combustion Institute*, 30, 2005.

[105] C. Meneveau and T. Poinsot. Stretching and quenching of flamelets in premixed turbulent combustion. *Comb. Flame*, 86, 1991.

[106] H.G. Weller, G. Tabor, A.D. Gosman, and C. Fureby. Application of a flame-wrinkling LES combustion model to a turbulent mixing layer. *Twenty-Seventh Symposium (International) on Combustion/The Combustion Institute*, 1998.

[107] Sébastien Candel. Combustion dynamics and control: Progress and challenges. *Proceedings of the Combustion Institute*, 29(1):1–28, 2002.

[108] H.C. Mongia, T.J. Held, G.C. Hsiao, and R.P. Pandalai. Challenges and progress in controlling dynamics in gas turbine combustors. *Journal of Propulsion and Power*, 19(5):822–829, 2003.

[109] J.H. Ferziger and M. Perić. *Computational Methods for Fluid Dynamics*. Springer, 1999.

[110] 1.J. Gullbrand, X.S. Bai, and L. Fuchs. High-order cartesian grid method for calculation of incompressible turbulent flows. *Int. J. Numer. Methods Fluids*, 36, 2001.

[111] http://www.openfoam.com, last access April 2011.

[112] H.G. Weller, G. Tabor, H. Jasak, and C. Fureby. A tensorial approach to computational continuum mechanics using object-oriented techniques. *Computers in physics*, 12(6):620–631, 1998. doi:10.1063/1.168744.

[113] R. Mittal and G. Iaccarino. Immersed boundary methods. *Annu. Rev. Fluid Mech.*, 37:239–261, 2005.

[114] G.S. Jang and C.W. Shu. Efficient implementation of weighted ENO schemes. *J. Comput. Phys.*, 126:202–228, 1996.

[115] A. Harten, B. Engquist, S. Osher, and S. Chakravarthy. Uniformly high order accurate essentially non-oscillatory schemes, III. *J. Comput. Phys.*, 71(2):231–303, 1987. doi:10.1016/0021-9991(87)90031-3.

[116] H. Jasak. *Error analysis and estimation for the Finite Volume method with applications to fluid flows*. Doctoral thesis, Imperial College, 1996.

[117] J. Kiefer, Z.S. Li, J. Zetterberg, X.S. Bai, and M. Aldén. Investigation of local flame structures and statistics in partially premixed turbulent jet flames using simultaneous single-shot CH and OH planar laser-induced fluorescence imaging. *Comb. Flame*, pages 802–818, 2008.

[118] S.A. Filatyev, M.P. Thariyan, R.P. Lucht, and J.P. Gore. Simultaneous stereo particle image velocimetry and double-pulsed planar laser-induced fluorescence of turbulent premixed flames. *Comb. Flame*, 150(3):201–209, 2007.

[119] A. C. Eckbreth. *Laser diagnostics for combustion temperature and species.* Gordon and Breach Publishers, 1996.

[120] L. Sirovich. Turbulence and the dynamics of coherent structures. part 1: coherent structures. *Quart. App. Math., XLV*, 3:561–571, 1987.

[121] N. Aubry. On the hidden beauty of proper orthogonal decomposition. *Theoret. Comput. Fluid Dynamics*, 2:339–352, 1991.

[122] M. Legrand, J. Nogueira, A. Lecuona, S. Nauri, and P. Rodríguez. Atmospheric low swirl burner flow characterization with stereo piv. *Experiments in Fluids*, 48:901–913, 2010.

[123] M. Stöhr, R. Sadanandan, and W. Meier. Phase-resolved characterization of vortex–flame interaction in a turbulent swirl flame. *Experiments in Fluids*, 51:1153–1167, 2011.

[124] C.O.U. Umeh, Z. Rusak, E.J. Gutmark, R. Villavalva, and D. Cha. Experimental and computational study of non-reacting vortex breakdown in a swirl-stabilized combustor. In *47th AIAA Aerospace Sciences Meeting, January 2009.*

[125] C.O.U. Umeh, Z. Rusak, and E.J. Gutmark. Experimental study of reaction and vortex breakdown in a swirl-stabilized combustor. *ASME Conference Proceedings*, 2009(GT2009-60183):935–950, 2009. doi:10.1115/GT2009-60183.

[126] R. Villalva Gomez, E.J. Gutmark, and C.O.U. Umeh. Characterization and dynamics of lean direct-injection swirl-stabilized flames. *AIAA paper*, AIAA-2009-5414, 2009.

[127] C. Fureby, F.F. Grinstein, G. Li, and E.J. Gutmark. An experimental and computational study of a multi-swirl gas turbine combustor. *Proceedings of the Combustion Institute*, 31(2):3107–3114, 2007. doi:10.1016/j.proci.2006.07.127.